DISCLAIMER

UNIVERSITY OF CALIFORNIA
Radiation Laboratory

Cover Sheet
Do not remove

RESTRICTED DATA
This document contains restricted data as defined in the Atomic Energy Act of 1946. Its transmittal or disclosure of its contents in any manner to an unauthorized person is prohibited.

UCRL 1173
INDEX NO. _____
This document contains 190 pages
This is copy 16 of 19 Series A

Issued to INFORMATION DIVISION

~~CONFIDENTIAL~~ DECLASSIFIED
~~classification~~

Each person who receives this document must sign the cover sheet in the space below.

Route to	Noted by	Date	Route to	Noted by	Date
				RKW	OCT 28 1955

UNIVERSITY OF CALIFORNIA

Radiation Laboratory

Contract No. W-7405-eng-48

RF FIELD INVESTIGATIONS ON THE 1/10 SCALE MARK I CAVITY

Mitchell Dazey, Dale Nielsen,

Raymond Robertson and Duane Sewell

March 13, 1951

Berkeley, California

Standard Distribution	Copy Numbers
Atomic Energy Commission, Washington	1-4
Carbide and Carbon Chemicals Division (Y-12 Area)	5
Chicago Operations Office	6
North American Aviation	7
Oak Ridge National Laboratory, X-10 Site	8
Patent Branch, Washington	9
Technical Information Service, Oak Ridge	10-14
University of California Radiation Laboratory	15-19
Total	19

Information Division
Radiation Laboratory
Univ. of California
Berkeley, California

OUTLINE OF 1/10-SCALE CAVITY REPORT

RF FIELD INVESTIGATIONS ON THE 1/10-SCALE MARK I CAVITY

Mitchell Dazey, Dale Nielsen, Raymond Robertson and Duane Sewell

Radiation Laboratory, Department of Physics
University of California, Berkeley, California

March 13, 1951

I INTRODUCTION

Early in the design of Mark I it was decided to check as many of the rf characteristics as possible by measurements on a model of the machine. Hence, a 1/10-scale model of the liner and drift tube assembly was built.

The following investigations were carried out on the cavity:

A. Magnetic Field Distributions

From the distributions were derived:

A. Losses

B. Shunt impedance, Z_s

C. Q

D. Other miscellaneous items

B. Drift Tube Stem Data

A. Determination of optimum position

B. Perturbation data

C. Bypass capacitor requirements

C. Drift Tube Perturbation Data

D. Measured Q

These investigations were carried out by a group already in existence and working on similar measurements for various experimental half-cells. This group included, in addition to the authors, the following personnel: Ralph

Dufour, Frank Grobelch, Max Harris, William Lawton, Craig Nunan, and John Waddell.

Much of the experience accumulated was directly applicable to the 1/10-scale measurements, and is included as a part of this report. All results that are given in this report are in terms of the full scale Mark I machine unless otherwise indicated.

The following nomenclature will be followed throughout this report:

1. The model with 7 1/2 drift tubes will be referred to as (7 1/2 M) and the later design with 8 1/2 drift tubes as (8 1/2 M).

2. Drift tube will be abbreviated DT, and to designate the position of a particular one this will be followed by the number, e.g., drift tube number seven is designated as DT-7.

3. DT's will be numbered from the entrance end of the cavity with the one-half DT mounted on the entrance end designated as DT-0.

4. A DT-cell-1 will be defined as the volume included between two successive planes on the center-lines between drift tubes and bounded by the cavity wall, as shown in Fig. I-1.

5. A DT-cell-2 will be defined as that volume included between planes through two successive drift tube longitudinal center-lines and bounded by the cavity wall (see Fig. I-1).

6. H-probe identifies a small ($r \ll \lambda$) shielded loop at the end of a coaxial transmission line for sampling magnetic fields.

7. E-probe identifies an open circuit transmission line with the inner conductor a small fraction of a wave-length longer than the outer conductor. These are used to sample electric fields.

8. A quantity which is proportional to the magnetic field B at any given point will be denoted F, and the absolute magnitude of the field will

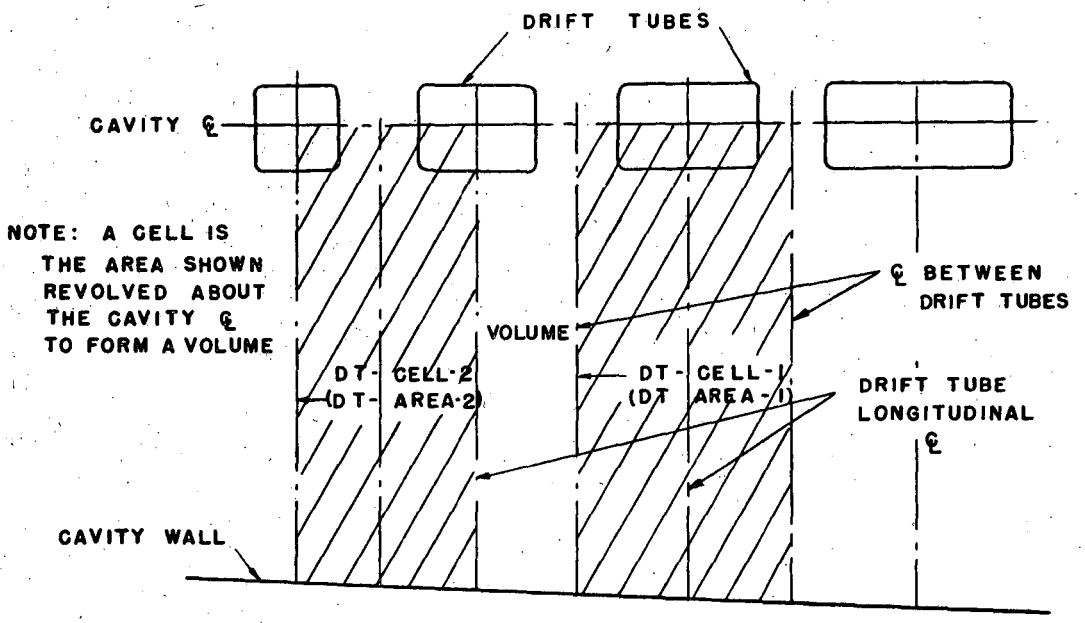

DEFINITION OF AREAS

FIG. I-1

MU1526

be denoted by B.

9. All fields, currents, and voltages are given in terms of their maximum amplitudes unless otherwise specified. (This means that calculations of power must be properly converted to r.m.s. values.)

10. The cavity was at all times operating in the TM_{010} mode.

II THEORETICAL CONSIDERATIONS

No attempt will be made here to delve into the theory of resonant cavities and, further, many commonly used expressions (such as the one for depth of penetration of an rf current into a conductor) will be used without proof.

There are two quantities of particular interest, namely Q, which relates the energy stored to the power loss, and the shunt impedance, Z_s, which relates the power loss to the voltage. At resonance Z_s is a purely resistive element and will be treated as such throughout this section.

The expressions for Q and Z_s can be transformed into a variety of forms, each of particular usefulness in connection with a particular method of attack for the problem at hand. The forms most useful for the methods of measurement described in the following sections will be developed.

We will define at the outset a few useful quantities:*

σ = conductivity (mhos/meter)

= 5.8×10^7 mhos/meter (commercial copper) (II-1)

δ = skin depth or depth to which an rf current penetrates into a conductor before it is attenuated to 1/e of its value at the surface. (This is also the equivalent thickness of a conductor of conductivity σ if uniform current density were present.)

$$\delta = \sqrt{\frac{1}{\pi f \mu \sigma}} = \sqrt{\frac{2}{\omega \mu \sigma}} \text{ meters} \qquad \text{(II-2)}$$

$$= \frac{0.0660}{\sqrt{f}} \text{ meters (commercial copper)} \qquad \text{(II-3)}$$

---

* A treatment of the relations as used in this section is to be found in "Fields and Waves in Modern Radio," by Ramo and Whinnery, Chapter 6.

f = frequency (cycles/sec.) (II-4)

λ = wave-length (meters) (II-5)

f and λ are related by the velocity of light, c:

$c = f\lambda = 3 \times 10^8$ meters/sec. (II-6)

$\omega = 2\pi f$, the angular velocity (radians/sec.) (II-7)

μ = permeability of the medium

$= 4\pi \times 10^{-7}$ henrys/meter for free space (and copper) (II-8)

All relations are determined in terms of the peak values of fields, voltages and currents, and MKS units will be used throughout.

A. Losses in a resonant cavity

A familiar form for the power loss, P_L, in a resistance R is:

$$P_L = \frac{1}{2} I^2 R \quad \text{watts} \tag{II-9}$$

where: I = Peak current (amperes)

R = Resistance (ohms)

We can expect the current to vary over different portions of the cavity (depending on the mode of oscillation and the geometry of the cavity), so we express Eq. (II-9) in integral form:

$$P_L = \iint_{\Sigma S} \frac{1}{2} I_S^2 R_S \cdot dS \tag{II-10}$$

where: I_S = Peak surface current per unit width. (Amperes/meter)

R_S = Surface resistivity (ohms/square)

dS = An elementary area on the boundary surface as defined in Fig. II-1.

Further, it can be shown that the current density in the conducting surface is equal in magnitude to the tangential magnetic field at the surface. Expressed

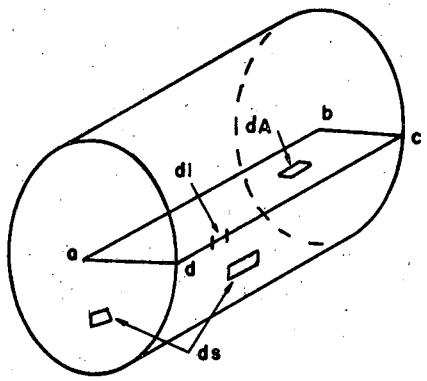

dA – DIFFERENTIAL AREA ON A PLANE THROUGH THE CENTER LINE.

a-b-c-d - DEFINES THE PLANE OF dA.

ds - DIFFERENTIAL AREA ON A CONDUCTING BOUNDARY SURFACE (INCLUDING DRIFT TUBES WHICH ARE NOT SHOWN IN THIS SIMPLIFIED SKETCH.)

dl - DIFFERENTIAL LENGTH ANYWHERE IN CAVITY

DIFINITIONS OF PLANES AND SURFACES

FIG. II. - 1

MU 1527

mathematically this is:

$$|I_S| = |n \times H_t| \quad \text{amperes/meter} \tag{II-11}$$

R_S, the surface resistivity, can be deduced from a consideration of the d.c. resistance, $R_{d.c.}$, and the skin depth:

$$R_{d.c.} = \frac{\ell}{\sigma A} \tag{II-12}$$

where: σ = Conductivity of the material (ohms/meter)

ℓ = Length of the path (meters)

A = Cross-sectional area of the conductor transverse to the current flow. (Meters^2)

For a strip of unit width and skin depth, δ :

$$A = \delta \text{ (meters)}$$

Then if we consider also a unit length of path, R_S, becomes:

$$R_S = \frac{1}{\sigma \delta} \text{ ohms/square} \tag{II-13}$$

Substituting Eq. (II-2):

$$R_S = \pi f \mu \delta = \sqrt{\frac{\pi f \mu}{\sigma}} \tag{II-14}$$

$$= 2.61 \times 10^{-7} \sqrt{f} \text{ ohms/square}$$

(in commercial copper)

Combining Eqs. (II-10), (II-11), (II-14):

$$P_L = \frac{\pi f \mu \delta}{2} \iint_{\Sigma S} (n \times H_t)^2 \, dS \tag{II-15}$$

or, in terms of the induction field $B = \mu H$

$$P_L = \frac{\pi f \delta}{2\mu} \iint_{\Sigma S} (n \times B_t)^2 \, dS$$

or,

$$\left.\begin{aligned} P_L &= \frac{\pi f \delta}{2\mu} \iint_{\Sigma S} |B_t|^2 \, dS \\ &= \frac{1.431 \times 10^9}{\sqrt{\lambda}} \iint_{\Sigma S} |B_t|^2 \, dS \end{aligned}\right\} \qquad \text{(II-16)}$$

B. Voltage considerations

It is not convenient to measure the voltage, V, directly in a cavity, but by some simple transformations it can be obtained from field measurements. In general:

$$V = \int E \cdot d\ell \qquad \text{(II-17)}$$

where: E = Electric field gradient.

V = Total voltage

This can be transformed by means of the Maxwell equation:

$$\nabla \times E = -\frac{\partial B}{\partial t} \qquad \text{(II-18)}$$

where: B = magnetic induction field (webers/meter^2)

Integrate both sides of this equation over a field area. We will denote a differential element of this area by dA (to avoid confusion with an element of area on the bounding surfaces, as shown in Fig. II-1). Transform the left hand side by means of Stokes theorem:

$$\iint (\nabla \times E) \cdot dA = \oint E \cdot d\ell \qquad \text{(II-19)}$$

(The line integral is taken around the boundary of the surface of integration.)

Then Eq. (II-18) becomes:

$$\oint E \cdot d\ell = \iint_{\text{field}} -\frac{\partial B}{\partial t} \cdot dA \qquad \text{(II-20)}$$

We are dealing with steady state time harmonic fields of the general form $e^{j\omega t}$, hence, the partial derivative with time can be written as $j\omega e^{j\omega t}$ (the $e^{j\omega t}$ is inferred in all the field equations for our system). Then Eq. (II-20) becomes:

$$\oint E \cdot d\ell = -j\omega \iint_{\text{field}} B \cdot dA$$

or:

$$V_c = \left| \oint E \cdot d\ell \right| = + \left| \omega \iint_{\text{field}} B \cdot dA \right| \qquad \text{(II-21)}$$

It is convenient to adapt the limits of the above integrals to our best advantage. This can be done by defining the field area in our system as being a plane surface bounded by the center line of the cavity and the outer walls as shown in Fig. II-1. This requires that $\oint E \cdot d\ell$ be taken along the center-line and returning around the outer wall (path a-b-c-d-a) shown in Fig. II-1. The convenience of this choice of boundaries is evident when it is noted that:

$$\int_b^c E \cdot d\ell = \int_c^d E \cdot d\ell = \int_d^a E \cdot d\ell \equiv 0 \qquad \text{(II-22)}$$

This is due to the boundary condition that the tangential component of E is equal to zero at a conducting boundary.

C. Stored energy

No attempt will be made here to derive the relations for the stored energy in a cavity. It is a constant for steady state conditions and is all in the magnetic fields at the instant they reach their peak value and all in the electric fields at the instant they reach their peak value. Between these two instants the stored energy is divided between the electric and magnetic

fields. The energy in terms of the electric fields is not of interest to us. The usual form for the energy storage in terms of the magnetic field is:

$$U_H = \frac{1}{2} \int_{\text{volume}} \mu H^2 \cdot d_V$$

or in terms of the magnetic induction, B:

$$U_H = \frac{1}{2\mu} \int_{\text{volume}} B^2 \cdot d_V \qquad \text{(II-23)}$$

where the integration is carried out over the entire volume of the cavity.

D. Frequency deviation methods for obtaining E and H. (B-B runs)

In addition to the direct field sampling methods utilizing the formulae detailed above there is a second independent means of determining the fields in a cavity. This utilizes the fact that a closed metallic surface or a volume of dielectric material inserted into the cavity will change the resonant frequency. It is beyond the scope of this paper to derive in full the relationships between the fields and frequency deviations. Suffice it to say that it can be shown that the frequency deviation due to the insertion of a small spherical volume of dielectric material is proportional to the volume and to the square of the electric field at the point of insertion. Similarly it can be shown that the deviation due to a spherical volume of metal is proportional to the volume displaced and the difference between the square of the electric field and one-half the square of the magnetic field at the point in question. Expressed mathematically:

$$\Delta f_{\text{dielectric}} \propto \frac{E^2}{C^2} \times \text{volume} \qquad \text{(II-33)}$$

$$\Delta f_{\text{metal}} \propto \left(\frac{E^2}{C^2} - \frac{B^2}{2}\right) \times \text{volume} \qquad \text{(II-34)}$$

In practice the size of the sphere used must be small, partly in order to avoid errors due to nonuniform field distributions, and partly for theoretical reasons beyond the scope of this paper. Frequency shifts are generally in the audio range.

The following definitions and nomenclature will be used as a starting point:

Δf = frequency shift produced by a B-B

Δf_M, Δf_D = frequency shifts produced by a metallic and a dielectric B-B respectively

From Eqs. (II-33) and (II-34)

$$\Delta f_M = K_1 \left(\frac{E^2}{c^2} - \frac{B^2}{2} \right) \tag{II-35}$$

$$\Delta f_D = K_2 \frac{E^2}{c^2} \tag{II-36}$$

Substituting Eq. (II-36) in (II-35)

$$\Delta f_M = \frac{K_1}{K_2} \Delta f_D - K_1 \frac{B^2}{2} \tag{II-37}$$

Assuming a cavity with axial symmetry (operating in TM_{010} mode) there will be zero magnetic field on the axis and Eqs. (II-35) and (II-36) become:

$$\Delta f_{M\phi} = K_1 \frac{E^2}{c^2} \tag{II-38}$$

$$\Delta f_{D\phi} = K_2 \frac{E^2}{c^2} \tag{II-39}$$

or, dividing Eq. (II-38) by Eq. (II-39):

$$\frac{\Delta f_{M\phi}}{\Delta f_{D\phi}} = \frac{K_1}{K_2} \tag{II-40}$$

Substituting Eq. (II-40) into Eqs. (II-37) and (II-36) and rearranging:

$$B^2 = \frac{2}{K_1}\left[\Delta f_D\left(\frac{\Delta f_{M\phi}}{\Delta f_{D\phi}}\right) - \Delta f_M\right] \tag{II-41}$$

$$E^2 = \frac{C^2}{K_1}\left(\frac{\Delta f_{M\phi}}{\Delta f_{D\phi}}\right)\Delta f_D \tag{II-42}$$

In order to evaluate K_1 choose some other point in the cavity where $B \neq 0$ to be used as a calibration point. All measurements made at this point will be identified by the addition of a superscript prime. From Eq. (II-41):

$$K_1 = \frac{2}{B'^2}\left[\Delta f'_D\left(\frac{\Delta f_{M\phi}}{\Delta f_{D\phi}}\right) - \Delta f'_M\right] \tag{II-43}$$

We can now evaluate $\oint E \cdot d\ell$ of Section B above. In terms of actual measured values from Eqs. (II-42), (II-43):

$$E = \frac{CB'}{\sqrt{2}}\sqrt{\frac{\Delta f_{M\phi}}{\Delta f'_D\left(\frac{\Delta f_{M\phi}}{\Delta f_{D\phi}}\right) - \Delta f'_M}} \tag{II-44}$$

Then from Eq. (II-21):

$$\oint E \cdot d\ell = \frac{CB'}{\sqrt{2}}\left[\frac{\oint (\Delta f_{M\phi}) \cdot d\ell}{\sqrt{\Delta f'_D\left(\frac{\Delta f_{M\phi}}{\Delta f_{D\phi}}\right) - \Delta f'_M}}\right] \tag{II-45}$$

This completely describes the end-to-end voltage of the cavity in terms of the measured frequency deviations and the field at a single normalizing point.

We can obtain an expression for the magnetic field B in a similar manner. From Eqs. (II-41) and (II-43):

$$B^2 = B'^2\left[\frac{\Delta f_D\left(\frac{\Delta f_{M\phi}}{\Delta f_{D\phi}}\right) - \Delta f_M}{\Delta f'_D\left(\frac{\Delta f_{M\phi}}{\Delta f_{D\phi}}\right) - \Delta f'_M}\right] \tag{II-47}$$

This expression completely describes the magnetic field B at any point in the cavity in terms of the frequency deviations and the field at a single normalizing point.

E. Shunt impedance

The relations set forth in the preceding sections are sufficient to obtain an expression for the shunt impedance, Z_s. As a starting point we will assume the general expression for the power loss P_L:

$$P_L = \frac{V_{peak}^2}{2R} \qquad \text{(II-48)}$$

For a cavity, R is the shunt impedance which is a pure resistance at resonance (this is the only case of interest to us). Substituting and rearranging:

$$Z_s = \frac{V_{max}^2}{2P_L} \qquad \text{(II-49)}$$

All of the members of the right hand side of this equation have been derived above.

1. Using $\oint E \cdot d\ell$ of Eq. (II-17) and Eq. (II-16):

$$Z_s = \frac{\mu}{\pi f \delta} \left[\frac{(\oint E \cdot d\ell)^2}{\iint_{\Sigma S} (n \times B_t)^2 \, dS} \right] \qquad \text{(II-50)}$$

or in terms of the wave-length, λ :

$$Z_s = 3.494 \times 10^{-10} \sqrt{\lambda} \left[\frac{(\oint E \cdot d\ell)^2}{\iint_{\Sigma S} (n \times B_t)^2 \, dS} \right] \qquad \text{(II-51)}$$

2. In terms of magnetic fields only, using Eqs. (II-16) and (II-21):

$$Z_s = \frac{2\omega\mu}{\delta}\left[\frac{\left(\iint_{\text{field}} B \cdot dA\right)^2}{\iint_{\Sigma S}(n \times B_t)^2 \; dS}\right] \qquad \text{(II-52)}$$

or, in terms of the wave-length:

$$Z_s = \frac{1.241 \times 10^9}{\lambda^{3/2}}\left[\frac{\left(\iint_{\text{field}} B \cdot dA\right)^2}{\iint_{\Sigma S}(n \times B_t)^2 \; dS}\right] \qquad \text{(II-53)}$$

3. In terms of B-B measurements for the voltage, using Eqs. (II-16) and (II-45):

$$Z_s = \left[\frac{\mu_c 2}{2\pi f \delta}\right]\left\{\frac{B'^2\left[\oint(\Delta f_{M\phi}) \cdot d\ell\right]^2}{\left[\Delta f'_D\left(\frac{\Delta f_{M\phi}}{\Delta f_{D\phi}}\right) - \Delta f'_M\right]}\right\}\left[\frac{1}{\iint_{\Sigma S}(n \times B_t)^2 \; dS}\right] \qquad \text{(II-54)}$$

To carry out this computation it is necessary that the magnetic field measurements be normalized to the same check point as the B-B runs. Let the normalized fields be $B_{tN} = \frac{B_t}{B'}$. Then Eq. (II-54) becomes:

$$Z_s = 1.573 \times 10^7\sqrt{\lambda}\left\{\frac{\left[\oint(\Delta f_{M\phi}) \cdot d\ell\right]^2}{\left[\Delta f'_D\left(\frac{\Delta f_{M\phi}}{\Delta f_{D\phi}}\right) - \Delta f'_M\right]}\right\}\left\{\frac{1}{\iint_{\Sigma S}(n \times B_{tN})^2 \; dS}\right\} \qquad \text{(II-55)}$$

4. Using B-B measurements only, using Eqs. (II-45) and (II-47):

$$Z_s = \left[\frac{\mu_c 2}{2\pi f \delta}\right]\frac{\left[\oint(\Delta f_{M\phi}) \cdot d\ell\right]^2}{\iint_{\Sigma S}\left[\Delta f_D\left(\frac{\Delta f_{M\phi}}{\Delta f_{D\phi}}\right) - \Delta f_M\right] \cdot dS} \qquad \text{(II-56)}$$

or, in terms of the wave-length:

$$Z_s = 1.573 \times 10^7 \sqrt{\lambda} \frac{\left[\oint (\Delta f_{M\phi}) \cdot d\ell\right]^2}{\iint_{\Sigma S} \left[\Delta f_D \left(\frac{\Delta f_{M\phi}}{\Delta f_{D\phi}}\right) - \Delta f_M\right] \cdot dS} \qquad \text{(II-57)}$$

This gives us four different forms for computing the shunt impedance using various combinations of magnetic field measurements and B-B measurements for determining the voltage and power loss. In later sections the particular measurements for substitution into these equations will be described.

F. Determination of Q

In addition to the shunt impedance we can compute the Q of the cavity in terms of the magnetic field measurements and the B-B runs. One of the standard forms for the Q of a circuit is:

$$Q = \frac{\omega E_s}{P_L} \qquad \text{(II-58)}$$

where: E_s = Stored energy (joules)

P_L = Average power loss (watts)

Substituting from Eqs. (II-16) and (II-23):

$$Q = \frac{2}{\delta} \frac{\iiint_{volume} B^2 \cdot dV}{\iint_{\Sigma S} (n \times B_t)^2 \cdot dS} \qquad \text{(II-59)}$$

or, in terms of the wave-length:

$$Q = \frac{5.248 \times 10^5}{\sqrt{\lambda}} \frac{\iiint_{volume} B^2 \cdot dV}{\iint_{\Sigma S} (n \times B_t)^2 \cdot dS} \qquad \text{(II-60)}$$

In terms of the B-B runs of Eq. (II-47):

$$Q = \frac{5.248 \times 10^5}{\sqrt{\lambda}} \frac{\iiint_{volume} \left[\Delta f_D \left(\frac{\Delta f_{M\phi}}{\Delta f_{D\phi}} \right) - \Delta f_M \right] \cdot dV}{\iint_{\Sigma S} \left[\Delta f_D \left(\frac{\Delta f_{M\phi}}{\Delta f_{D\phi}} \right) - \Delta f_M \right] \cdot dS} \qquad \text{(II-61)}$$

G. Absolute fields, currents, and voltage

1. Fields

All of the field distribution measurements were made on a purely relative basis, i.e., the shape of the field was determined but the sampling probe did not give absolute values of the field. This relative distribution is sufficient for determining Z_s and Q of the model cavity but for purposes of scaling fields from the model to the full scale machine it was necessary to know the absolute value of the fields.

The absolute value of the magnetic field was determined by means of the voltage induced in a loop. Given a loop of radius, r, immersed in a uniform magnetic field, B. There will be a voltage V_L induced which will appear across the output terminals as shown in Fig. II-2. The relation

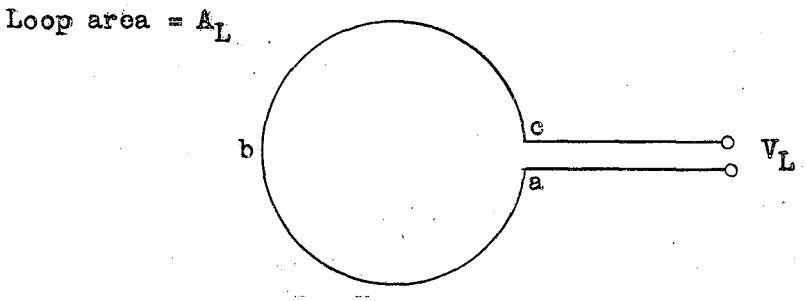

Field Calibration Loop

Fig. II-2

between the voltage induced and the field is given in Eqs. (II-17) and (II-21):

$$V = \oint_{a-b-c} E \cdot d\ell = -\omega \iint_{A_L} B \cdot dA \qquad \text{(II-62)}$$

where the surface integral is over the area of the loop. Assuming the field to be uniform over the loop and that the plane of the loop is perpendicular to the magnetic field vector:

$$V_L = \omega A_L B' \qquad \text{(II-63)}$$

$$B' = \frac{-V_L}{\omega A_L} \qquad \text{(II-64)}$$

A_L = Loop area (meters^2)

V_L = Loop voltage (peak)

B' = Max. magnetic field (webers/meter^2)

With certain special physical considerations which are related in detail in Section VI-D the right hand side of this equation can be determined and hence the magnetic field, B', at the position of the loop.

If we place the field sampling probe at the same point in the cavity as the loop and read its value, F', we can compute the absolute value of the field, $B(r,\theta,z)$, for any point in the cavity (provided of course that all the measurements were taken with the same probe at the same level of excitation). Let a superscript prime (B') indicate a value taken at the position of the loop:

$$B(r,\theta,z) = B' \left[\frac{F(r,\theta,z)}{F'} \right] \qquad \text{(II-65)}$$

where: $B(r,\theta,z)$ = absolute field at any general point (maxwells/meter^2)

$F(r,\theta,z)$ = probe measurement at any general point (proportional to the absolute field)

B' = absolute field at the loop position (maxwells/meter^2)

F' = probe measurement at the loop position

Define a normalized field value, F_N:

$$F_N(r,\theta,z) = \frac{F(r,\theta,z)}{F'}$$

In the measurements all readings were normalized in this manner so that the results would be independent of the level of operation. This also facilitated absolute field calculations as seen by substituting in Eq. (II-65):

$$B(r,\theta,z) = F_N(r,\theta,z)B' \qquad \text{(II-66)}$$

It is necessary only to determine the absolute field at the loop position by Eq. (II-64) to convert F_N to B.

2. Surface currents

The relation between fields and currents has already been set forth in Eq. (II-11):

$$I_S = n \times H_t$$

or, in terms of magnitudes only:

$$|I_S| = |H_t| = |B_t/\mu|$$

$$I_S = \frac{B_t}{4\pi} \times 10^7 \text{ amperes/meter (peak)} \qquad \text{(II-67)}$$

where B_t is the tangential magnetic field at the conducting boundary. Note that since all quantities are in terms of their peak values, if power is calculated from the currents a factor of one-half must be included.

3. Total end-to-end voltage

From Eq. (II-21) we can compute the end-to-end voltage of the cavity directly:

$$V = -\omega \iint_{\text{field}} B \cdot dA \quad \text{volts (peak)} \qquad \text{(II-68)}$$

The area of integration is the same as described in Section II-B. The integral can be evaluated from probe measurements which must be converted to absolute fields using Eq. (II-66).

H. Scaling factors

In predicting the operation of the full scale machine it is necessary to know the proper factors by which to multiply the information obtained from the model. In general it can be postulated that electric fields, magnetic fields, and currents will all scale with the same factor, S_F. This can be proved easily by noting that if it were not so, relative electric and magnetic fields in the two cavities would not be the same and this is obviously impossible. Also from Eq. (II-67) the magnitude of the current is equal to that of the magnetic field and hence current and fields must have the same scaling factor. The voltage scaling factor will be different from that of the field by the dimensional scaling factor, S_D, because $V = \oint E \cdot d\ell$ and $d\ell$ scales by S_D.

1. Dimensional scaling factor

The dimensional scaling factor is a design value and was chosen as one-tenth:

$$S_D = 1/10 \text{ , the dimensional scaling factor .} \qquad \text{(II-69)}$$

2. Voltage scaling factor

This is most easily deduced by comparing the end-to-end voltages of the two machines. Any other voltage will scale by this same factor because $V = \oint E \cdot d\ell$ and the field scaling factor is a constant and the dimensional scaling factor is a constant so that a combination of the two is a constant. Mathematically:

$$S_V = \frac{V_{FS}}{V_M} \qquad \text{(II-70)}$$

where: S_V = voltage scaling factor

V_{FS} = 45.18×10^6 volts = full scale end-to-end voltage

V_M = model end-to-end voltage

The model voltage, V_M, can be determined by using some of the results of other sections. From Eq. (II-21):

$$V_M = -\omega \iint_{\text{field}} B \cdot dS \qquad \text{(II-71)}$$

From Eq. (II-66) we can determine B in terms of the measured fields. Combining Eq. (II-66) with Eq. (II-64) and substituting in Eq. (II-71):

$$V_M = \frac{V_L}{A_L} \iint_{\text{field}} F_N \cdot dS \qquad \text{(II-72)}$$

where: A_L = 1.613×10^{-4} meter^2 (for the loop used)

V_L = monitor loop voltage

$\iint F_N \cdot dS$ = 1.163 (meters)^2 (measured)

then:

$$V_M = 7210\, V_L \qquad \text{(II-73)}$$

Then the scaling factor, S_V, is:

$$S_V = \frac{45.18 \times 10^6}{7.185 \times 10^3 \times V_L} = \frac{6.288 \times 10^3}{V_L} \qquad \text{(II-74)}$$

V_L = monitor loop peak voltage

3. Fields and current scaling factor

The most straightforward method for determining this factor, S_F, is to compute the average gradient along the centerline of each machine and take their ratio:

$$S_F = \frac{V_{FS}/L_{FS}}{V_M/L_M} = \left(\frac{V_{FS}}{V_M}\right)\left(\frac{L_M}{L_{FS}}\right)$$

where: L_M = length of the model

L_{FS} = length of the full scale machine

But this is simply

$$S_F = (S_V)(S_D) \tag{II-75}$$

where: $S_V = \dfrac{6.288 \times 10^3}{V_L}$

$S_D = \dfrac{1}{10}$

Then

$$S_F = \frac{628.8}{V_L} \tag{II-76}$$

I. Frequency changes resulting from perturbation of the cavity boundaries

In determining the frequency perturbations (Part XII) due to changes in the size and position of the walls and DT's, it was not possible to measure all the desired coefficients. However, Slater* treats this problem from a theoretical standpoint and arrives at results which are directly applicable to our case. Slater's Eq. (7.1) on page 81 is:

$$\omega^2 = \omega_a^2 \left[1 + \int_{\Delta V} (H_a^2 - E_a^2)\, dV \right] \tag{II-77}$$

where: ω_a = frequency of the cavity in its unperturbed state

ω = frequency of the cavity after perturbing one of the boundaries

$\int_{\Delta V} dV$ = integral over the change in volume, V, effected by the perturbation of the boundary

E_a = electric field distribution over the change in volume normalized to $\int_V E_a^2 \cdot dV$ † = 1 (Note: this integral is over the entire cavity volume.)

---

* J. C. Slater, "Microwave Electronics," D. Van Nostrand Company, Inc., 1950.

† Loc. cit., p. 61.

H_a = magnetic field distribution over the change in volume normalized to $\int_V H_a^2 \, dV = 1$ (integrated over the entire cavity volume.)

Rewriting Eq. (II-77) and taking the square root:

$$f = f_a \left[1 + \int_{\Delta V} (H_a^2 - E_a^2) \, dV \right]$$

Assuming that $F(E,H) \ll 1$ (a very good assumption for perturbations small compared to linear dimensions of the cavity) we can expand by the binomial theorem:

$$f = f_a \left[1 + \frac{1}{2} \int_{\Delta V} (H_a^2 - E_a^2) \, dV \right]$$

Then:

$$\Delta f = (f - f_a) = \frac{f_a}{2} \left[\int_{\Delta V} (H_a^2 - E_a^2) \, dV \right]$$

$$\Delta f = \frac{f_a}{2} \left[\int_{\Delta V} H_a^2 \, dV - \int_{\Delta V} E_a^2 \, dV \right] \qquad \text{(II-78)}$$

We can interpret the right hand members of this expression as Δf_H and Δf_E, the frequency deviations due to the magnetic and electric fields respectively. Then:

$$\Delta f = \Delta f_H - \Delta f_E \qquad \text{(II-79)}$$

If both the electric and magnetic fields are known over the region of perturbation this is a straightforward computation. For our case, only the magnetic distributions were known directly from measurements, but it was possible to obtain a reasonable approximation of the electric field perturbation for the cases desired. Actually only two such cases were used:

Case 1. Region where $E_a^2 << H_a^2$.

For this case Eq. (II-78) becomes:

$$\Delta f = \Delta f_H = \frac{f_a}{2}\left[\int_{\Delta V} H_a^2 \cdot dV\right] \qquad \text{(II-80)}$$

In terms of the normalization factor:

$$\Delta f = \frac{f_a}{2}\,\frac{\int_{\Delta V} H^2 \cdot dV}{\int_V H^2 \cdot dV} = \frac{f_a}{2}\,\frac{\int_{\Delta V} B^2 \cdot dV}{\int_V B^2 \cdot dV}$$

The denominator is completely determinable from the measurements for the stored energy (see Eq. (II-23)) and the numerator can be evaluated from the field plots in the region of the desired perturbation.

Case 2. Δf_E not negligible, but measureable approximately as a frequency difference. (This is valid only in regions where $E \gg H$). For this case Δf_H for the entire region is determined as in Case 1 and the measured $\Delta f \sim \Delta f_E$ can be subtracted

Actually the magnetic fields could be calculated for every point in the cavity from the measured field distributions and some reasoning. From the magnetic fields, the electric fields could be calculated and hence Δf_E determined. However, such a process would be laborious and the accuracy required could be obtained by the method outlined above.

J. Conducting rod in a uniform field

The drift tube stems perturb the fields locally. It is possible to obtain the new magnetic field distributions due to the insertion of the stems analytically.

Stratton* derives expressions for the field distributions around an

---

* Stratton, Electromagnetic Theory, McGraw-Hill, 1941 1st ed., p. 261.

infinite rod inserted in a uniform magnetic field with the axis of the rod perpendicular to the field.

$$\left.\begin{aligned} H_r &= H_o \left(1 + \frac{\mu_1 - \mu_2 a^2}{\mu_1 + \mu_2 r^2}\right) \sin\theta \\ H_\theta &= -H_o \left(1 - \frac{\mu_1 - \mu_2 a^2}{\mu_1 + \mu_2 r^2}\right) \cos\theta \end{aligned}\right\} \qquad \text{(II-81)}$$

where: μ_1 = permeability of the rod

μ_2 = permeability of the medium

a = radius of the rod

r, θ = variables of position in cylindrical coordinates.

It should be noted that these formulae are derived for the magnetostatic case, but for a rod small compared to wave-length they are applicable for time varying fields.

Assuming a perfectly conducting rod, i.e., $\sigma = \infty$, no fields exist inside the rod and hence it behaves as if $\mu_1 = 0$. (This will be a reasonably good approximation provided $\omega\sigma$ is very large, i.e., the skin depth, $\delta \to 0$.)

$$\left.\begin{aligned} H_r &= H_o \left(1 - \frac{a^2}{r^2}\right) \sin\theta \\ H_\theta &= H_o \left(1 + \frac{a^2}{r^2}\right) \cos\theta \end{aligned}\right\} \qquad \text{(II-82)}$$

For the special case of the fields at the surface of the rod, $r = a$:

$$\left.\begin{aligned} H_r &= 0 \\ H_\theta &= 2 H_o \cos\theta \end{aligned}\right\} \qquad \text{(II-83)}$$

Then there is only a tangential field present at the surface as expected.

The currents flowing in the rod can be calculated using Eqs. (II-67)

and (II-83):

$$I_S = \frac{B}{2\pi} \times 10^7 \cos \theta \qquad \text{(II-84)}$$

B = field without rod present.

III MECHANICAL DESIGN

The model cavity was designed to scale as nearly as was practical the full scale machine. The notable exceptions were the manner in which the DT's were supported, the slots and holes required for making the various measurements, the design of the bypass capacitors on the stems, and the construction of the cavity in two sections, 126° upper and 234° lower, for rapid disassembly.

The liner, a 16 sided, tapered tank, was made of 1/16 in. copper sheet throughout. In cross section, it is an irregular, inscribed polygon symmetrical about the X and Y axes (see Figs. III-1, III-2, E-1). A 1 inch flange around the opening of each section provided a means for clamping the two parts together. Cleco sheet metal clamps were used for this purpose.

The ends of the liner, designed flat, were provided with a ± 2 1/2 in. full scale "oil can" motion for minor frequency adjustments. This was accomplished by attaching the ends solidly to the frame of the cavity by means of push screws from the frame to a ring around the center hole. Brass angle irons ran radially out from the ring to stiffen the copper sheet and to transfer the "oil can" motion evenly.

The cavity was first constructed with 7 1/2 DT's but was subsequently changed to 8 1/2 DT's for design considerations. The 8 1/2 DT layout is given in Fig. III-3. Since the cavity was handled in exactly the same way for the 7 1/2 M and 8 1/2 M and inasmuch as the measurements on the 8 1/2 M are the ones which are of interest to us here, only the latter will be considered in detail. It should be mentioned, however, that in converting from 7 1/2 M to 8 1/2 M the liner which had the proper scale for 7 1/2 drift tubes became 2 1/2 in. too long full scale for 8 1/2 drift tubes, though it scaled in all other dimensions. This is discussed in Section XII

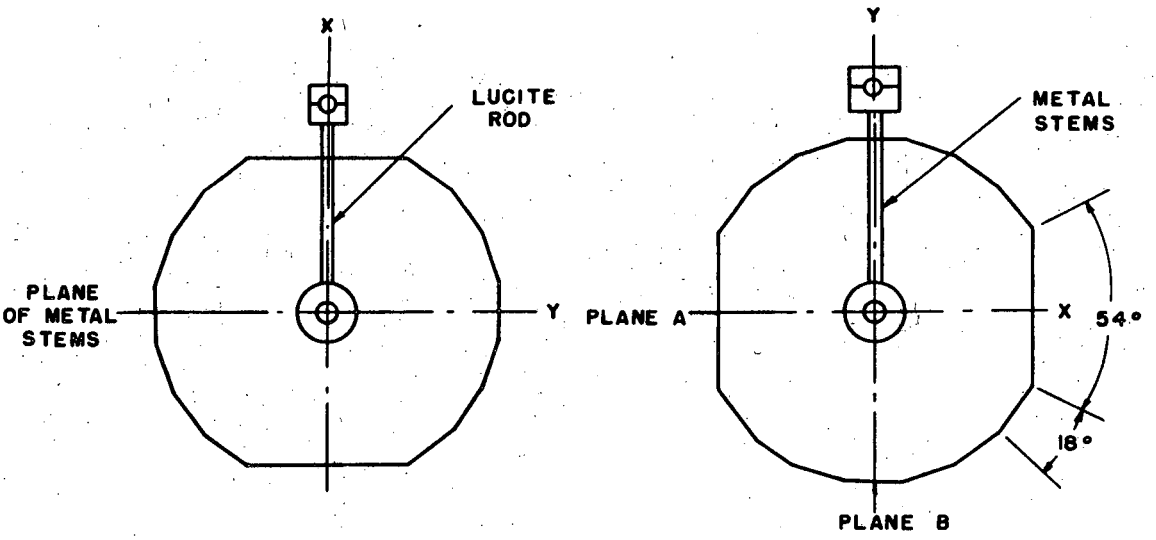

CAVITY ORIENTATION FOR STEM POSITION DETERMINATION

(a)

CAVITY ORIENTATION FOR FIELD MEASUREMENTS

(b)

FIG. III-1

MU 1528

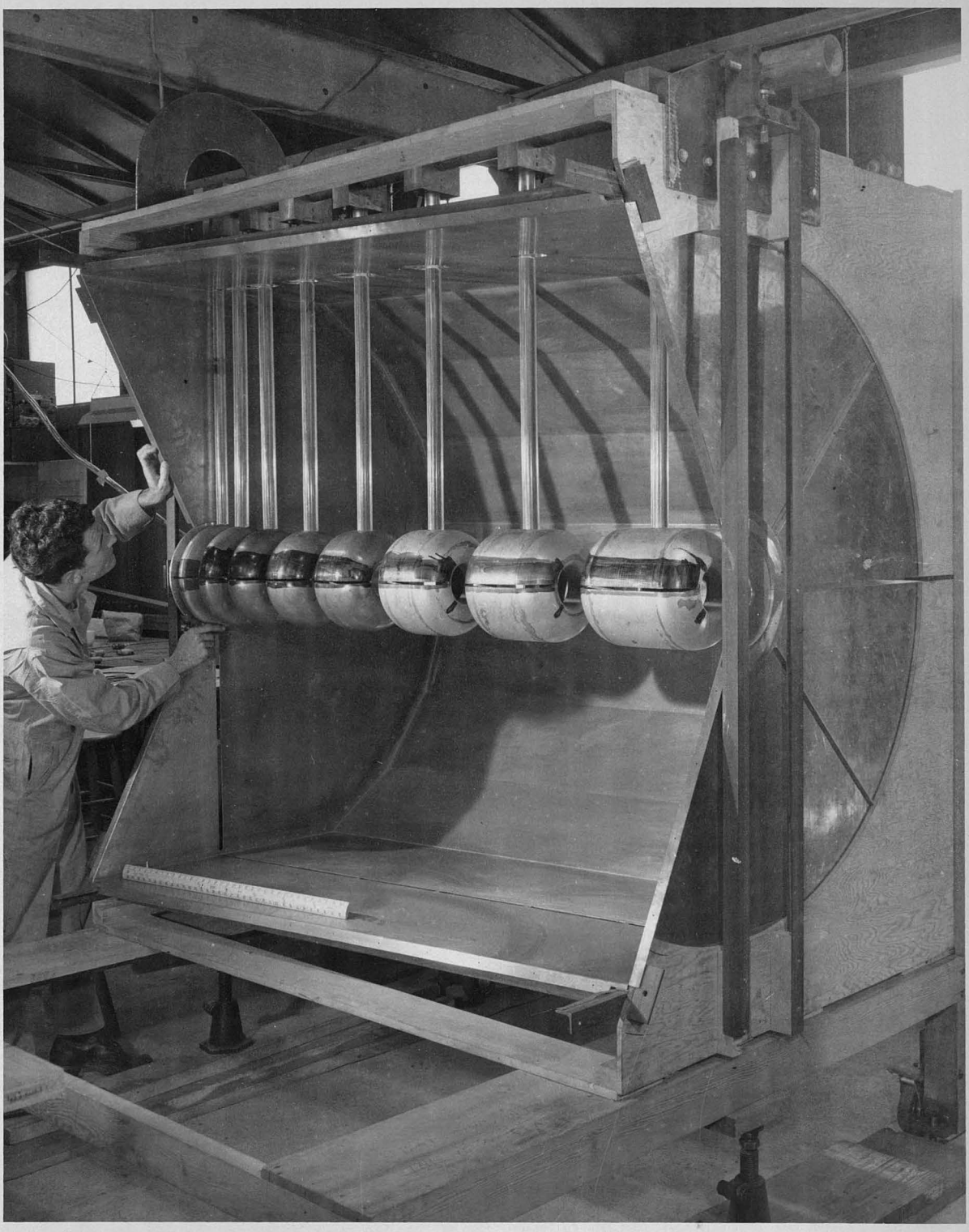

$\frac{1}{10}$ SCALE MODEL CAVITY WITH 126° SECTION REMOVED TO SHOW DRIFT TUBES SUPPORTED ON LUCITE RODS

FIG. III - 2

OZ 1063

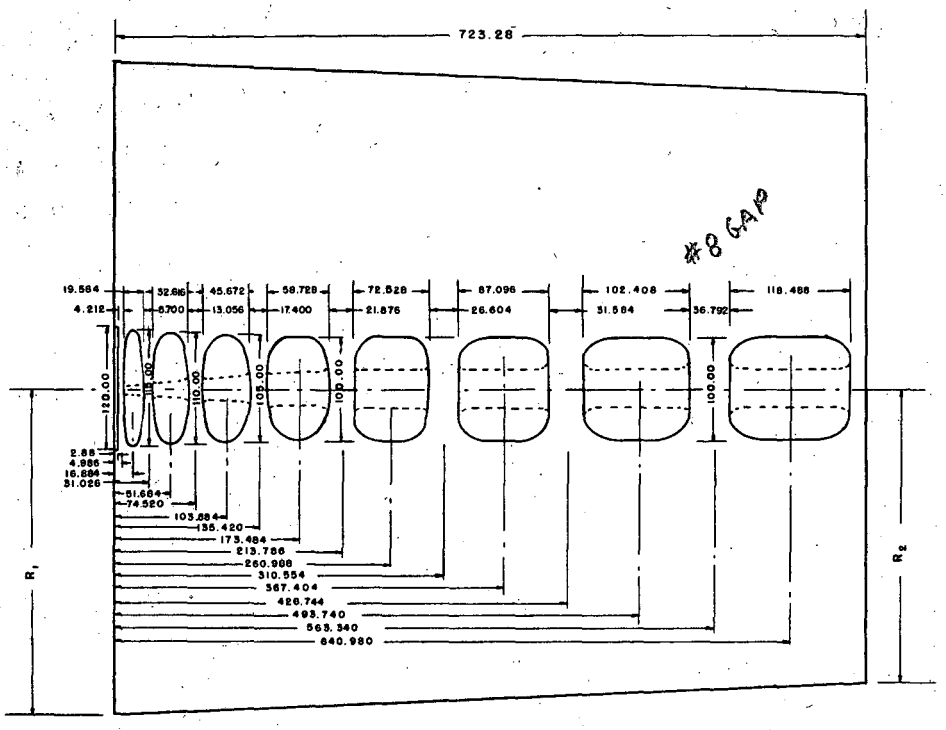

	A-PLANE	B-PLANE
R_1	315.47	349.69
R_2	283.28	312.46

FOR LINER DETAIL SEE UCRL SKETCH # 203-1166A

FOR DRIFT TUBE DETAIL SEE UCRL LAYOUT # 26475A

DRIFT TUBE LAYOUT

FIG. III-3

MU1529

on Frequency and Perturbations.

For locating stem positions the cavity was placed on its side. This allowed the stem positioning to be done in the same plane in which the metal stems would be located in the final orientation (see Figs. III-1a, III-2). The drift tubes were supported on 1 3/4 in. diameter (model dim.) lucite rods from a common horizontal stainless steel tube mounted above the liner. Brass movable stems (as shown in Fig. IX-4) were introduced into the cavity at right angles to the lucite rods through 2 in. (model dim.) slots provided for the purpose. A detailed account of the stem position determination is given in Section IX.

After the stem positions were located, by-pass capacitors were installed on the movable stems. The voltage across the capacitor was measured as a function of capacity. Capacitor voltages were also measured with the stem and drift tube translated along the axis of the cavity.

The next operation was to rotate the cavity to its correct orientation (Fig. III-1b) and mount the DT's on metal stems. In this case the stems were suspended from a horizontal bakelite rod for insulating purposes.

When the metal stems were installed, scaled liner nozzles were installed for each stem position to more nearly approximate the full scale liner. The by-pass capacitors were mounted on top of the nozzles as shown in Fig. III-4. The cross section of the nozzles is given in Fig. III-5. A table of nozzle lengths is given in Table III-1. With this configuration, by-pass capacitor voltage was measured as a function of the axial perturbation of the DT position with the outer end of the stem constrained.

The DT's were made of brass. Because of size, they were machined in sections and soft soldered together. A 1/4 in. slot (model dim.) was cut lengthwise in all DT's to facilitate field distribution measurements. During

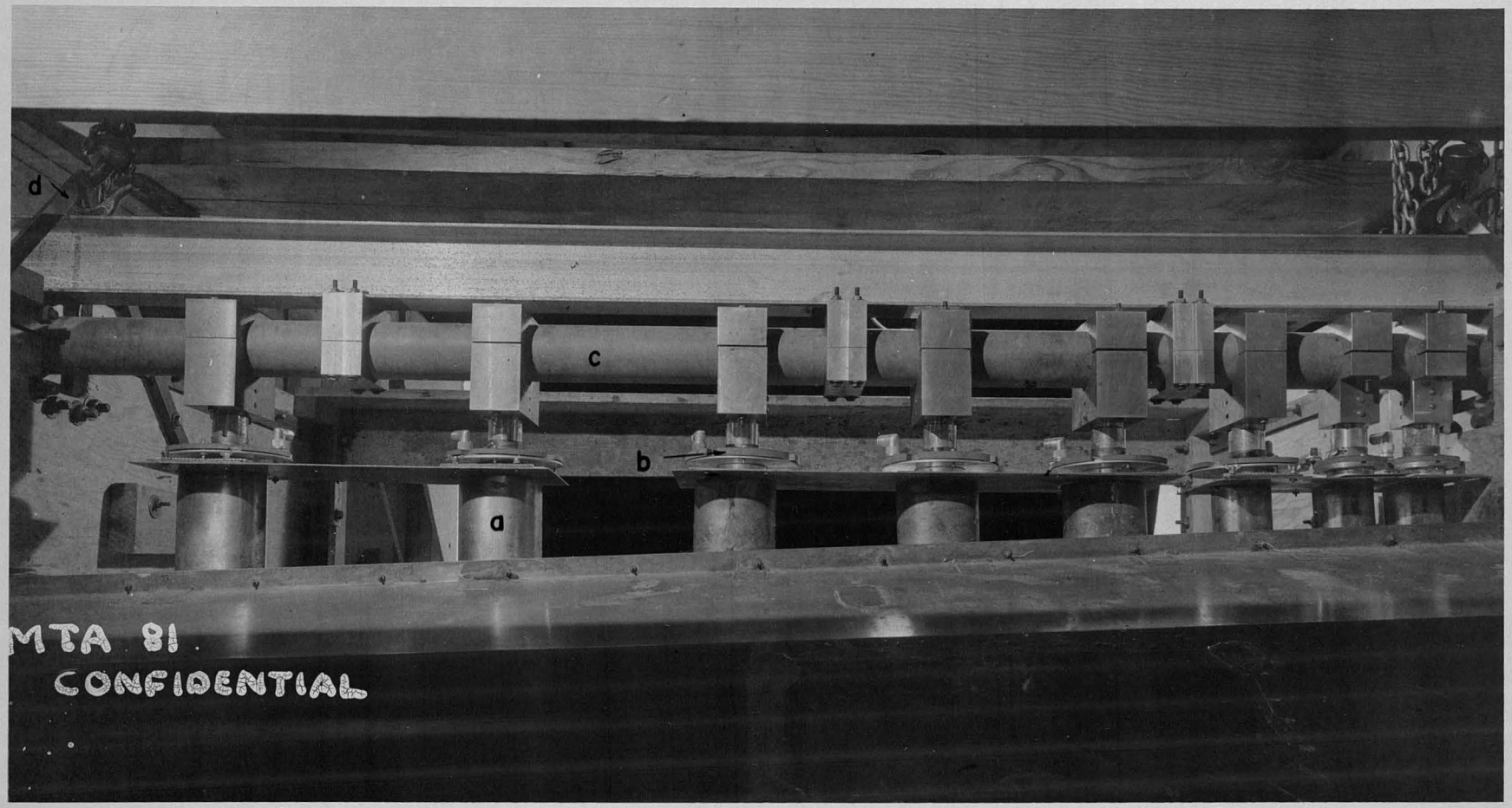

(a) LINER NOZZLES
(b) STEM BY PASS CAPACITORS
(c) PLASTIC SUPPORT BEAM
(d) LIFTING EYE

1/10 SCALE MODEL STEM SUPPORT ASSEMBLY

FIG. III-4

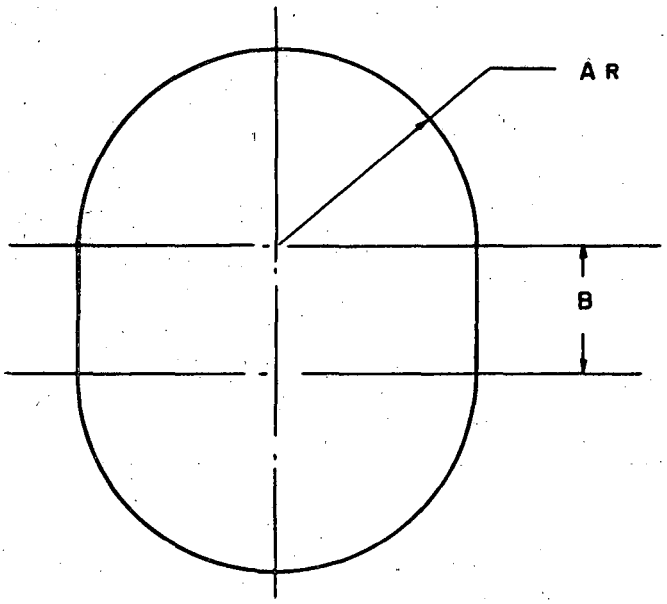

# 1 - 3 INCL	# 4 - 8 INCL
A = 11"	A = 16"
B = 7"	B = 10"

LINER NOZZLE SECTIONS

FIG. III-5

MU 1530

Liner Nozzle Lengths (Full Scale)

Table III-1

DT Number	Nozzle Length (In.)
1	35.190
2	36.908
3	39.486
4	42.923
5	47.244
6	52.500
7	58.739
8	66.010

Liner Taper = 0.04938 ft/ft

the conversion from 7 1/2 M to 8 1/2 M it was decided to silver plate the DT's and stems to give a better conductivity than that of brass. No great effort was made to obtain absolutely smooth DT surfaces before plating because it was thought that it was not warranted at that time. It was not until later that it was found that a considerably more accurate determination of Z_s and Q could be obtained than had been desired or thought possible at the outset, considering time and facilities available. The metal stems, also brass, were silver plated before they were soft soldered to the DT's. This, again, was done because it was thought that initial requirements did not warrant building up special equipment necessary for plating the DT and stem as one unit.

When the prospect of refining the measurements arose, the condition of the DT surfaces became a primary consideration. It was thought that the losses in the DT's caused by small scratches in the surface and those caused by the soft solder joints at the base of the stems might contribute appreciably to the difference between the measured Q and that calculated from the field distributions. Also some work by Leslie J. Cook on silver plating (UCRL-1068) indicated that the rf conductivity of the silver on the DT's and stems could be of the order of 50 percent of theoretical as a result of bad plating and buffing. Therefore it was decided to replate the DT's with stems attached to: (a) improve the surface of the DT's, (b) attempt to improve the conductivity of the silver, and (c) cover the soft solder joints. The separate effects of the above are not known, but by careful plating, the measured Q of the cavity was brought to within 2 probable errors of that obtained from the field plots. Fig. III-6 shows the 1/10 scale model cavity with the 234° section removed to show the silver plated DT's and stems. An account of the plating procedure is given in Appendix A.

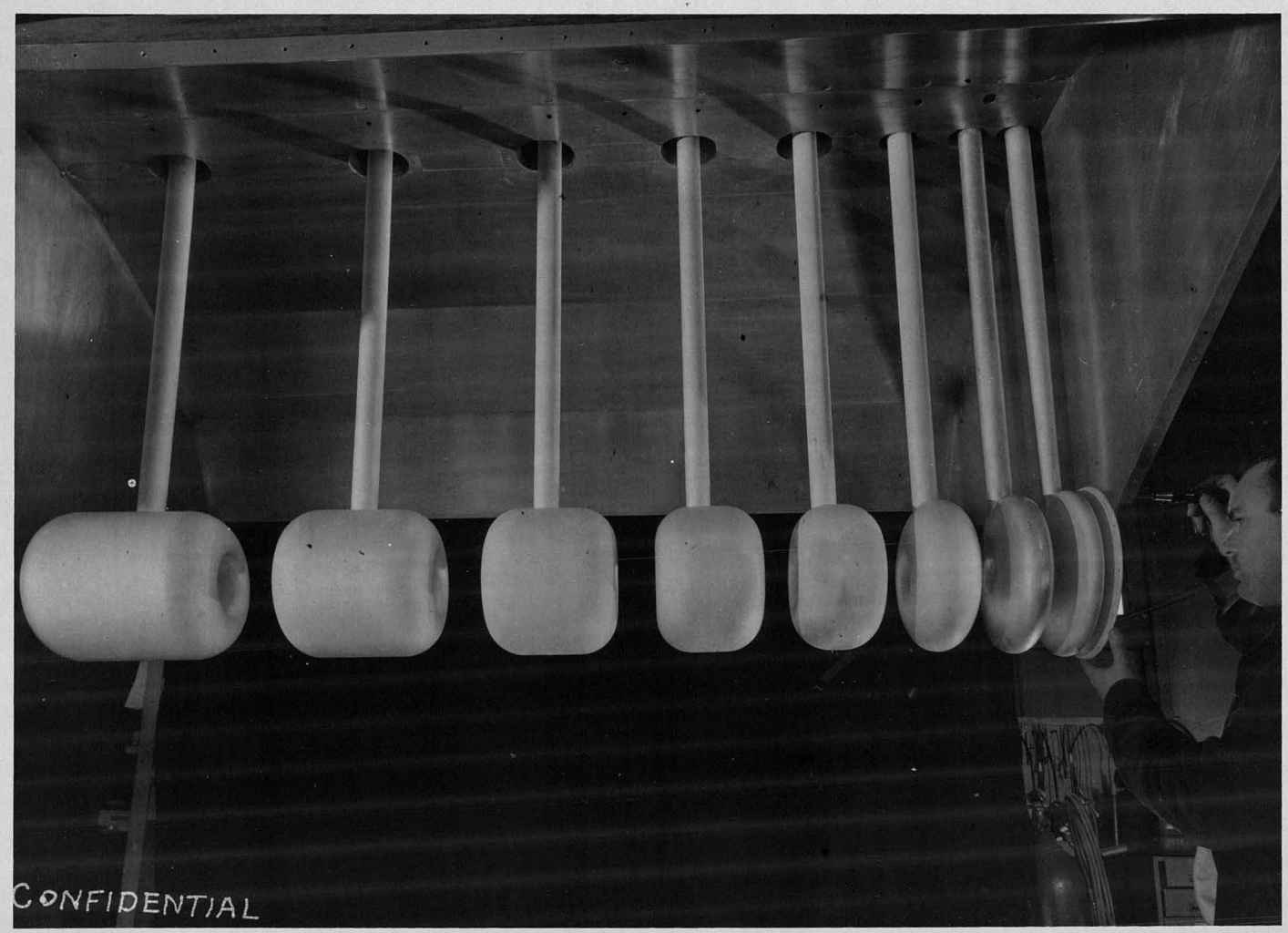

1/10 SCALE MODEL CAVITY WITH LOWER SECTION REMOVED TO SHOW THE DRIFT TUBES SUPPORTED BY METAL STEMS IN THE FINAL SILVER PLATED CONDITION.

FIG. III-6

The liner was built to a ± 1/16 in. (model dim.) tolerance. The tolerances on the DT's were ± 0.002 in. on the lengths and ± 0.005 in. (model dim.) on all other external dimensions. The diameter of the stems also had a tolerance of ± 0.005 in. (model dim.). Both the lucite and the metal stems were attached to the DT's in a jig which gave a tolerance on the length of the stems of ± 0.005 in. (model dim.) (see Fig. III-7). This proved useful in aligning the DT's as is discussed in the following section on Mechanical Adjustments.

DRIFT TUBE AND STEM ASSEMBLY JIG

FIG. III - 7

IV MECHANICAL ADJUSTMENTS

A. Ends

Although the ends of the liner were provided with an "oil can" motion for minor frequency adjustments, it was not needed and the measurements were made with the ends flat. The flatness gauge is shown in Fig. IV-1. The tolerance on the flatness was ± 1/16 in. (model dim.). Adjustments were made with push screws on the ring around the center hole.

B. Drift tubes

1. Cathetometer

By assembling the DT's and stems in a jig and suspending them from a common support as mentioned in the previous section, DT positioning in the liner was confined to two adjustments. The first adjustment, and the most critical of the two, was the axial spacing of the DT's with a cathetometer. The second adjustment consisted of aligning the DT's on a common axis by rotating the DT and stem about the support. For this adjustment silk cross hairs were fastened to each end of the DT's with Duco household cement. To make the axis of the DT's coincide with the axis of the liner, the DT support was provided with horizontal and vertical adjustments on either end.

The DT alignment set up is shown in Fig. IV-2. Before the alignment could be made, the cavity had to be leveled. Cross hairs were installed in the center of each end of the liner and the leveling was done with a dumpy level. Then the line of sight of the telescope on the cathetometer was adjusted perpendicular to the axis of the liner and at the proper height to pass through the 2 in. (model dim.) slot in the liner, to the DT's. Because the DT's could not be aligned with one cathetometer position, a bench

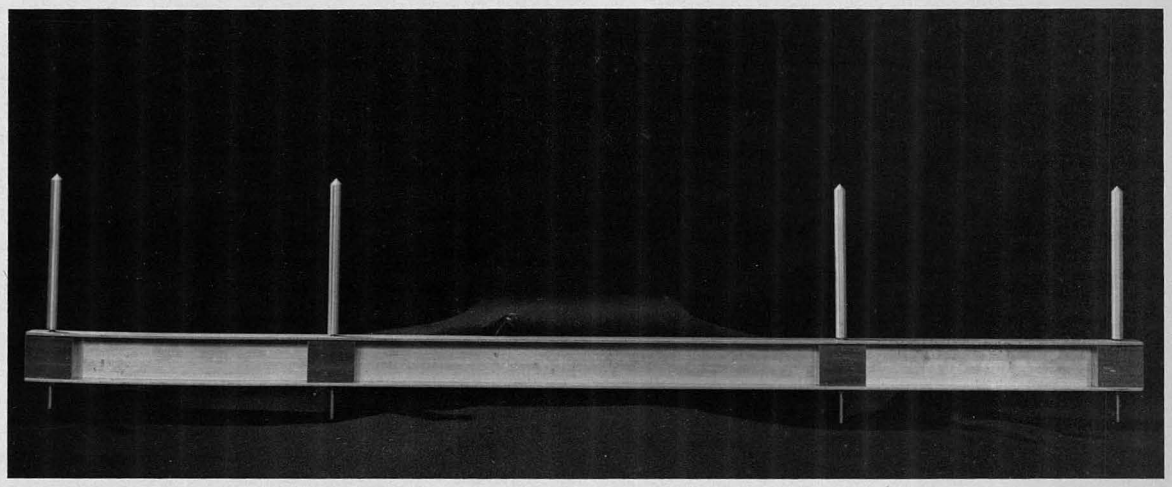

FLATNESS GAUGE FOR CAVITY ENDS

FIG. IV-1

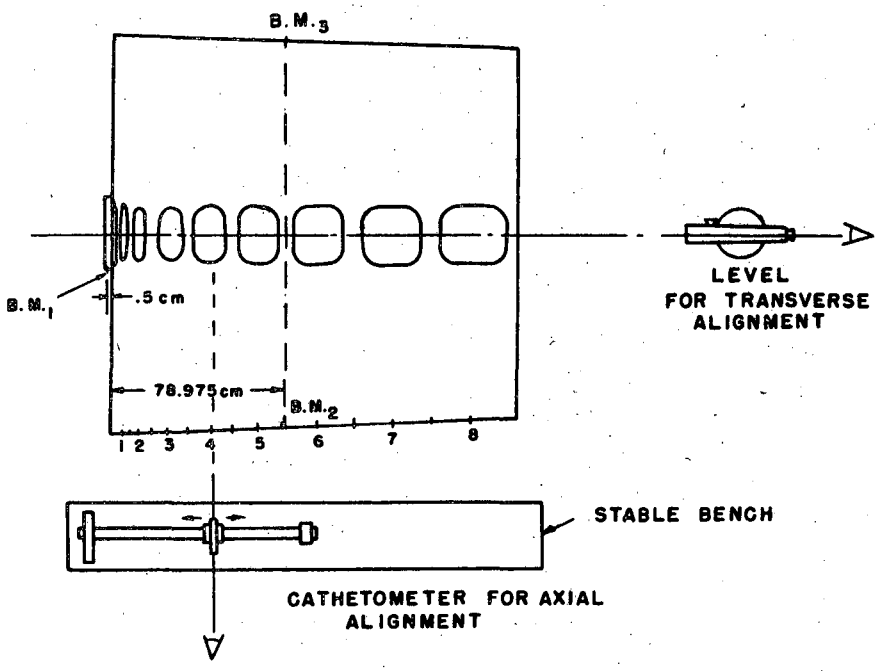

DIMENSIONS ARE FOR MODEL

MECHANICAL ALIGNMENT OF DRIFT TUBES

FIG. IX-2

MU1531

mark was scribed in each side of the liner such that a vertical plane passed through the two points would be perpendicular to the axis of the cavity. Thus, with the liner and cathetometer leveled, setting up on the two bench marks insured that the motion of the cathetometer telescope would be parallel to the axis of the cavity.

DT alignment was, then, a three man job; one man on each optical instrument and one man above the cavity to move the drift tubes. A transverse center line was scribed on the side of each DT nearest the cathetometer. This center line was visible to the cathetometer through the 2 in. (model dim.) slot in the liner. When the brass movable stems were placed in the slot, it was necessary to raise the cathetometer and sight through holes placed in the liner above each stem position. The positions of the DT's were set with respect to Bench Mark #2. Bench Mark #1 was placed on the cavity to facilitate locating the position of DT #0.

2. Analysis of accuracy

The accuracy of the axial alignment of the DT's was determined by the repeatability of the cathetometer readings. A series of 10 readings between two fixed points on the cavity by each of 5 people demonstrated that the readings could be repeated only to $\pm$ 0.3 mm (model dim.). This was not due exclusively to reading error. The effects of vibrations in the cavity and the building contributed.

Looking again at Fig. IV-2, the cathetometer was set up about 3 feet from Bench Mark #2 or about 9 feet from Bench Mark #3. If a 0.3 mm (model dim.) error were made at both bench marks and if the errors were in the opposite direction, the cathetometer would still be perpendicular to the axis of the cavity within an angle of 1 minute. Such an error is insignificant.

The tolerance on the transverse alignment was set at $\pm$ 1/16 in. (model

dim.), though it was for the most part better. For the effect of alignment accuracy on frequency, see Section XI, Frequency and Perturbations.

Since DT positions did change, especially while supported on lucite stems, the alignment was checked before every critical measurement. In the case of the lucite stems the axial tolerance was relaxed to ± 0.5 mm (model dim.) because of the cold flow in the lucite caused by the weight of the DT.

V OSCILLATORS

A. Power requirements

The electromagnetic fields to be measured in a cavity must be established by means of a high frequency oscillator. The main requirements of such an oscillator are (a) frequency stability, (b) amplitude or output stability, and (c) sufficient power output.

It is the usual practice to obtain frequency stability when using a resonant cavity as the oscillator load by allowing the cavity to act as the frequency determining element of the oscillator. This can be accomplished by tightly coupling the grid and plate circuits to the cavity. This type of oscillator is often referred to as a locked-in oscillator.

Amplitude stability can be obtained by providing suitable voltage regulation for the various power supplies that may be necessary to operate the oscillator.

The power requirements for field measurements are not large and it is therefore unnecessary to exercise extreme caution as far as efficiency, cooling, and operating costs are concerned in the design of an oscillator for exciting model cavities.

The amount of power necessary to make satisfactory measurements in a cavity can be determined approximately in the following manner. The voltage V_L induced in a loop inserted in the cavity is given by Eq. (II-63):

$$V_L = B_L \omega A_L \tag{V-1}$$

Further, the end-to-end voltage, V_C, of the cavity is, from Eq. (II-21)

$$V_C = \omega \iint_{\text{field}} B \cdot dA \tag{V-2}$$

As an approximation (good enough for our purposes) let

$$\iint B \cdot dA = B_L A_{field} \qquad (V\text{-}3)$$

B_L = magnetic field at the loop of Eq. (V-1)

A_{field} = cavity area bounded by the liner walls and the center line.

Then $$V_C \approx \omega B_L A_{field} \qquad (V\text{-}4)$$

and from Eq. (V-1)

$$V_C \approx \frac{\omega A_{field}}{A_L} (V_L) = \frac{V_L A_{field}}{A_L}$$

From Eq. (II-49) the power loss can be written:

$$P_L \approx \frac{V_C^2}{2Z_s}$$

or

$$P_L \approx \frac{V_L^2}{2Z_s} \left[\frac{A_{field}}{A_L}\right]^2 \qquad (V\text{-}5)$$

This requires that an estimate be made of the shunt impedance, Z_s, of the cavity. This is usually possible within a factor of two. As a practical example consider the 8 1/2 DT model cavity. If we assume a pick-up loop of area 0.10 inch^2 and that we can work with induced voltages in the loop of the order of one volt at the maximum field point we have the quantities:

$$V_{loop} = 1 \text{ volt}$$

$$Z_s \approx 30 \times 10^6 \text{ ohms}$$

$$\text{Area loop} = 0.10 \text{ inch}^2$$

$$\text{Area cavity} \left(\frac{60'' \times 72''}{2}\right) \approx 2{,}000 \text{ inches}^2$$

From Eq. (V-5),

$$P_L \approx \frac{1}{60 \times 10^6} \left(\frac{2 \times 10^3}{10^{-1}}\right)^2 = 6.7 \text{ watts}$$

Conservatively, one might say that a 20 or 30 watt oscillator would be satisfactory for this purpose when inefficiencies in the coupling system are taken into account.

B. APT-4 transmitter

The ordinary commercial high frequency signal generator has a power output of the order of milliwatts. Also it will not operate as a locked-in oscillator on a cavity without severe modifications. Therefore, the use of such signal generators could not be considered for this application.

Attention was drawn to the APT-4 airbourne radar transmitter which was a fairly common commodity on the surplus market. This transmitter is capable of supplying about 100 watts of power at frequencies of around 200 megacycles per second. The oscillator tube in the APT-4 is a split anode magnetron. If the output of the transmitter is coupled into a cavity and the frequency control adjusted until fields appear in the cavity, the nature of the magnetron operation is such that locked in oscillations occur, and the power level in the cavity will remain essentially constant, even though the frequency of the cavity is shifted slightly by inserting a paddle or distorting the walls.

For operation at frequencies in the vicinity of 100 megacycles it was necessary to load the tuning line of the magnetron by adding a small capacitor close to the base of the tube. This loading capacitor must be rated for 1000 volts at 100 mc, have a capacity of 10 micromicrofarads, and still be small enough so it does not upset the symmetry of the transmission line. It was necessary to design a special air-spaced condenser for this purpose.

A large number of satisfactory field measurements were made on various

cavities using the APT-4 transmitter; however, there were several factors which made its use somewhat difficult. Since the APT-4 is designed for airbourne operation it is necessary to use a 400 cycle generator as a power supply. From a dependability standpoint, trouble was experienced with the blower motor bearings, the water pump in the heat exchanger, the water flow interlock, and the case interlocks. From an operating standpoint, some difficulty was experienced with the output level changing during measurements.

C. Cavity oscillator

The limitations of the APT-4 transmitter and an increase in scope of the field measurement program made it advisable to design and build an oscillator for use in exciting the cavities.

A grounded grid oscillator using an Eimac 35-TG triode was constructed. A schematic of this oscillator is shown in Fig. V-1. The resonant circuits associated with the plate and cathode consisted of variable air-spaced condensers, and the inductances consisted of single loops which were inserted into the cavity through slots. Photographs of this oscillator are shown in Fig. V-2a and V-2b. The oscillator could be operated with from 300 to 1500 volts on the plate. Typical operating conditions for 1000 volts on the plate are:

Plate voltage	1000 volts d.c.
Plate current	170 ma d.c.
D.C. power	170 watts
Grid current	60 ma d.c.
Grid bias	150 volts d.c.

The following quantities were calculated from pyrometer measurements of plate temperature and are only approximate:

R F power output (tube)	63 watts (calculated)
Plate dissipation	110 watts (calc.)

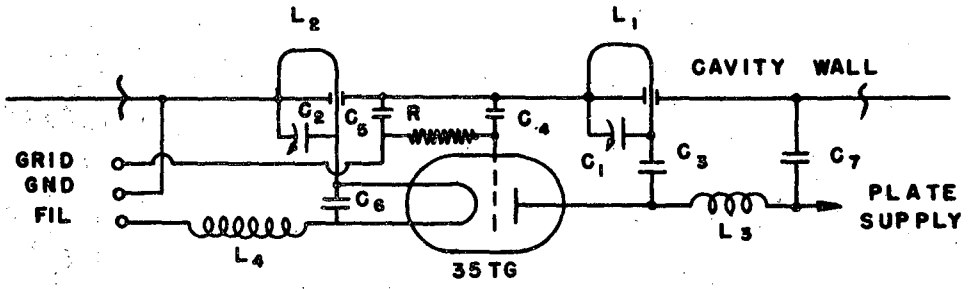

L_1 = PLATE LOOP
L_2 = CATHODE LOOP
L_3 = 10 μh 250 Ma
L_4 = 20 TURNS # 16 ½" DIA. ½" LONG
R_1 = 2500Ω, 10 W

C_1 = 13 μμf 4.5 KV AIR VARIABLE
C_2 = 50 μμf 1 KV " "
C_3, C_4 = SPECIALLY DESIGNED BLOCKING CAPACITOR APPROX. 500 μμf 3 KV
C_5, C_6 = 300 μμf 250 V SILVER-BUTTON MICA
C_7 = 0.002 μf 2.5 KV MICA

OSCILLATOR SCHEMATIC
FIG. V-1

MU 1532

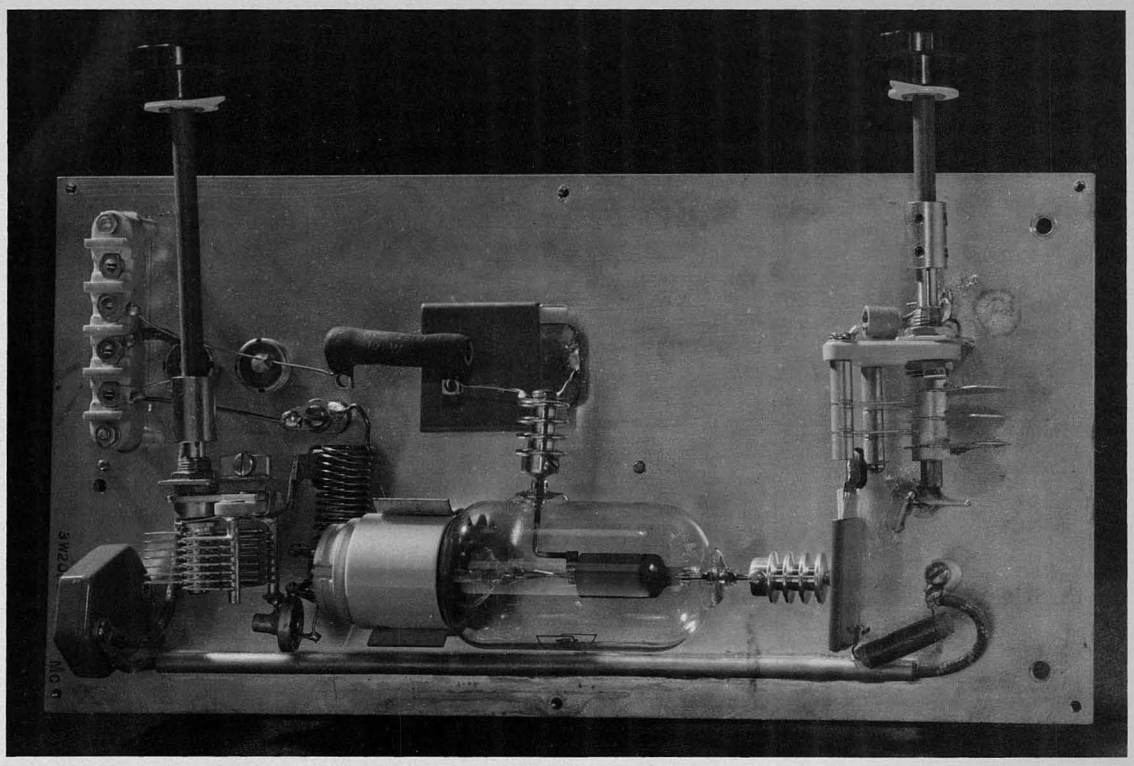

a

CAVITY OSCILLATOR FRONT VIEW

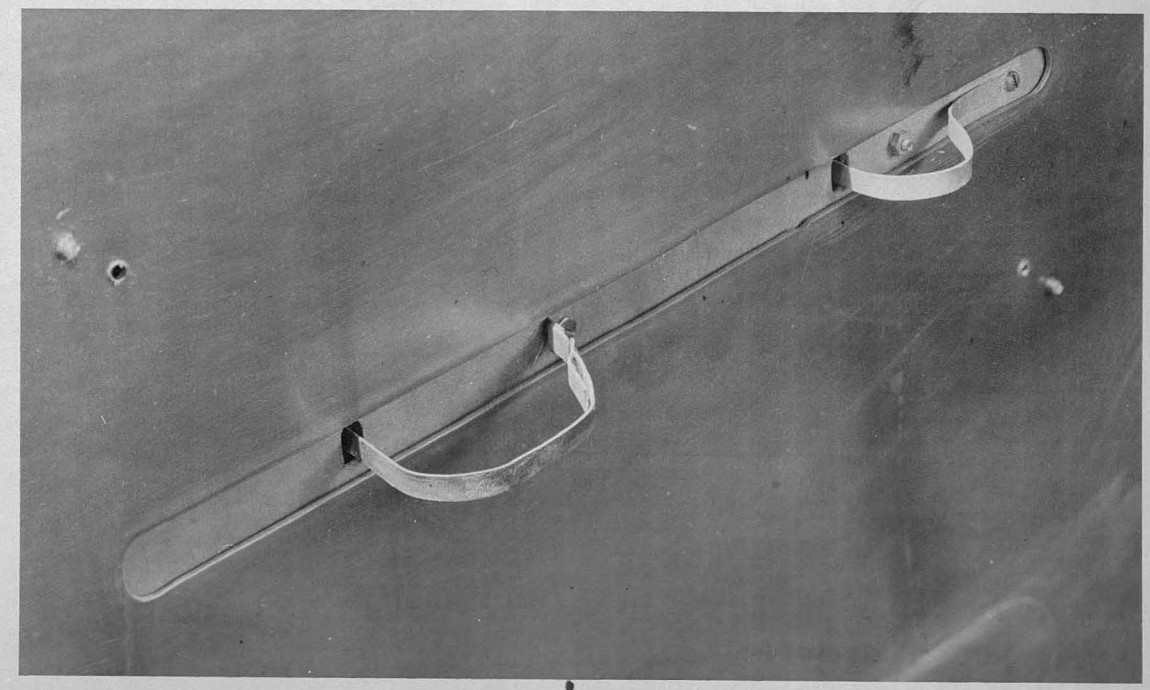

b

OSCILLATOR LOOP (INSIDE CAVITY)

FIG. V-2

OZ 1085

Plate efficiency	63 percent (calc.)
Plate current flow angle	134° (calc.)
Peak plate current	700 ma (calc.)
Average plate current	300 ma (calc.)
Peak rf voltage	425 volts (calc.)
Load impedance	1420 ohms
Loaded tank circuit Q	19
Circulating tank circuit current	5.7 amperes peak
R F power dissipated in tank circuit	47 watts
Power supplied to cavity	16 watts

A remote grid keyer was built to turn off the oscillator while the zero adjustment of the measuring equipment was being done. A schematic of the grid-keyer is shown in Fig. V-3. It was found that appreciable 60 cycle amplitude modulation occurred in the output of the oscillator at low level when the filament of the 35-TG tube was operated from a filament transformer, so a storage battery was used as a filament supply. The plate supply was regulated by means of a series regulator. A diagram of the power supply is shown in Fig. V-4. UCRL drawings applicable to the oscillator and power supplies are:

3W2052	Oscillator and parts list
3W2062	Oscillator blocking condenser
3W2074	Oscillator chassis
3W2084	Oscillator cover
3W2293	Regulator for high voltage power supply

Although the overall efficiency of the oscillator was less than ten

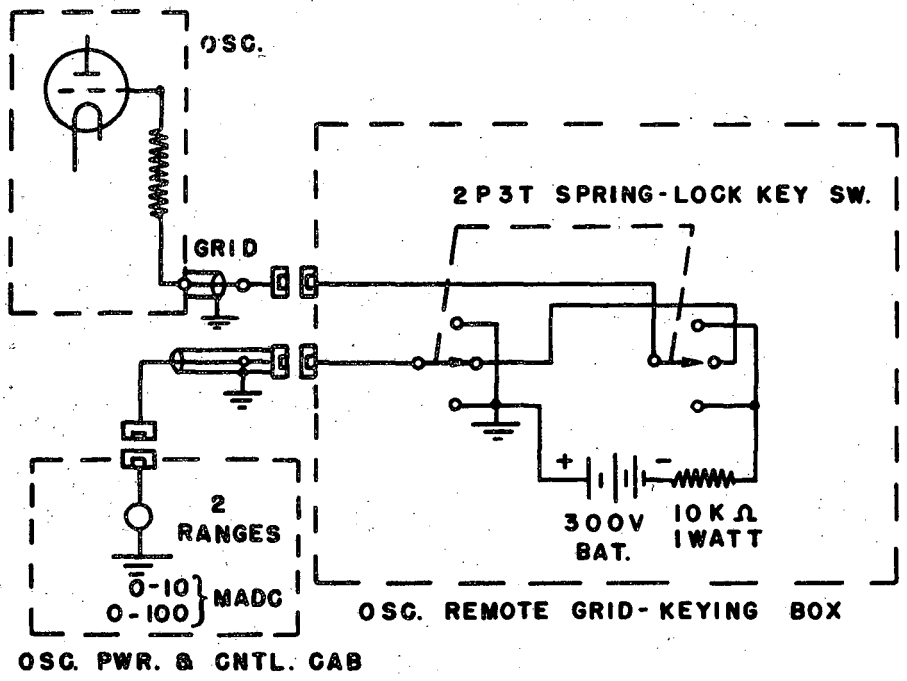

OSCILLATOR GRID KEYING CIRCUIT SCHEMATIC

FIG. V-3

MU 1533

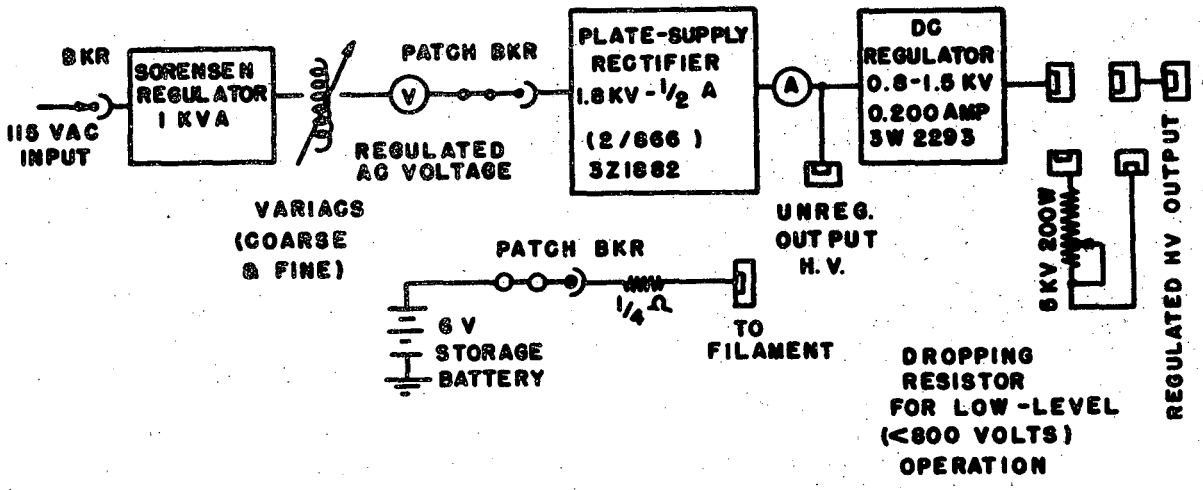

CONTROL CABINET BLOCK DIAGRAM

FIG. V-4

MU 1534

percent, it was entirely satisfactory for the application for which it was intended with respect to frequency and amplitude stability and power output.

VI FIELD MEASURING EQUIPMENT AND TECHNIQUES

A. H-probes

The shunt impedance and Q of the 1/10 scale model were determined from the distribution of the magnetic field in the cavity (see Sections II and X). Therefore it was necessary that the magnetic field be mapped. A special H-probe consisting of a loop at the end of a transmission line was designed to accomplish the field sampling.

The transmission line and loop were made small to keep the perturbation of the fields to be measured as small as practical. How small the loop could be made was determined by the physical considerations involved in making the loop, the sensitivity of the detectors, and a reasonable power rating for the oscillator used to excite the fields in the cavity. With about 20 watts of rf power in the 1/10 scale model cavity, readings could be made on several commercially available detectors if the pick-up loop had an area of about 0.05 square inch.

The transmission line was formed by drawing a length of shielded wire* through copper or stainless steel tubing. The smallest available tubing which proved to be rigid enough was 1/8 in. O.D., with a 0.020 in. wall. The loop was formed on the end of the line by bending the center conductor in a 1/4 in. diameter circle and soldering it to the outer conductor and the end of the tubing. To shield the probe from the electric field in the cavity, the loop was painted with duPont air drying silver No. 4817 in a "balanced" design which was developed by a trial and error procedure (see Fig. VI-1). Fig. VI-2 illustrates the steps of probe construction.

Each probe was carefully checked before it was used. Two conditions

---

* Phonograph pickup-arm cable, Type 1470, Consolidated Wire Co.

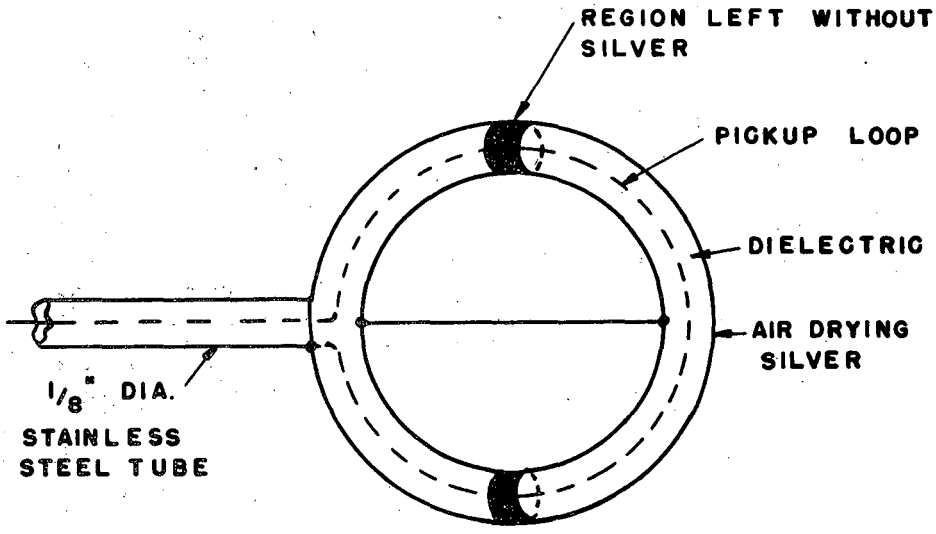

H PROBE SHIELDING DESIGN

FIG. VI-1

MU 1535

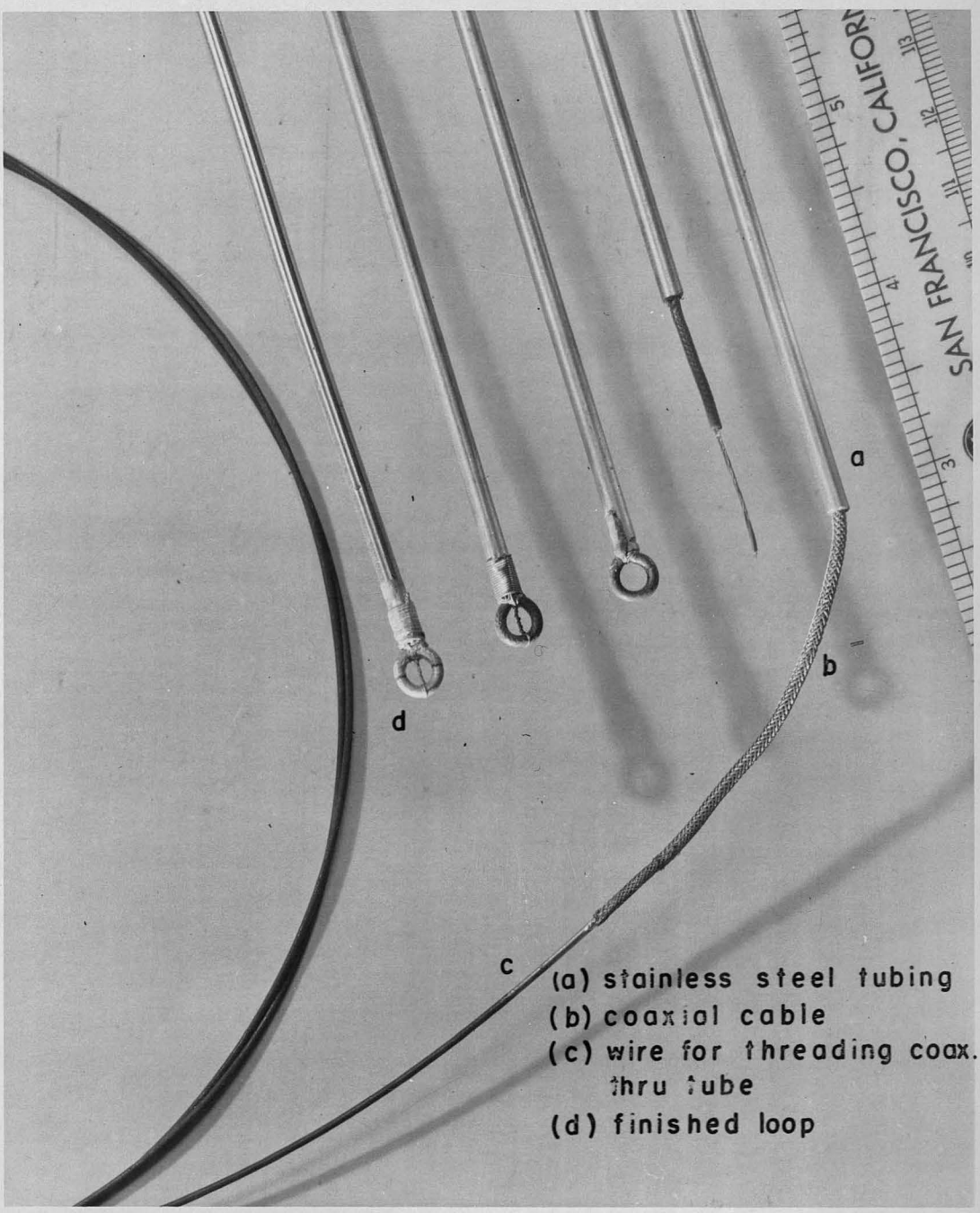

H PROBE CONSTRUCTION DETAIL

FIG. VI-2

OZ 1026

had to be met before a probe was accepted. In a region of the cavity where the H field was zero and the E field large, the probe must give a reading of no more than 0.5 percent of the reading at the point of maximum H field. Also in a region where the E field is changing rapidly with position, the probe had to give the same reading within 5 percent with the maximum area exposed to the H-field that was obtained when the probe was rotated 180°. This second test is referred to as the 0-π test and the ratio of the readings at the maxima the 0-π ratio. Only about 50 percent of the probes made satisfied these two tests.

The outer ends of the probes were fitted with a standard coaxial cable connector type Amphenol 8315P. A small bushing was placed on the 1/8 in. O.D. tubing to make a rigid connection.

B. E probe design

Electric field probes were used to measure the E field distribution of the cylindrical cavity (see Appendix D) as a check on some of the detectors employed. Measurements were made adjacent to the skin of the cavity using a probe of copper tubing with a center conductor of polyethylene insulated wire protruding about 1/4 in. from the end. Satisfactory agreement with theoretical distribution was obtained.

C. Detectors

1. Crystal detectors

The first type of detector used in this investigation was a crystal combined with a bypass condenser of about 0.0001 microfarads as shown in Fig. VI-3. The geometry of the elements of the detector was not critical at the frequencies used.

The signal from the detector was fed into a Hewlett-Packard Vacuum Tube Volt Meter type 410A. To test the linearity of the crystals the H probes were

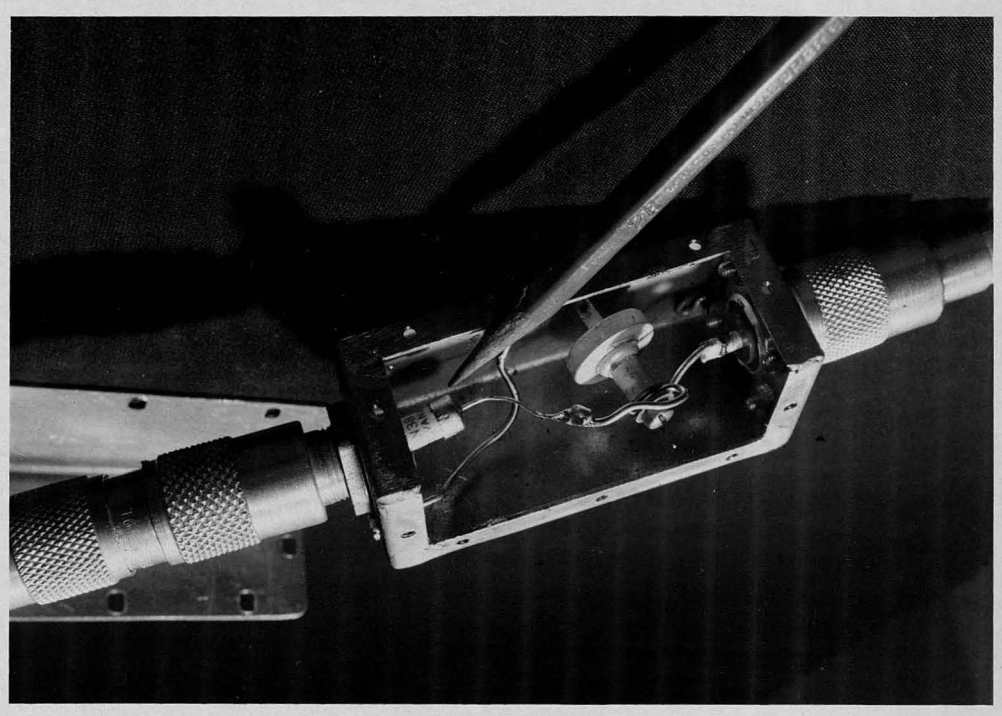

CRYSTAL DETECTOR

FIG. VI-3

rotated in a goniometer and the deviation from the cosine law plotted. This gave corrections to be applied at all signal levels.

Since the crystal detector was not mounted at the loop, consideration had to be given to the proper length of probe for most satisfactory operation. If it is assumed that the crystal rectifier will act as an infinite impedance, after the bypass condenser reaches full charge, it can be shown from transmission line equations that the voltage at the crystal will be:

$$V = \frac{V_i}{\cosh \theta} \qquad \text{(VI-1)}$$

where V_i is the rf voltage induced in the loop.

The electrical length, θ, of a uniform transmission line is:

$$\theta = \alpha \ell + j \frac{2\pi}{\lambda} \ell \qquad \text{(VI-2)}$$

where: α = attenuation in nepers/meter

ℓ = length in meters

λ = wave-length in meters

Substituting (VI-2) in (VI-1) and expanding:

$$V = \frac{V_i}{\cosh (\alpha \ell) \cos (\beta \ell) - j \sinh (\alpha \ell) \sin (\beta \ell)} \qquad \text{(VI-3)}$$

If the probe is cut to any odd quarter wave-length, the cosine term becomes zero and the sine term becomes equal to 1. The voltage in the crystal is then:

$$V = \frac{jV_i}{\sinh (\alpha \ell)} \qquad \text{(VI-4)}$$

If the attenuation of the coaxial line is sufficiently small, α is small enough that:

$$V = \frac{V_i}{\alpha \ell} \qquad \text{(VI-5)}$$

The relationship between Q and α for a resonant, low loss transmission line is to a good approximation

$$\alpha = \frac{\pi}{Q\lambda} \qquad \text{(VI-6)}$$

Substituting

$$V = \frac{4Q\,V_i}{n\pi} \qquad \text{(VI-7)}$$

Thus one would expect to get a voltage increase of about 128 percent of Q. Voltage increases of about a factor of 100 were observed indicating a Q of around 80.

The length of the probes was calculated roughly assuming a dielectric constant of about 2.3 using the expression:

$$\ell = \frac{300}{4\sqrt{2.3}\,f} \qquad \text{(VI-8)}$$

where ℓ is in meters and f in megacycles/sec.

Since (VI-8) does not take into account stray capacities associated with the crystal and crystal holder the probes were usually cut to approximate length and trimmed to a final resonant length with the assistance of a Measurements Corp. Model #59 grid dip oscillator. The trimming could be done by watching the grid dip meter or by observing the rectified voltage as it appeared on the vacuum tube voltmeter.

The performance of the crystal detectors was reasonably consistent. However, certain errors did appear as a result of changes in crystal characteristics. The largest error was probably the one caused by the temperature change of the crystal. A rough check indicated that this error was of the order of 1 percent per degree centigrade change when the signal on the voltmeter was about 10 volts. Attempts were made to control the temperature of the crystal by applying regulated heat from an external source. This did not

completely solve the problem because part of the heat which caused the temperature variation came from the rf losses in the crystal. This variation could not be compensated for quickly with the regulated external heat.

The field plots obtained using crystal detectors and a vacuum tube voltmeter could be repeated to ± 2 percent.

2. Diode detectors

In attempting to find a more accurate and dependable detector than the crystal detector, one type of diode detector was tried. A special fitting was devised to attach one of the standard H probes to the dicde on a Hewlett-Packard 410A Vacuum Tube Voltmeter. A photograph of the assembly is shown in Fig. IX-5. The probes were trimmed with a grid dip oscillator as discussed in the subsection on crystal detectors to take into account any stray capacities associated with the diode and holder.

The diode probe method was used for several weeks as a cavity level monitor and proved to be relatively free from temperature drifts when the voltmeter was used on the 10 volt scale or higher. The instrumental accuracy of the diode probe proved to be between 2 and 3 percent. In spite of the fact diodes gave a slightly greater accuracy than the crystal detectors, they were not used because later methods proved to be even more convenient and dependable.

3. Bolometers

During the course of the cavity measuring program, attention was drawn to the Hewlett-Packard Microwave Power Meter type 430A. This instrument contains a source of 10 kilocycle power, an automatically balancing resistance bridge, and a metering circuit. In operation, a bolometer element, such as a 1/100 ampere Littlefuse, acts as a resistance in one arm of the bridge. The bridge is initially balanced with 10 kilocycle power being dissipated in the Littlefuse. The amount of power dissipated depends on the scale setting of

the meter. When rf power from an external source is dissipated in the Littelfuse the resistance of the Littelfuse increases because of positive temperature coefficient of its element. This unbalance of the bridge automatically reduces the 10 kilocycle power and brings the bridge back into balance. The amount by which the 10 kilocycle power is reduced, which is equivalent to the rf power from the external source, is read on the meter. Since the mass of the wire in the Littlefuse is small and the circuits in the Microwave Power Meter are fast, there is no appreciable lag in meter reading when the rf field is changed.

The initial balance of the instrument, which was done manually, had a narrow range of adjustment. Only 5 percent of the Littlefuses obtained commercially fell within the resistance range required to balance the bridge.

The Microwave Power Meter used did not come supplied with a holder for the bolometer element. One was designed which could be fastened directly to the H probe. The circuit for the bolometer probe is given in Fig. VI-5.* Care had to be taken not to load the 10 kilocycle signal excessively with the bypass condenser. A value of approximately 500 $\mu\mu$f was used.

Since the characteristic impedance of the probe line is of the order of 50 ohms, and the Littlefuse acts as a 200 ohm termination, a quarter wave probe line will provide a voltage gain of:

$$\frac{V}{V_i} = \frac{Z_\ell}{Z_o} = \frac{200}{50} = 4$$

where: V = voltage at the Littlefuse

V_i = voltage induced in the loop

Z_ℓ = impedance of the probe

Z_o = characteristic impedance of the probe line

---

* There is no Fig. VI-4.

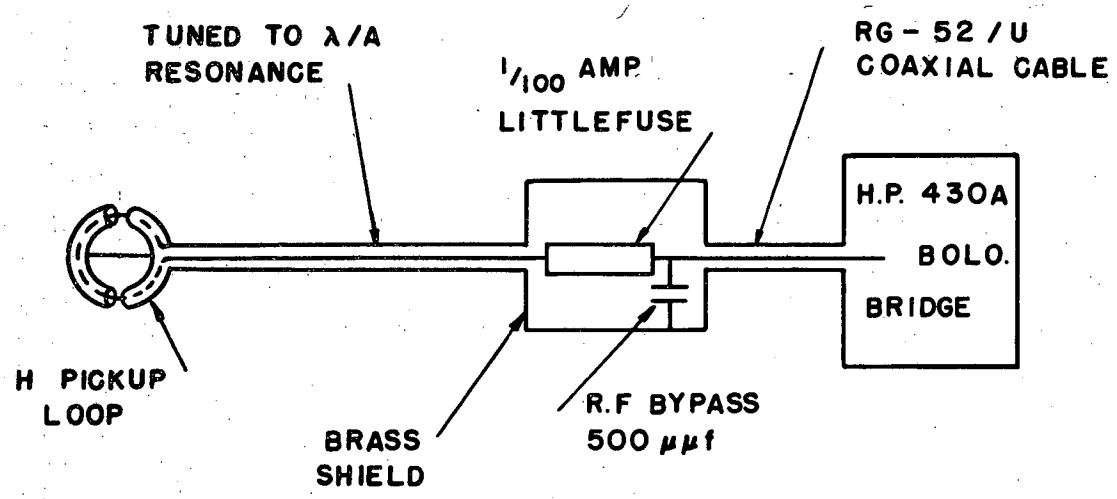

ONE ELEMENT BOLOMETER DETECTOR

FIG. VI-5

MU 1536

Since a voltage gain of 4 means a power gain of 16, there is a definite advantage in using a 1/4 or 3/4 wave length probe. The standing wave ratio of a 50 ohm line terminated with 200 ohms is so low the probes could not be trimmed accurately by observing a dip on the grid dip oscillator. However, using the grid dip oscillator as a signal generator, the probe length can be trimmed by observing the frequency at which the reading on the microwave power meter is a maximum.

The holder described above had its disadvantages, however. Variation in power meter readings caused by temperature changes in the fuse, mechanical shock, and possibly change in the contact resistance in the fuse holder cause instrumentation errors of around 5 percent. For this reason, a special type of bolometer detector which was essentially free of all the disadvantages above was designed. It contained 4 Littlefuses arranged in such a way that the probe was terminated with 50 ohms and the power meter cable terminated with approximately 200 ohms. Type 3AG fuse holders were substituted for the fuse clips previously used to hold the bolometer elements to insure better contact between the fuse and holder. It was necessary to put a 50 ohm resistance in series with the 10 kilocycle power meter lead to bring the bridge to balance. The circuit is shown in Fig. VI-6. Photographs of two different quadruple fuse mounts are shown in Figs. VI-7a and VI-7b.

Rather than mount the quadruple bolometer holder on the end of the probe it was placed in a lead brick enclosure to minimize temperature variations and mechanical shock.

A goniometer check of the probe was made feeding the signal to the four element bolometer. Approximately the same corrections were necessary for the four element bolometer as were needed with the single element bolometer. A typical correction curve is given in Fig. VI-8. The correction table used to

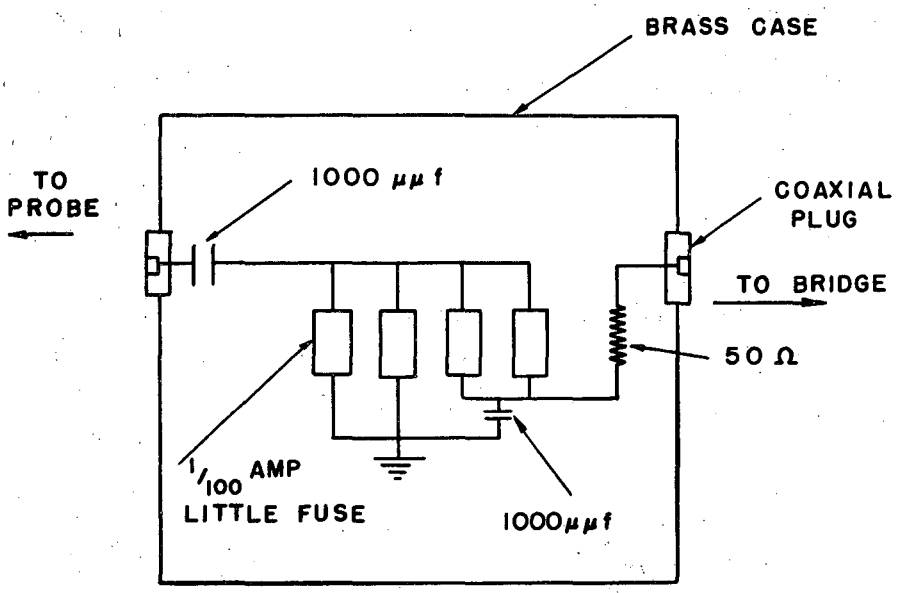

FOUR ELEMENT BOLOMETER DETECTOR SCHEMATIC

FIG. VI-6

MU 1537

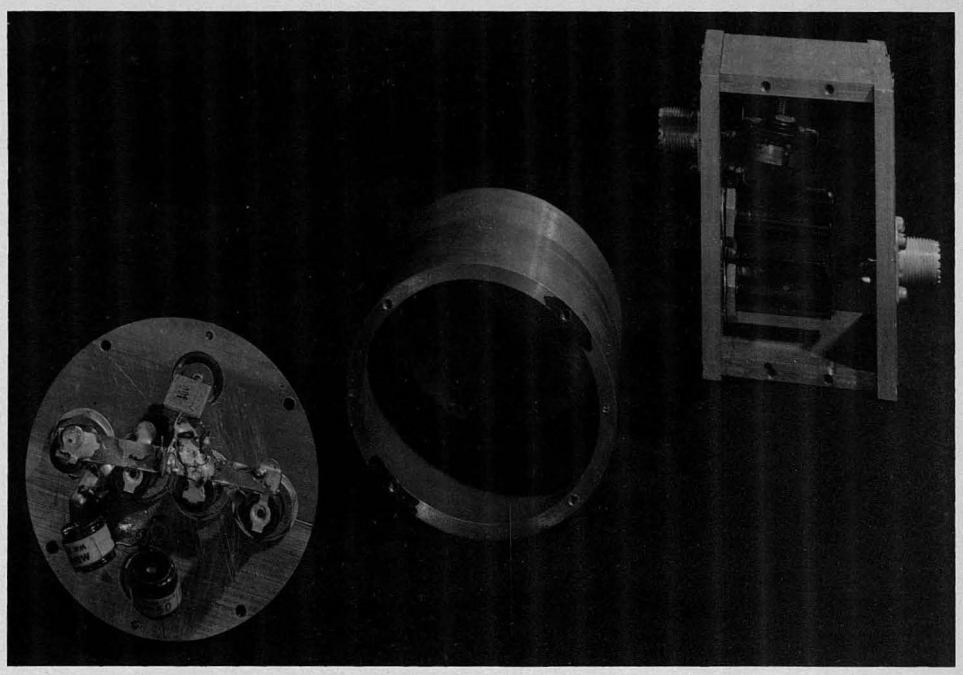

a

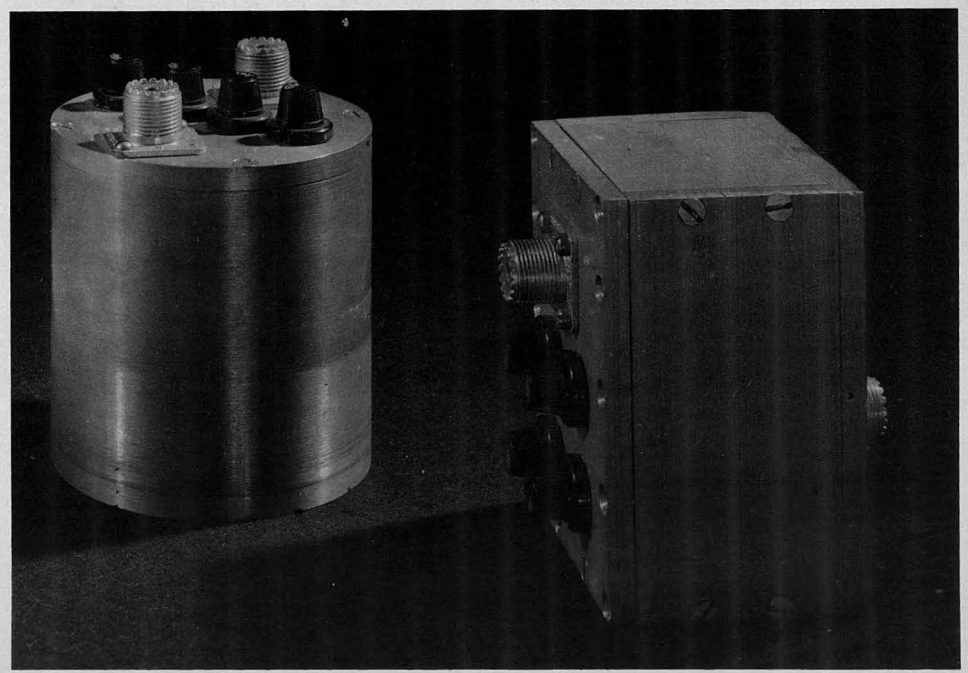

b

FOUR ELEMENT BOLOMETER HOLDERS

FIG. VI-7

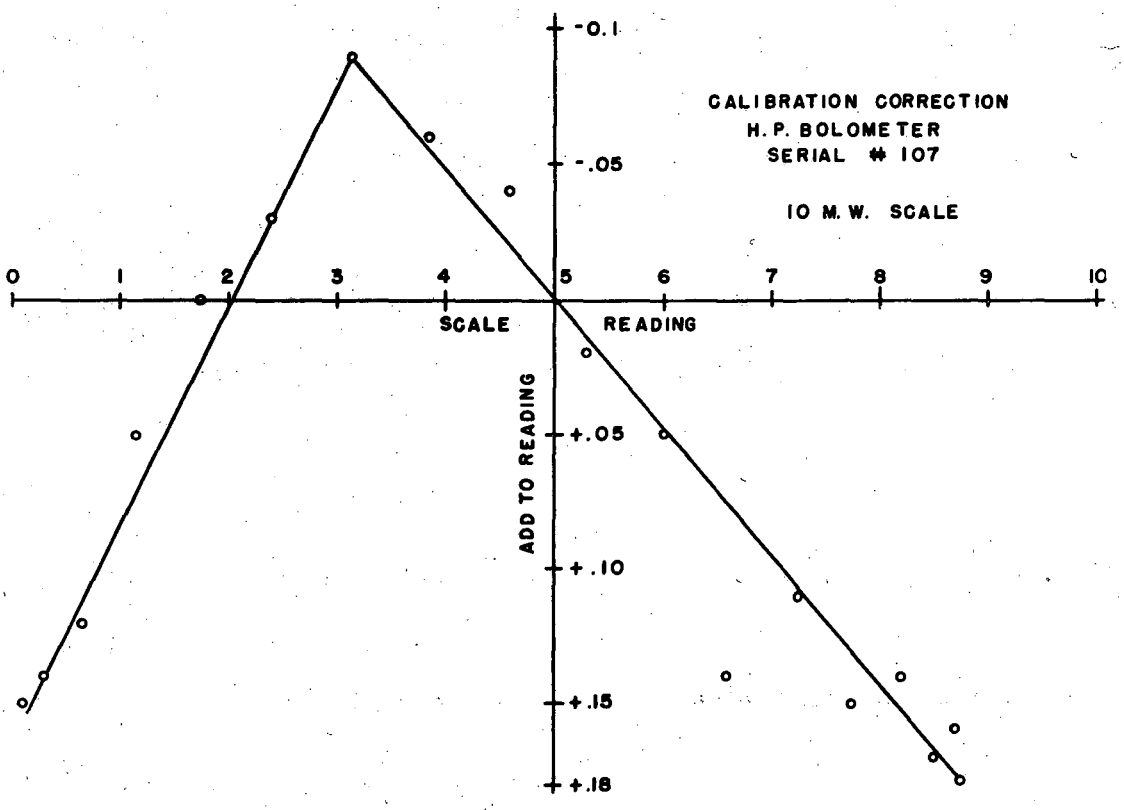

FIG. VI-8

MU 1538

correct all bolometer data taken on the 8 1/2 M is shown in Table VI-1.

At about the same time the quadruple bolometer mount was developed, a more accurate system for monitoring the cavity level was developed (see the following section on Absolute Field Measurements). This system enabled a reproducibility check to be made on the bolometer readings. Before and after each series of field measurements, a reading was taken at an arbitrary check point. If the two values differed by more than 2 percent in power, the series of readings was discarded. Less than 10 percent of the data taken was discarded.

D. Absolute field measurements

It was necessary to determine the absolute magnitude of the fields in the 8 1/2 DT model cavity in order that voltages observed on the drift tube stem bypass condensers could be scaled up to the full scale machine. The condenser voltages are discussed in Section IX and the procedure for scaling the voltage is discussed in Section II.

A small loop was inserted into the cavity on the A plane at the exit end at 195 in. radius (see Fig. X-3). This is a point of high magnetic field and was symmetrical with the point at which the probes were normalized, i.e., at a point where $F_N = 1.0$. The area of the loop was determined by measuring its area on a photograph with a planimeter.

A diode slide back voltmeter similar to the type used to monitor the level of the Berkeley 32 Mev linear accelerator (described in UCRL-236) was used to measure the voltage induced in the loop. In operation, a negative d.c. voltage is applied to the plate of the diode and this voltage is increased (slid-back) until the d.c. conduction current in the diode is zero. The voltage necessary to reduce the current to zero is equal to the peak rf voltage induced in the loop plus a small additional voltage necessary to compensate

Scale Linearity Corrections

For Bolometer #107

(Note: Corrections not to absolute milliwatts)

10 milliwatt scale (Do not use below 0.5 mw)		3 milliwatt scale (Do not use below 0.1 mw)		1 milliwatt scale (Do not use below 0.02 mw)	
For scale reading of	Add	For scale reading of	Add	For scale reading of	Add
0.5 - 1.1	0.00	0.1 - 0.3	0.00	0.02 - 0.07	+0.08
1.1 - 1.7	-0.05	0.3 - 0.5	-0.02	0.07 - 0.17	+0.08
1.7 - 2.35	-0.10	0.5 - 0.7	-0.04	0.17 - 0.27	+0.06
2.35 - 4.5	-0.15	0.7 - 1.15	-0.06	0.27 - 0.52	+0.05
4.5 - 5.5	-0.10	1.15 - 1.52	-0.04	0.52 - 0.71	+0.06
5.5 - 6.6	-0.05	1.52 - 1.9	-0.02	0.71 - 0.90	+0.07
6.6 - 7.6	0.00	1.9 - 2.27	0.00	0.91 - 1.0	+0.08
7.6 - 8.7	+0.05	2.27 - 2.65	+0.02		
8.7 -10.0	+0.10	2.65 - 3.0	+0.04		

Table VI-1

for the thermal energy of the electrons. This small additional voltage is the voltage necessary to reduce the d.c. current to zero when there is no rf voltage induced in the loop, and is approximately one volt in magnitude.

The area of the monitor loop was 0.250 square inches and, at the level that the capacitor voltage measurements were made, about 4 rf volts were induced in the loop. The voltage-current characteristic of the diode is asymptotic to zero current, and this makes it difficult to define the zero current condition to better than about two-tenths of a volt. This limitation introduced an uncertainty in field levels of ten to fifteen percent.

To avoid the limitations inherent in a diode slide-back voltmeter at low levels, a special holder was built containing a 1N63 germanium crystal in place of the diode. The voltage-current characteristic of a germanium crystal has a finite slope at zero current, consequently the balance point of the slide-back voltmeter is sharply defined. The fact that a crystal is not a perfect rectifier makes the slide-back voltage necessary for balance slightly higher than the peak rf voltage; however, this error is small and corrections can be made by graphical methods from the characteristic curves if necessary.

The block diagram of the crystal slide-back voltmeter is shown in Fig. VI-9. The slide-back voltage was measured on a standard 3 inch panel meter, and this voltage was also measured by a Leeds and Northrup type 7655 Potentiometer. The d.c. current through the crystal is balanced to zero on a zero center 10 microampere meter. It was convenient to insert 10,000 ohms in series with the lead to the crystal and read the voltage across this resistance with a type MV-17A Millivac voltmeter. The Millivac voltmeter has scales from 1 millivolt to 1000 volts full scale and is an ideal substitute for a more expensive and less versatile galvanometer in this application. In operation the Millivac is set on the 10 millivolt scale, and therefore reads the d.c. crystal

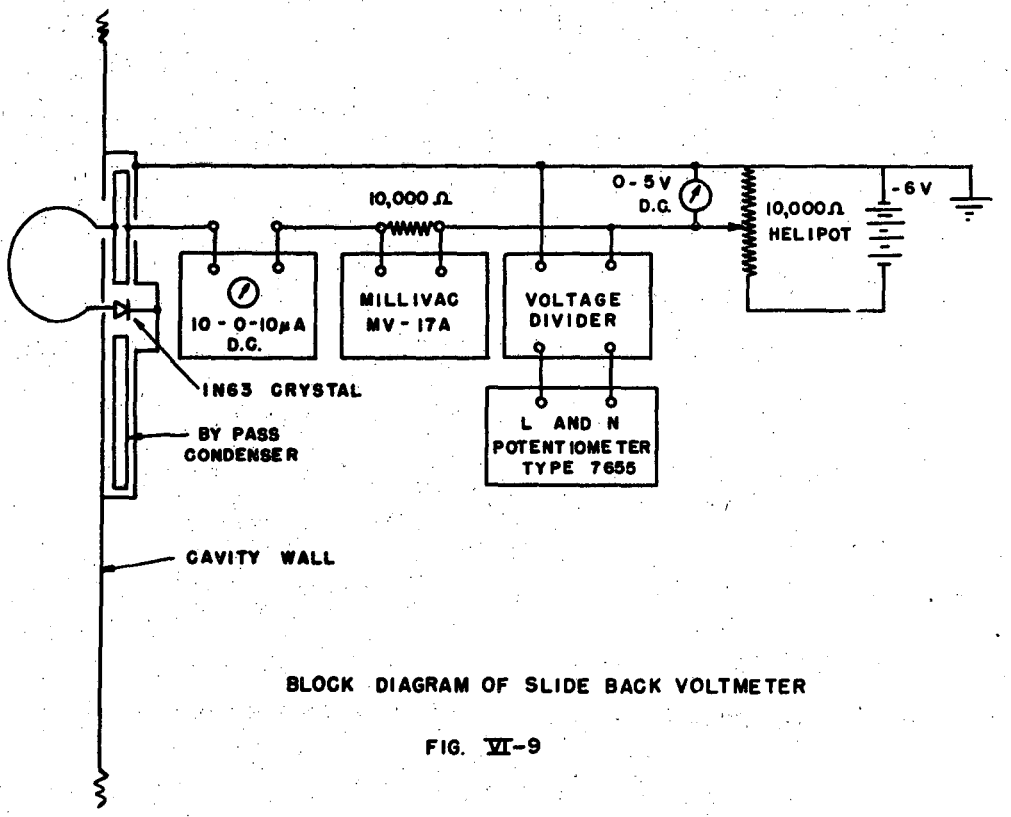

BLOCK DIAGRAM OF SLIDE BACK VOLTMETER

FIG. VI-9

MU 1539

at 1 microampere full scale. It is then possible to adjust the slide-back voltage until the crystal current is less than 0.02 microamperes. A photograph of the slide-back voltmeter and associated equipment is shown in Fig. VI-10. The crystal holder and loop are shown in Fig. VI-11a and VI-11b.

The apparatus for measuring absolute fields was also ideal for monitoring the level of the cavity when making the field measurements described in the preceding section. The reasons why a crystal rectifier was successful in the slide-back voltmeter circuit, and yet was subject to errors when used to measure the voltage induced in an H probe are: (a) there is lower voltage across the crystal, 4 to 5 volts instead of 10 to 20 volts, resulting in reduced rf heating of the crystal; (b) the crystal was operated with the slide-back circuit nulled and therefore it presented a higher impedance to the rf and there was no power dissipated in the crystal due to the rectified current; and (c) there could be no change in crystal characteristics due to mechanical shocks since the crystal holder was mounted rigidly on the cavity. It is believed that field levels in the cavity could be reproduced to an accuracy of 1/10 percent with this system.

E. B-B measurements

The measurement of the various frequency deviations as discussed in Section II can be accomplished by comparing the frequency of the cavity oscillator and the frequency of a stable constant frequency oscillator.

It was found that the TS-175/U Signal Corps Heterodyne Frequency meter was capable of supplying an rf signal which was sufficiently stable. The signal from the TS-175/U frequency meter was attenuated and fed into an APR-4 radio receiver. A small amount of power can be coupled out of the cavity oscillator, and fed into the APR-4 receiver. The output of the receiver will be a sine wave whose frequency is the difference between the two rf frequencies.

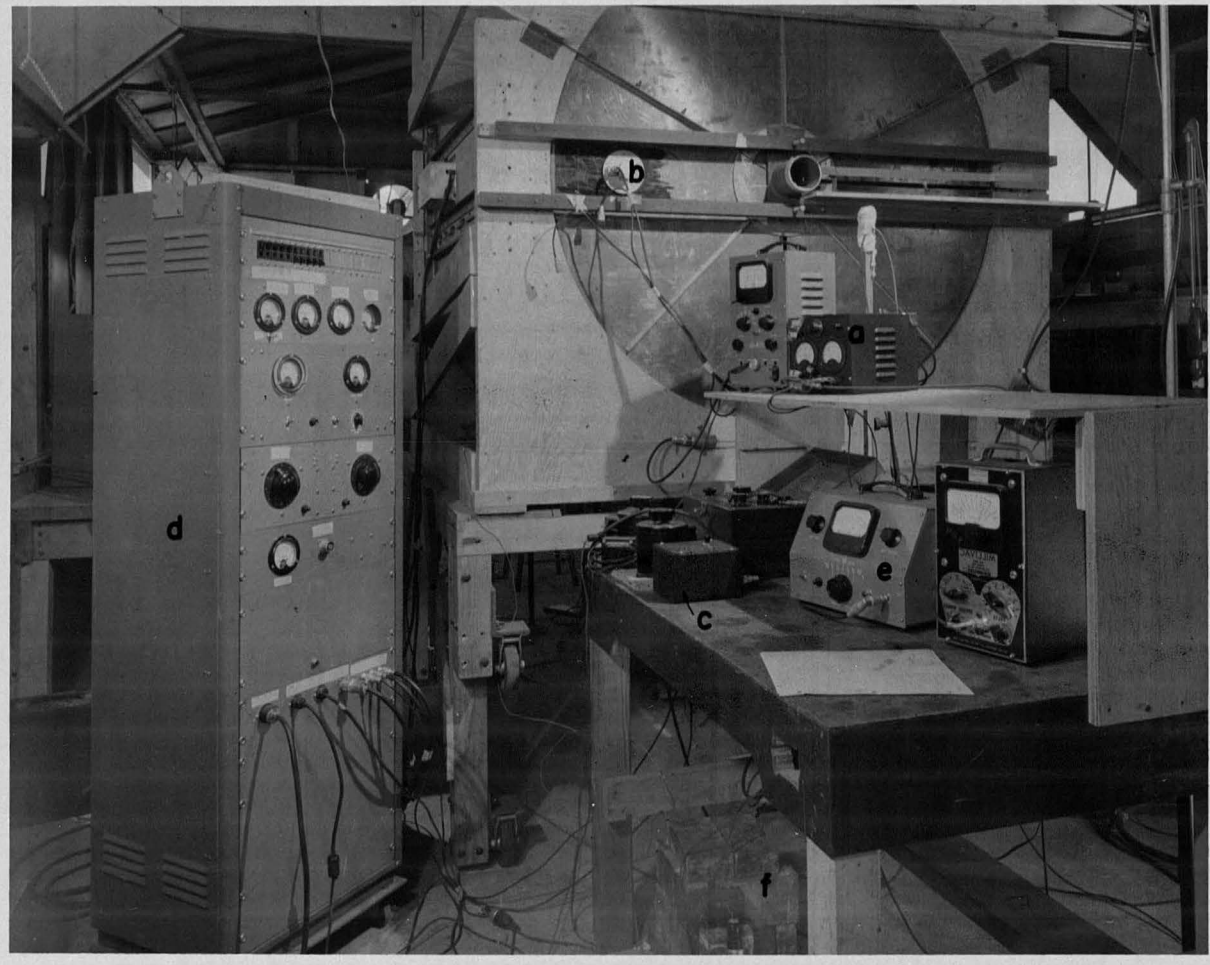

(a) Slide back voltmeter
(b) Slide back voltmeter crystal holder
(c) Osc. remote grid keying box
(d) Osc. power supply
(e) Bolometer bridge
(f) Four element bolometer detector housing

CAVITY CONTROL AND MONITORING EQUIPMENT

FIG. VI-10

OZ 1062

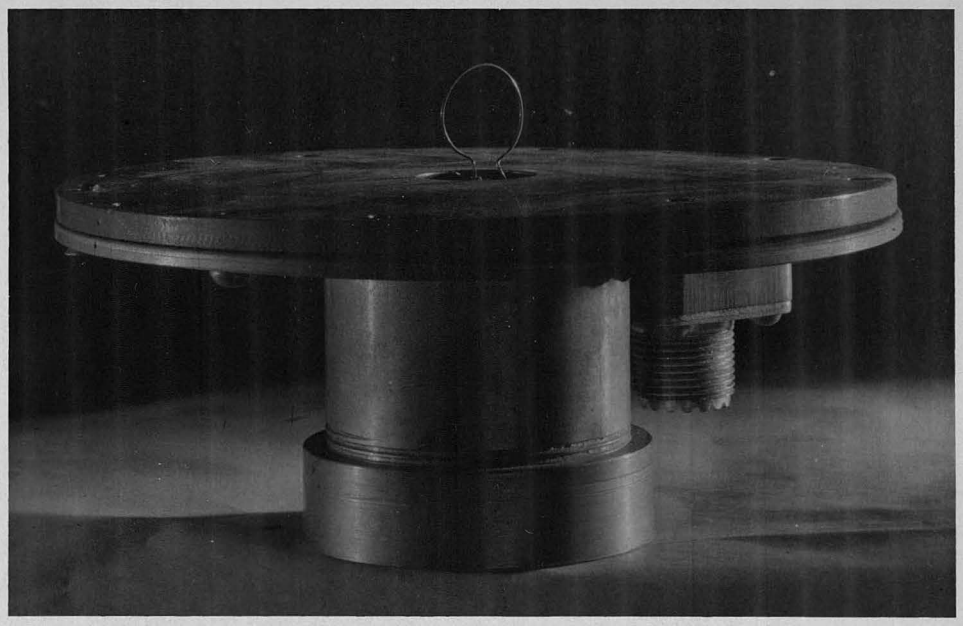

A

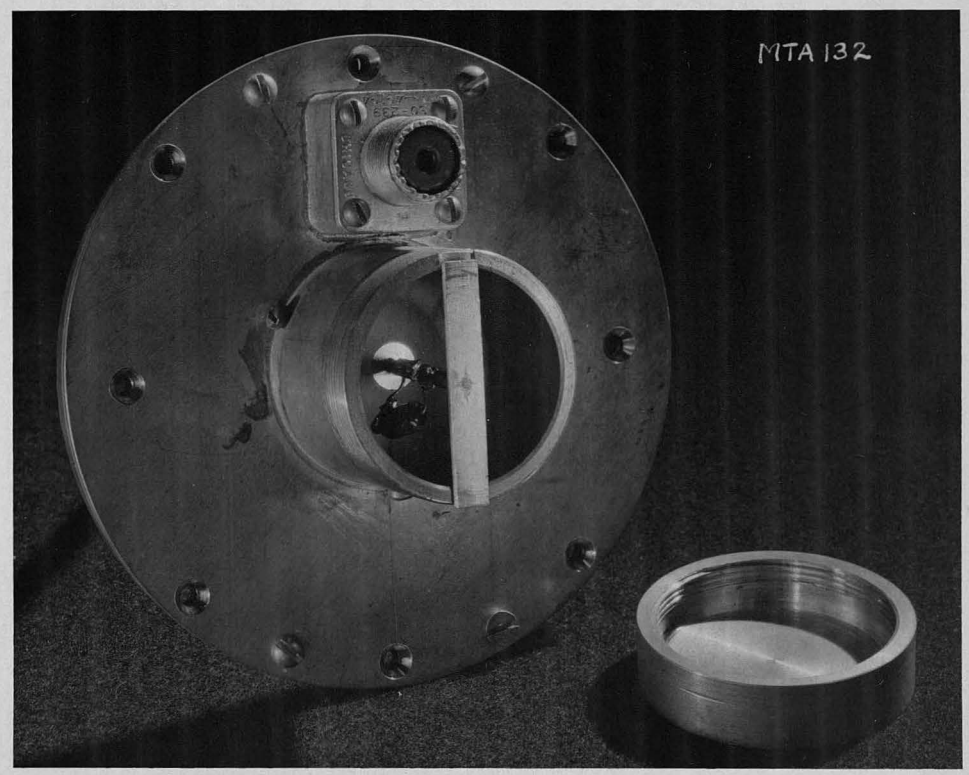

B

SLIDE BACK VOLTMETER CRYSTAL HOLDER AND LOOP

FIG. VI – II

OZ 1071

This difference frequency was fed into the Hewlett-Packard type 500A frequency meter, and relative frequency deviations as the BB is moved to various positions in the cavity are read directly on a meter.

It was found possible to measure frequency deviations to an accuracy of about 50 cycles and total deviations up to 50,000 cycles by the above method. A block diagram of the Frequency Deviation equipment is shown in Fig. VI-12.

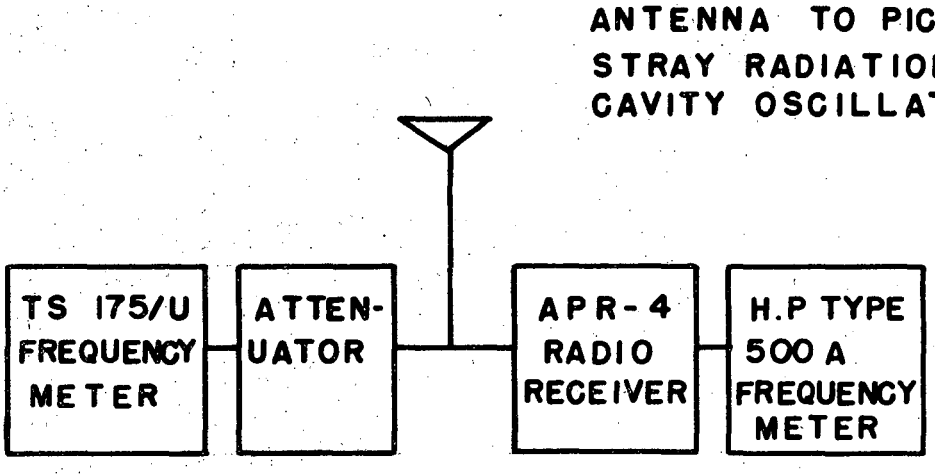

BLOCK DIAGRAM OF EQUIPMENT USED TO MEASURE FREQUENCY DEVIATIONS RESULTING FROM INSERTING BB'S IN A CAVITY.

FIG. VI-12

MU 1540

VII MEASUREMENT OF Q

In order to check the value of Q calculated from the field distributions (Section X), a direct measurement of the Q of the cavity was made. The method used was the following. The cavity was excited with a loosely coupled oscillator. The voltage level in the cavity was then measured with a monitor which did not absorb an appreciable amount of power. Thus for a constant voltage at the oscillator, the level in the cavity could be determined as a function of the frequency of the signal fed into the cavity. Actually, it is sufficient to determine the difference in frequency between the points on either side of the resonance curve where the level of the cavity is 0.707 of the value at the peak resonance. These points are sometimes referred to as the one half power points.

The Q is defined as:

$$Q = \frac{\text{Resonant Frequency}}{(f_1 - f_2)}$$

where f_1 and f_2 are the frequencies at the one half power points. The quantity $(f_1 - f_2)$ is also sometimes called the bandwidth of the cavity.

If results accurate to one or two percent are desired, the problem is one of instrumentation. The resonant frequency of the cavity was measured with sufficient accuracy with a T/S 175 Signal Corps Frequency Meter. However, measuring the bandwidth was more difficult. If the Q of the cavity is between 50,000 and 100,000 and the resonant frequency is 100 megacycles per second, the bandwidth of the cavity will be between 1,000 and 2,000 cycles. Thus it would be necessary to measure the bandwidth to an accuracy of between 10 and 20 cycles per second.

One way to obtain stability and fine control is to design and build a special crystal controlled oscillator. Since it is not usually practical to use crystals cut to a frequency higher than 5 or 10 megacycles per second, it

would be necessary to incorporate frequency multipliers and power amplifiers to obtain sufficient output at the frequencies desired. Rather than do this, it was decided to use a system which included, in as far as possible, commercial type units.

It was found that the Hewlett-Packard VHF oscillator type 608A would operate with a drift of the order of 50 cycles per minute if the line voltage fed into it was stabilized with a type 1000S Sorenson regulator. The control of the frequency of this oscillator was not fine enough to use for a Q measurement. However, provision is made in this oscillator for modulation up to 1 megacycle per second. Thus, if the frequency of the VHF oscillator is modulated and the cavity excited by the sideband, a fine adjustment of the exciting frequency could be made by simply changing the frequency of the modulating oscillator. If the sideband frequency is sufficiently far from the fundamental frequency, there will be no appreciable field in the cavity from excitation by the fundamental. An approximate calculation can be made of how far away the sideband should be. Terman* derives an expression for Q which, to a very good approximation, can be written:

$$Q = \frac{f_{res}}{\Delta f} \frac{\sqrt{(V_{res})^2 - (V_{\Delta f})^2}}{2V_{\Delta f}}$$

where: f_{res} = the resonant frequency of the cavity

Δf = the number of cycles that the oscillator is away from the resonant frequency

V_{res} = the voltage level in the cavity when the oscillator is on the resonant frequency

$V_{\Delta f}$ = the voltage level in the cavity when the oscillator is Δf cycles away from the resonant frequency of the cavity

* F. E. Terman, Radio Engineers Handbooks, McGraw-Hill, 1943, p. 914, Eq. (13)

If a Q of 80,000 is assumed, and the resonant frequency is 120 megacycles per second, the sideband distance necessary to reduce the fields from the fundamental by a factor of 100 is calculated as:

$$80{,}000 = \frac{120 \times 10^6}{\Delta f} \quad \frac{\sqrt{1^2 - (10^{-2})^2}}{2 \times 10^{-2}}$$

Solving for Δf:

$$\Delta f = \frac{120 \times 10^6}{8 \times 10^4 \times 2 \times 10^{-2}} = 75{,}000 \text{ cycles}$$

Therefore, by choosing a modulating frequency higher than 100 kilocycles the fields in the cavity caused by the fundamental can be made essentially zero.

The VHF oscillator was modulated with a Hewlett-Packard 650 A test oscillator. It was found quite stable and had sufficient output to modulate the VHF oscillator 100 percent. The size of the main tuning knob on the 650 A oscillator was increased to give a finer control.

The cavity was coupled to the VHF oscillator by means of a small loop similar to those mentioned in Section VI. Since the output impedance of the oscillator is 50 ohms, the length of the line was not critical.

Because the first sideband will move the same number of cycles that the modulating frequency is shifted, the difference between the frequencies at the half power points is merely the change in the modulating frequency. A second Hewlett-Packard 650A test oscillator was used as a constant reference frequency. This oscillator was set at a frequency very close to that of the modulating oscillator. A mixer circuit was developed (by another group) which put out a sine wave of a frequency equal to the difference between the two 650A test oscillators. This output was fed into a Hewlett-Packard 500 A Frequency Meter which in turn fed a signal into an Esterline Angus 1 ma Recorder. This recorder, then

would show the frequency shift of the modulating oscillator.

The most important reason for showing the frequency shift on a chart is to eliminate the drift in the system from the final result. Although it helped to run all the instruments from Sorenson 110 volt a.c. line voltage regulators, drift did result from instability of the oscillators and the shift in the resonant frequency of the cavity with change in temperature.

The nature of the drifts was such that for short periods of time they were linear. The two half-power points were recorded alternately three successive times. If the drifts were linear, straight lines could be drawn through the one half power points. The separation of the two lines defined the bandwidth of the cavity. It was required that the lines be both straight and parallel. Any non-linearity or instability in any part of the system was evidenced on the chart. Sometimes instabilities in the oscillators could be eliminated by varying the line voltage a small amount causing the VR tubes in the oscillators to operate on a slightly different characteristic. The pen of the Esterline Angus Recorder was carefully balanced to reduce the drag of the paper to its lowest practical value. By holding the frequency of the modulating oscillator at the one half power points for several seconds, the pen had sufficient time to stabilize.

The chart used had a range of 0 - 2,500 cycles per second. Calibration was done in two steps. First a low frequency signal (600 cycles) was fed into the Hewlett-Packard Frequency Meter and the pen set on the proper mark by the zero adjust. Then a higher frequency signal (2,400 cycles) was fed in and the pen set on the proper mark with the calibrate knob on the frequency meter. A check of other frequencies on the chart showed errors caused by non-linearity of the recording system to be less than 20 cycles per second.

It was desirable that the recorder chart be calibrated using a signal from

the mixer. To accomplish this, the input signal to the frequency meter was placed on the vertical plates of an oscilloscope with 1,200 cycles per second on the horizontal plates. Lissajous figures were obtained for 600, 1,200, 1,800, and 2,400 cycles output from the mixer. To be certain that the calibrating oscillator was operating on exactly 1,200 cycles its output was placed on the horizontal plates of a second oscilloscope. On the vertical plates of this oscilloscope was placed the 600 cycle per second signal broadcast by radio station WWV. The calibration oscillator was a Hewlett-Packard 200C; the radio receiver used was a National NC57.

A very important factor in measuring Q precisely is the accurate determination of the level of the cavity at the one half power points with respect to the value at peak resonance. A 1 in. diameter loop was constructed and mounted on a goniometer (see Fig. VII-1). The signal picked up by the loop was fed into an APR-4 receiver. The signal was read by inserting a large 200 microampere signal strength meter in the receiver. If the loop follows the cosine law, the scale of the signal strength meter can be calibrated by rotating the goniometer and observing the meter reading for the various angles. Measurements of the signal reading as a function of the angle of the loop in the field indicated that the receiver signal monitoring circuit was linear within 1 percent if a constant of about 2 percent was subtracted from all readings. This 2 percent was, presumably, noise in the receiver. Although the cosine law of the loop was not verified independently, it would be unlikely that the errors in the cosine law of the loop would be canceled by errors in the signal strength monitoring circuit of the APR-4.

In actual measurement of Q the cosine law of the loop is assumed. With the goniometer set on 45°, the frequency of the modulating oscillator was adjusted to give a maximum signal strength on the APR-4. This reading on the meter is noted. The goniometer is then set on 90° and the frequency of the modulating

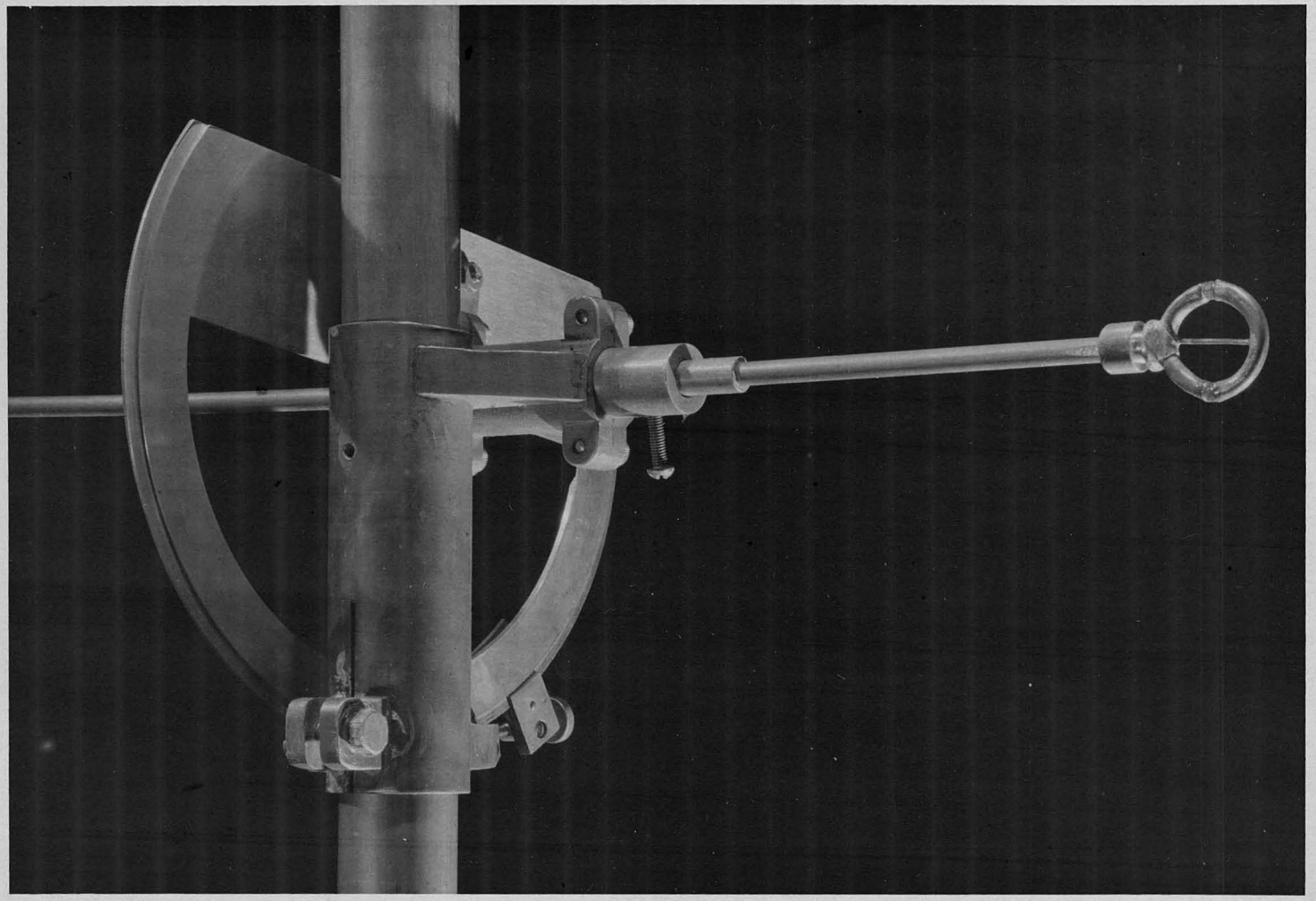

Q MEASUREMENT DETECTOR LOOP AND GONIOMETER

FIG. VII – I

oscillator adjusted to give the same signal strength on the meter as was obtained at the 45° position. This frequency is held long enough to allow the pen on the recorder to stabilize. Then the frequency is adjusted to cause the signal strength to move up through a maximum and back to the same setting previously obtained. This procedure is repeated twice. The goniometer is then returned to 45° and the signal strength maximized to check the drift in the output level of the oscillator. The result is a series of pedestals on the chart which represent the frequencies at the one half power points. A photograph of one of the Q charts is given in Fig. VII-2. Fig. VII-3 shows a block diagram of the Q measuring equipment. A photograph of the instruments is given in Fig. VII-4.

The value of Q measured for the 1/10 scale model cavity was 77,800 ± 2 percent. This gives a Q for the full scale machine Q_M = 246,000 ± 2 percent. The measured Q's are analyzed and compared with those calculated from the field plots in Section XI.

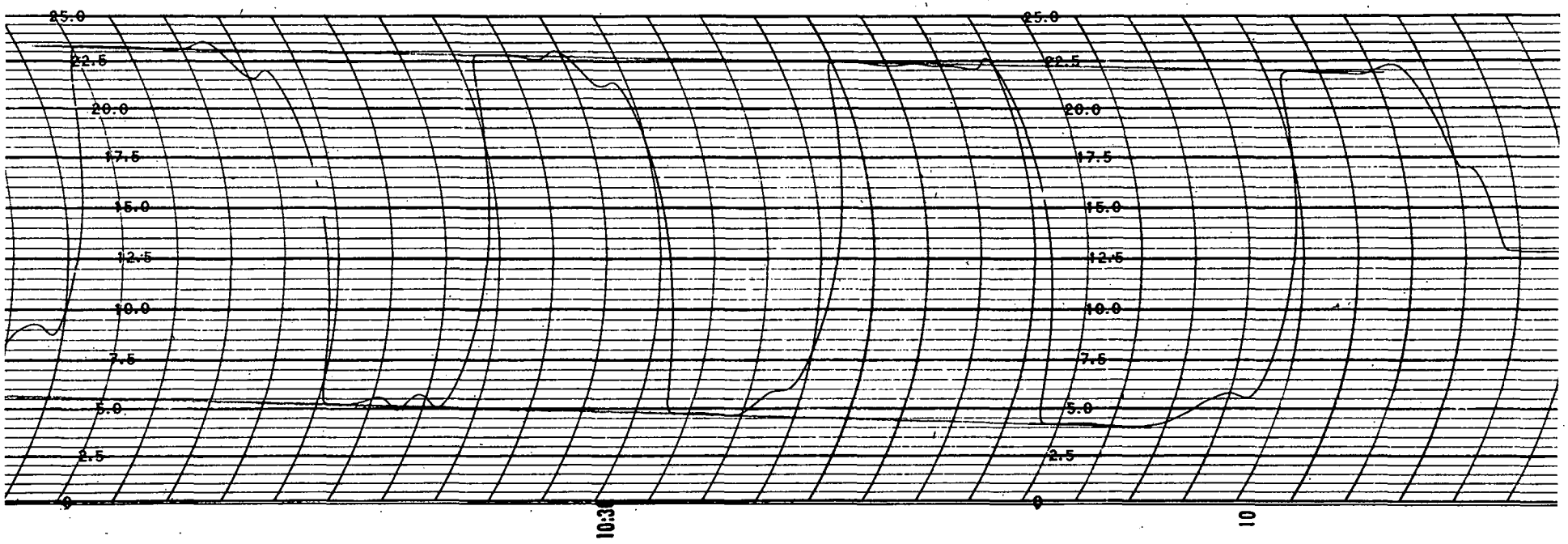

A TYPICAL Q - CHART

FIG. VII-2

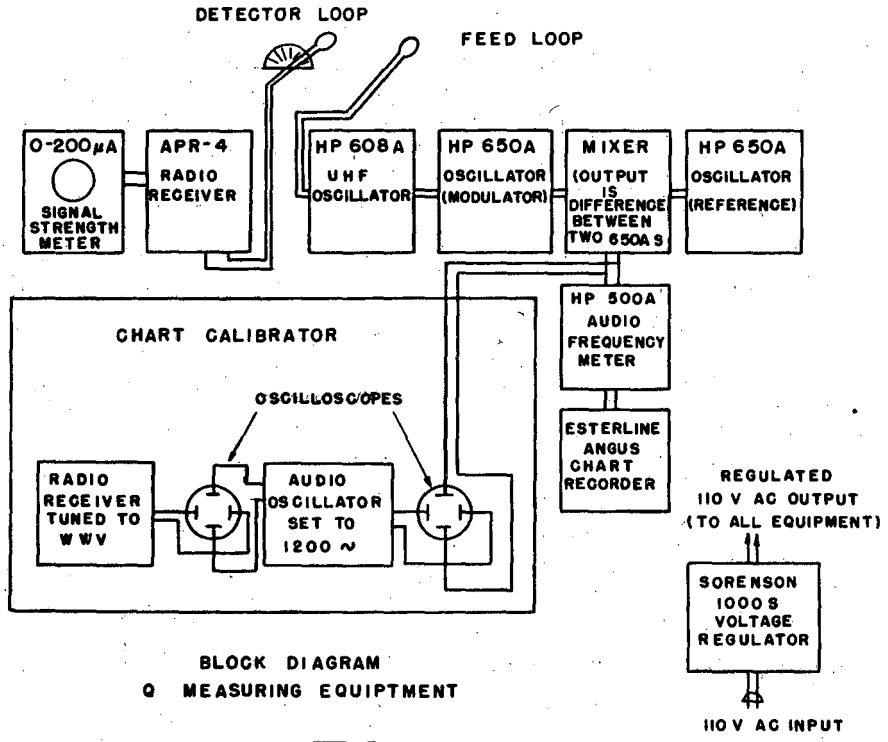

BLOCK DIAGRAM
Q MEASURING EQUIPTMENT

FIG. VII-3

MU 1541

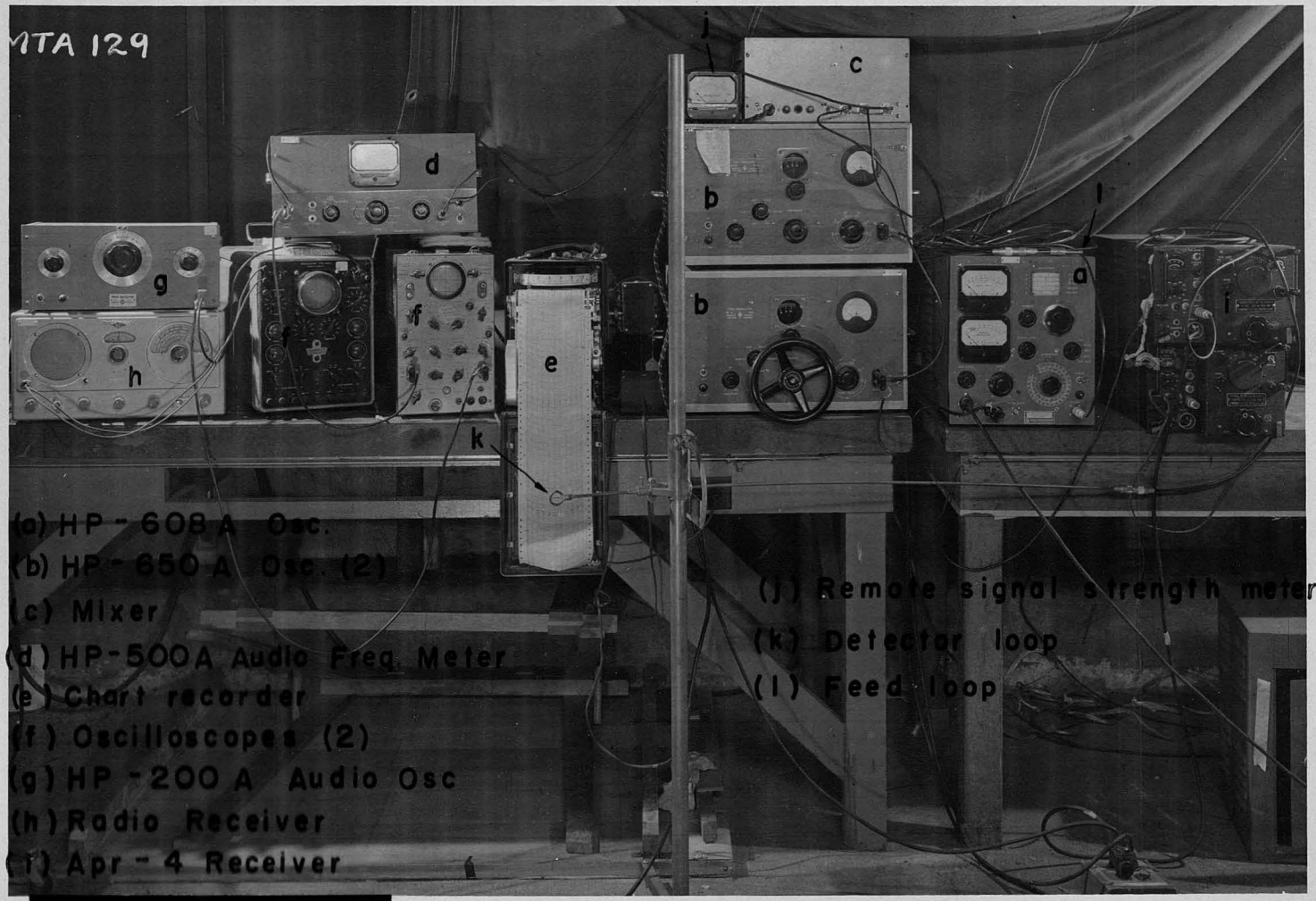

Q MEASURING EQUIPMENT

FIG. VII - 4

VIII $7\frac{1}{2}$ DRIFT TUBE MODEL

The original design of the Mark I was for $7\frac{1}{2}$ drift tubes and the 1/10-scale cavity was constructed on this basis. The measurements program was by no means complete when the design was changed to $8\frac{1}{2}$ drift tubes. The program was continued while the redesign was being completed but the measurements were of a qualitative nature. No information was obtained which was not repeated on the $8\frac{1}{2}$ M in a much more complete manner. For this reason the $7\frac{1}{2}$ M measurements will not be detailed here.

IX DRIFT TUBE STEM INVESTIGATIONS ON 8½ DT MODEL

One of the important investigations made in connection with the model was that of the drift tube stem position. D.C. bias voltages are required on the final machine on some of the stems, hence they cannot be tied directly to the liner skin but must be electrically isolated. (In the full scale machine only part of the DT's will be isolated, but the measurements on the model were made with all the stems isolated.) In order that large rf voltages do not build up on the stems so isolated, it is necessary to include a bypass capacitor at the outer extremity. The problem then arises of minimizing the rf current which must flow through the bypass capacity. This was done by a judicious choice of DT stem positions.

A. Stem position determination

In general, the position chosen must be both mechanically and electrically tolerable. From the mechanical standpoint the best position for the stem is along the transverse center-line of the drift tube as shown in Fig. IX-1a. This has the advantage of simplicity of manufacture and installation and the center of gravity of the system falls naturally along the transverse center-line. The latter is important where such a large mass as that of the combined DT and focussing magnet is concentrated on the end of the slender DT stem. Electrically this position is not tolerable because of the large rf current that would flow through the bypass capacitors.

From the abstract electrical standpoint the best position would be with the axis of the stem coincident with the surface of symmetry dividing the two cells formed by a DT as shown in Fig. IX-1b. This surface is not a plane and does not cut the DT exactly at the transverse center-line because of the asymmetry of adjacent cells. Experiment shows that these surfaces are approximately

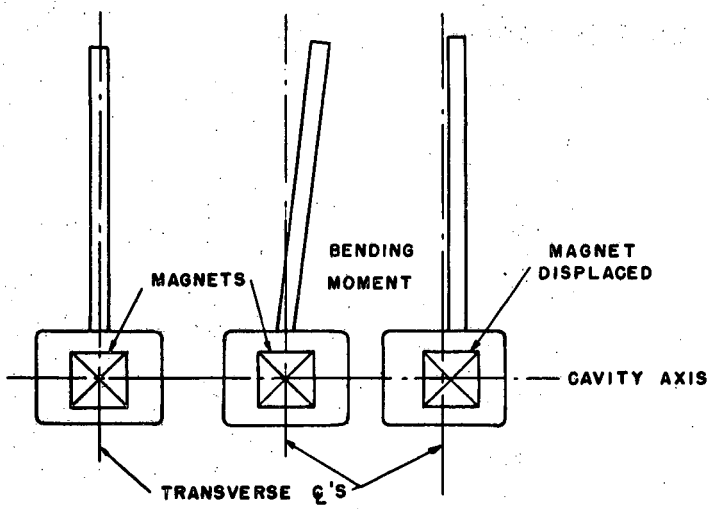

(a) OPTIMUM MECANICAL POSITION

(b) OPTIMUM ELECTRICAL POSITION

(c) ACCEPTABLE COMPROMISE

STEM POSITIONS

FIG. IX - 1

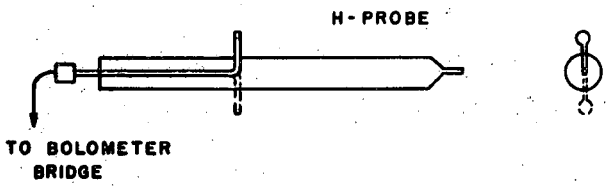

STEM PROBE

FIG. IX - 2

MU 1542

conical in shape with a base angle of the order of a few degrees and with the apex toward the entrance end. Mechanically this position is awkward because (a) the handling of the drift tubes in their installation, which is at best a delicate procedure, would be considerably more difficult, and (b) there is a bending moment to be taken into account in calculating the forces and positioning the stems.

An acceptable compromise was reached, after some investigation, in which the stem is placed perpendicular to the drift tube axis but displaced from the transverse center-line by a critical amount to minimize the rf current. (See Fig. IX-1c.) This requires that the DT magnets be displaced enough to keep the center of mass along the stem center-line. An account of the procedure for the investigation is given below.

The first question which arose in choosing this stem position was that of stem losses. It seemed possible that if the stem was not on the surface of symmetry between half-cells that the differential E-field on opposite sides of the stem would cause greater losses. Such a field would result in a circumferential current around the DT stem which in turn would induce a component of magnetic field longitudinally along the stem. The probe shown in Fig. IX-2 was designed to detect this longitudinal field. The plane of the loop was lined up perpendicular to the stem axis as nearly as possible and the transmission line was run through a hole in the side of the stem and out of cavity where the signal was detected by a bolometer. Quantitative data was not easily obtained because of the fact that the readings were barely detectable, but this was sufficient evidence that the losses due to the circumferential currents were at least an order of magnitude below those due to the longitudinal currents. These tests were carried out on DT-5 at a distance of approximately 120 inches from the liner. It has more recently been noted that the effect might be greater

near the DT where the E-field is greater but it is difficult to conceive of it reaching the magnitude of the longitudinal current.

With the assurance that the losses would not become excessive the remaining problem was to determine the exact offset from the transverse center-line for each DT stem. Due to the interaction between stems it was necessary to have all eight stems scaled, fitted with a detecting device, and positioned in the cavity simultaneously. A stem and detecting assembly is shown in Fig. IX-4. The coupling box (e) was originally designed to house a bolometer detector element but was converted for use with the H.P. 410A voltmeter because the 1/100 ampere Littlefuse detecting elements were too easily burned out by chance movements of the stems. A sketch of the system is shown in Fig. IX-3a. An adaptor to allow the use of standard coaxial connecters and to contain the fields was designed and is shown in Figs. IX-4d and IX-5. The coupling box is grounded to the liner by resting it on the slot edge, and the stem is entirely inside the cavity. This prevents fields from being propagated outside the cavity by the stem. The system is coaxial from the end of the stem to the diode probe, where the voltage between stem and liner wall appears.

The mechanical positioning of the stems was first accomplished simply by resting the tip of the stem in the $2\frac{1}{2}$-inch slot ($\frac{1}{4}$ in. model) cut in the DT's. Later V-grooves were filed in the lower surface of the DT slot at $2\frac{1}{2}$-inch ($\frac{1}{4}$ in. model) intervals on each side of the transverse center-line.

The first step in the investigation was to place all eight of the stem assemblies in the cavity and align them on their respective DT transverse center-lines. As a first approximation seven of the stems were left in this position and the remaining stem was moved by 2.5-inch steps ($\frac{1}{4}$ in. model) on the inner end and the outer end moved until the voltage minimum point was observed. The position of the stem was then plotted for each 25-inch ($\frac{1}{4}$ in.

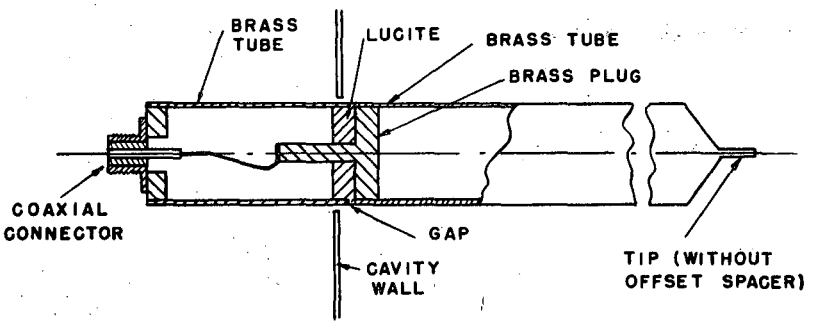

STEM
(a)

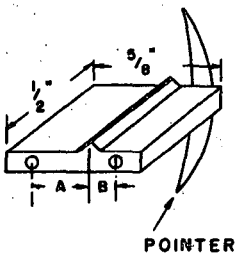

DIM. A	DIM. B
1/4"	1/8"
3/16"	1/16"
0"	0"

OFFSET SPACER
(b)

TEST DT STEM

FIG IX-3

MU 1543

(a) stem
(b) tip with offset spacer
(c) H.P 410A VTVM
(d) diode probe adaptor
(e) stem coupling box

SCALED STEM AND MONITORING EQUIPMENT FOR INVESTIGATING DRIFT TUBE STEM POSITIONS
FIG. IX - 4

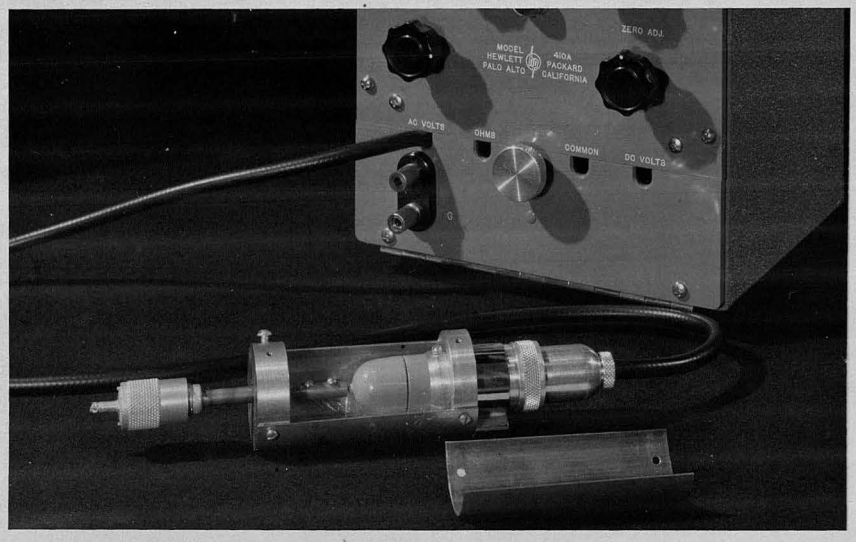

ADAPTOR FROM H.P. DIODE PROBE TO COAXIAL LINE.

FIG. IX-5

OZ 1033

model) increment. Such a graph is shown in Fig. IX-6. The common center of rotation was fortuitous because it provided a direct evaluation of the desired stem position (i.e., perpendicular to DT axis). For the sample stem (#6) the predicted position was 3 3/4 inches (3/8 in. model) toward the exit end from the transverse center-line of the DT. It did not seem practical to use this process on DT-1, 2, and 3 because of the space limitations. The next step was to align each stem at its predicted position and then, starting with #8, adjust the outer end for minimum voltage on its own meter. (Because of interaction between cells the adjacent stem voltages would change radically.) This proved to be a converging process. When all eight of the stem voltages had been reduced to a few tenths of a volt (model) on the H.P. 410A VTVM, the positions of the outer ends of each stem were measured (the inner ends were not moved in this process). The inner end was then moved one-fourth of the way toward the new outer position and the outer end moved three-fourths of that distance toward the inner position. For example, if the inner end was at +2 (0.2 in. model) inches and the final adjusted outer position was +3 inches (0.3 in. model), the new stem position would be with inner and outer ends at 2 $\frac{1}{4}$ (0.225 in. model) inches. This one-fourth ratio was deduced from Fig. IX-6 in which the distance from the inner end of the stem to the center of rotation is roughly one-fourth the length of the stem. Starting from these new positions the process of minimizing voltages individually was repeated and a new set of stem positions determined. This procedure was repeated until it was not necessary to move the outer end of the stems to minimize the voltage after resetting their positions from the previous run.

There were two doubtful points about these results: (a) how much was the 20 inch slot adjacent to the stems affecting the results? (b) what effect would the liner nozzles have on the positions? In order to study these a set of slot

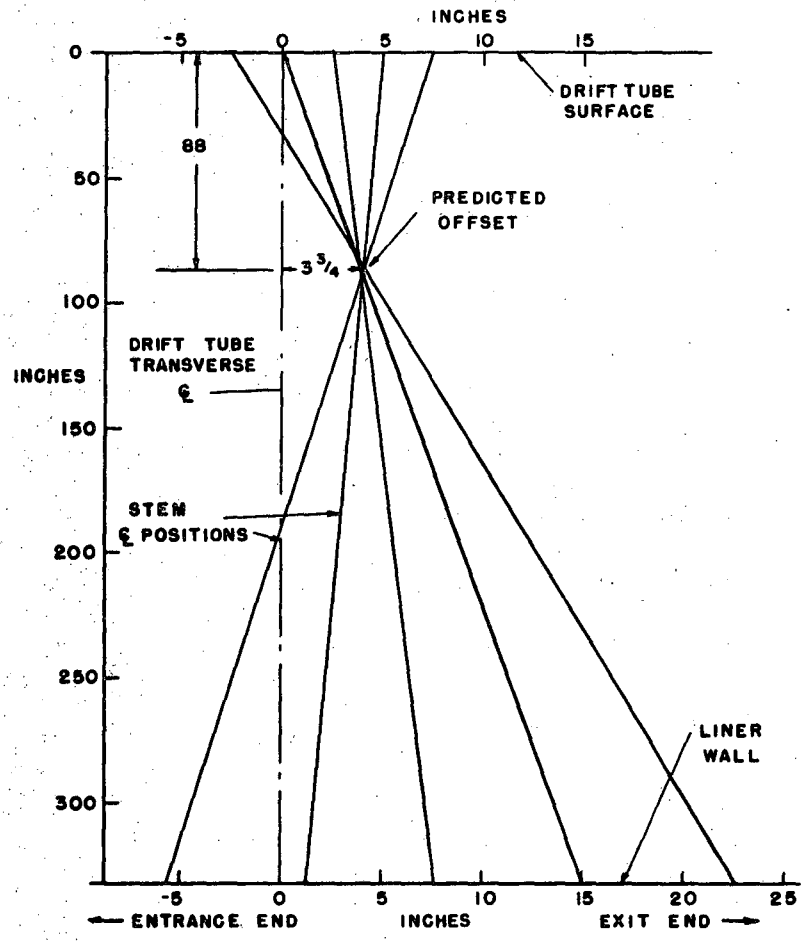

STEM POSITION NOMOGRAPH
FIG. IX-6

MU 1544

closers were made which fitted around the coupling boxes and were taped to the liner. In addition, the liner nozzle for stem #6 was scaled and attached to the cavity. Fig. IX-7 shows the liner with the slot closers and liner nozzle installed. Note that stem #1 and #6 are not in the cavity. Within the accuracy of measurement no change could be observed in the stem position with the slot closed or with the liner nozzle.

There was still a lingering doubt as to the accuracy of the positions determined. It had already been decided to check the stem bypass capacitor currents and this program was extended to include a more elaborate positioning system for the stems to further check the data already obtained.

A set of offset spacers were made as shown in Fig. IX-3b. Dimensions "A" and "B" were made so that with three sizes of spacer the stem could be offset from a given $2\frac{1}{2}$-inch groove on the DT by 0, 5/8, $1\frac{1}{4}$, 1-7/8, or $2\frac{1}{2}$ inches. The pointer was a later addition to aid in determining the correct DT groove to insert the stem. It should be noted that all operations involving the positioning on the DT were tedious and delicate, partly because of the poor visibility and partly from the mechanical instability of the lucite stems (discussed in Part IV), which made frequent readjustments necessary. Following the same procedure as above a new set of stem position measurements was made. Only slight differences were noted. Table I below itemizes the stem offsets considered as final for design purposes. These were considered accurate to $\pm$ 5/8 inch.

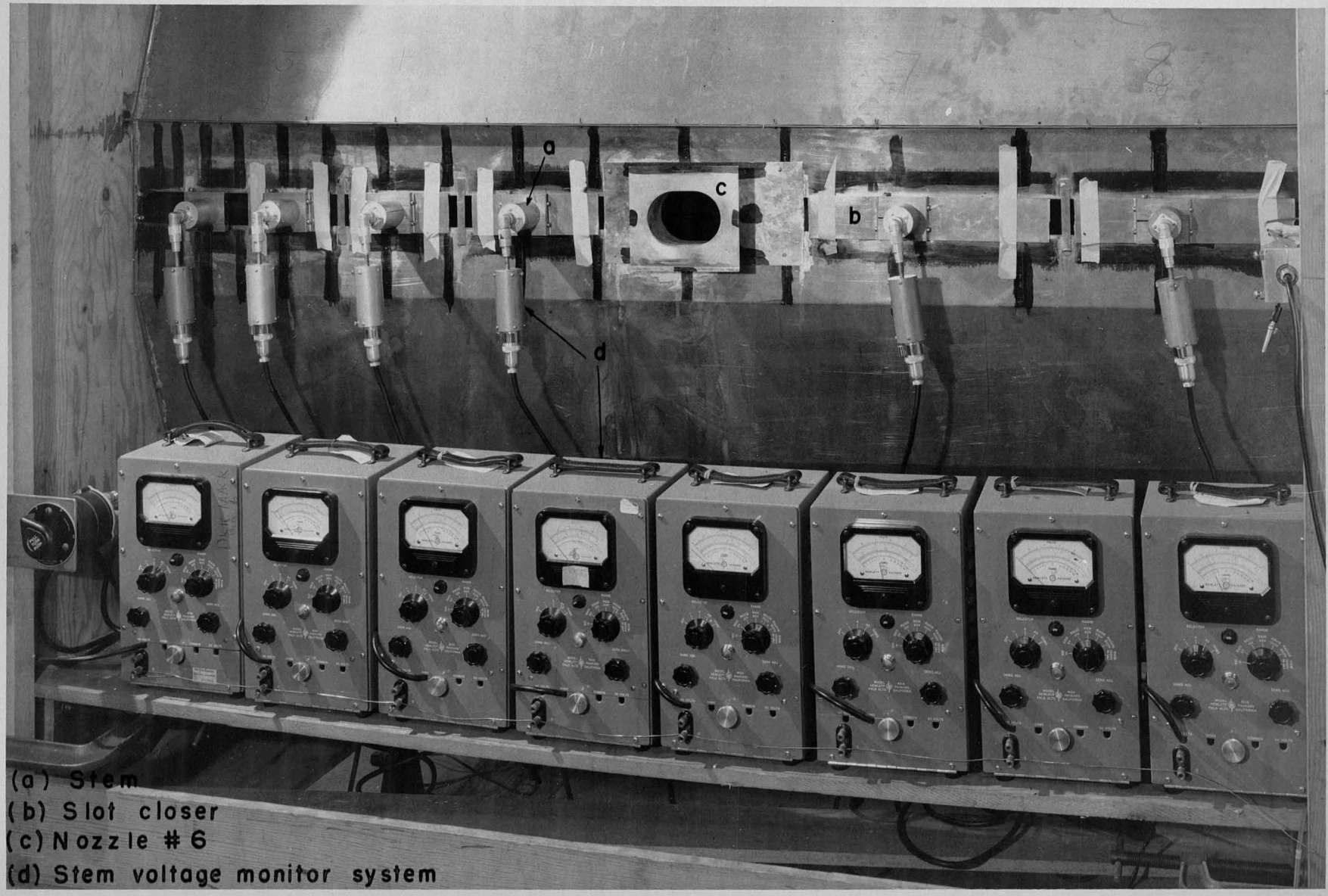

LINER WITH SLOT CLOSERS AND #6 LINER NOZZLE FOR STEM MEASUREMENTS

FIG. IX-7

Stem Offsets

Stem Number	Offset from DT Center-line (inches)
1	+ 1 7/8 ± 5/8
2	+ 3 3/4
3	+ 4 3/8
4	+ 5 5/8
5	+ 5
6	+ 4 11/16
7	+ 2 1/2
8	- 1 1/4

Note: A (+) sign indicates an offset toward the exit end

A (-) sign indicates an offset toward the entrance end

Table IX-1

B. Bypass capacitors and currents

The bypass capacitors were not exact scale models of the final full scale design since this was physically impossible. As a reasonable approximation they were made coaxial with the stem and of a capacity compatible with the full scale design. Two different physical sizes were required. Because of the space limitations near the entrance end numbers 1 and 2 were smaller than those used on the balance of the stems. Fig. IX-8 shows the components in each type and one of the large ones assembled on a stem. The base plate was fastened to the cavity by means of spring finger strips above and below the slot running the full length of the cavity. A mockup of this assembly is shown in Fig. IX-9. The top plate made contact to the stem through a sylphon which was a very tight fit over the stem. The clamping disc was then placed over the top plate and bolted to the lower plate. Several thicknesses of polystyrene spacers were made so that the capacity could be adjusted. The capacity was measured on a GR Type 650A Impedance Bridge. This bridge operates at 1000 cycles/sec., so it was first verified that the same results were obtained on it as on a Boonton Q-meter Type 160-A operating at the frequency of the model. All the capacitors were adjusted to 5000 $\mu\mu$f (500 $\mu\mu$f model). Four slots were cut in the clamping plate to allow the insertion of a specially shaped probe adaptor for diode head on the VTVM. This probe could be inserted in place of the coaxial input to the adaptor boxes. Fig. IX-10 shows detail of probe in position on capacitor. Fig. IX-11 shows an adaptor box with coax input and one with probe input. By measuring in four places the uniformity of the plate spacing is roughly checked, i.e., if the screws on one side are tighter than those on the other side the capacity is not uniformly distributed and the current must be calculated from an average voltage. This is not a serious matter because the direction of adjustment for this measurement is always toward zero voltage and all points on

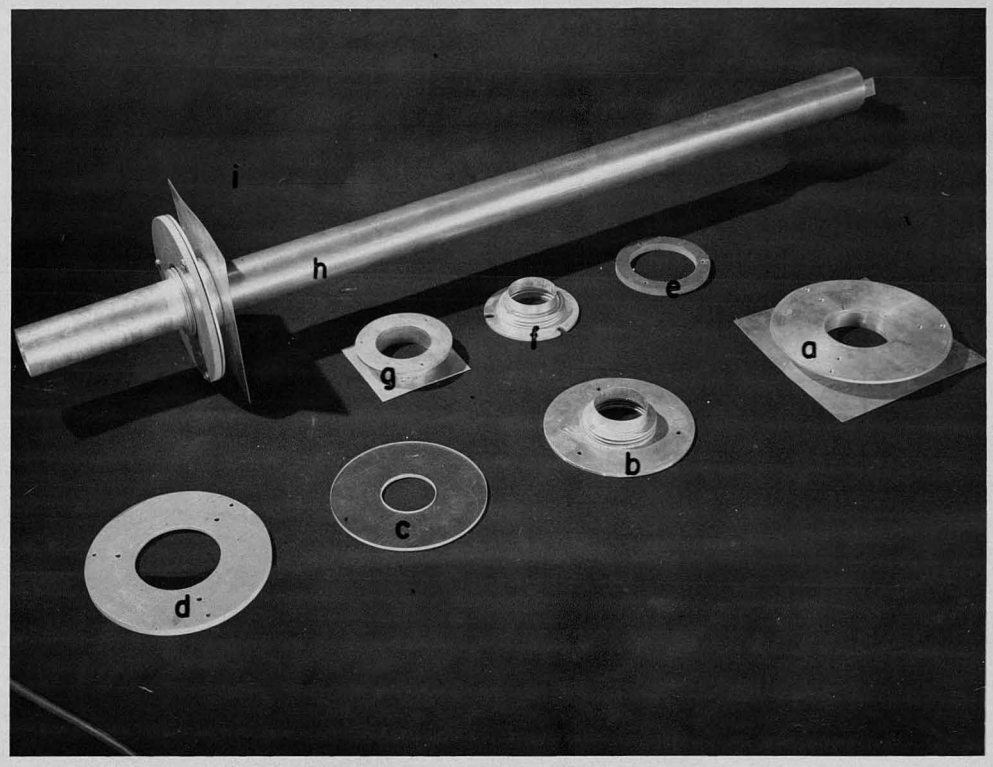

(a)-(d) parts for stem capacitor #'s 3-8

(a) base plate

(b) top plate

(c) polystyrene spacer

(d) bakelite clamping disc

(e), (f) & (g) parts for stem capacitor #'s 1&2

(e) bakelite clamping ring

(f) top plate

(g) base plate

(h) stem

(i) assembled capacitor

FIG. IX-8

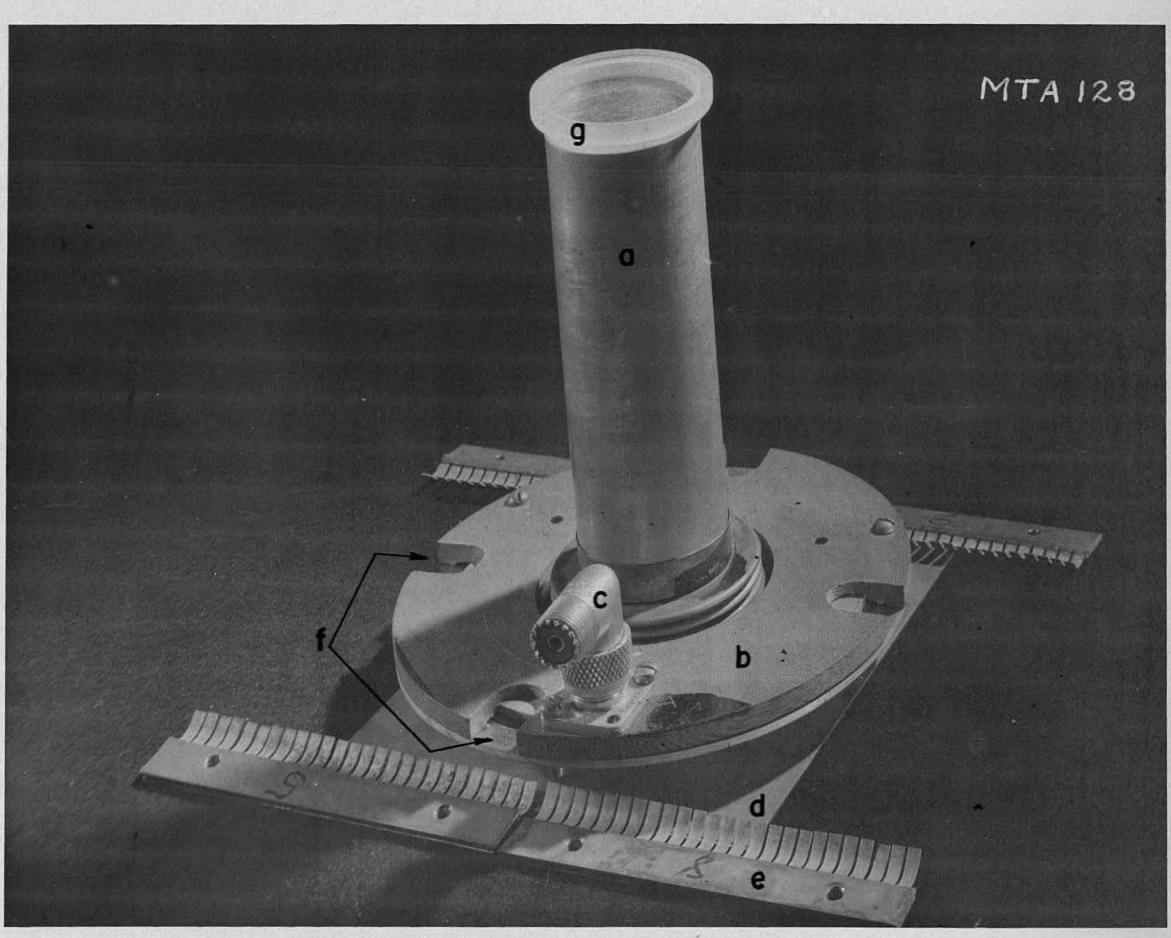

(a) stem
(b) capacitor
(c) output connector
(d) base plate
(e) spring finger clamp
(f) slots for voltage probe
(g) lucite plug with scribed center

MOCKUP OF CAPACITOR SPRING FINGER CLAMPS

FIG. IX-9

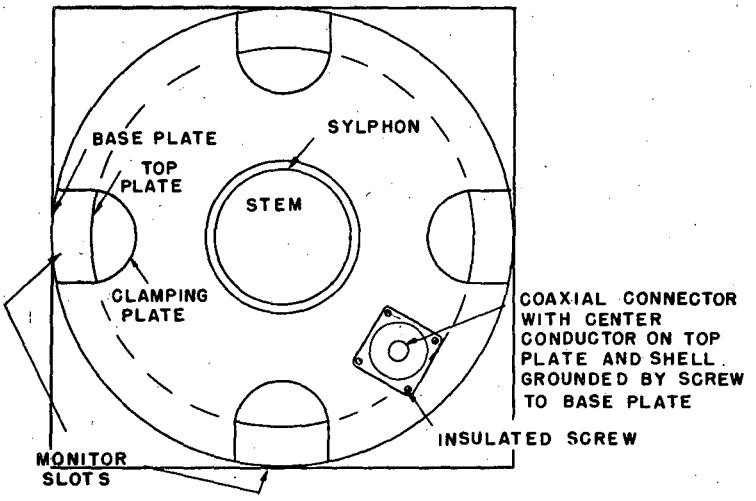

TOP VIEW
(a)

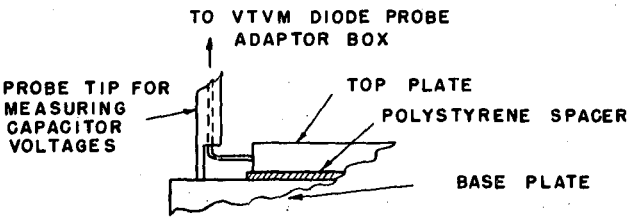

PROBE DETAIL
(b)

LARGE CAPACITOR
FIG. IX - 10

MU 1545

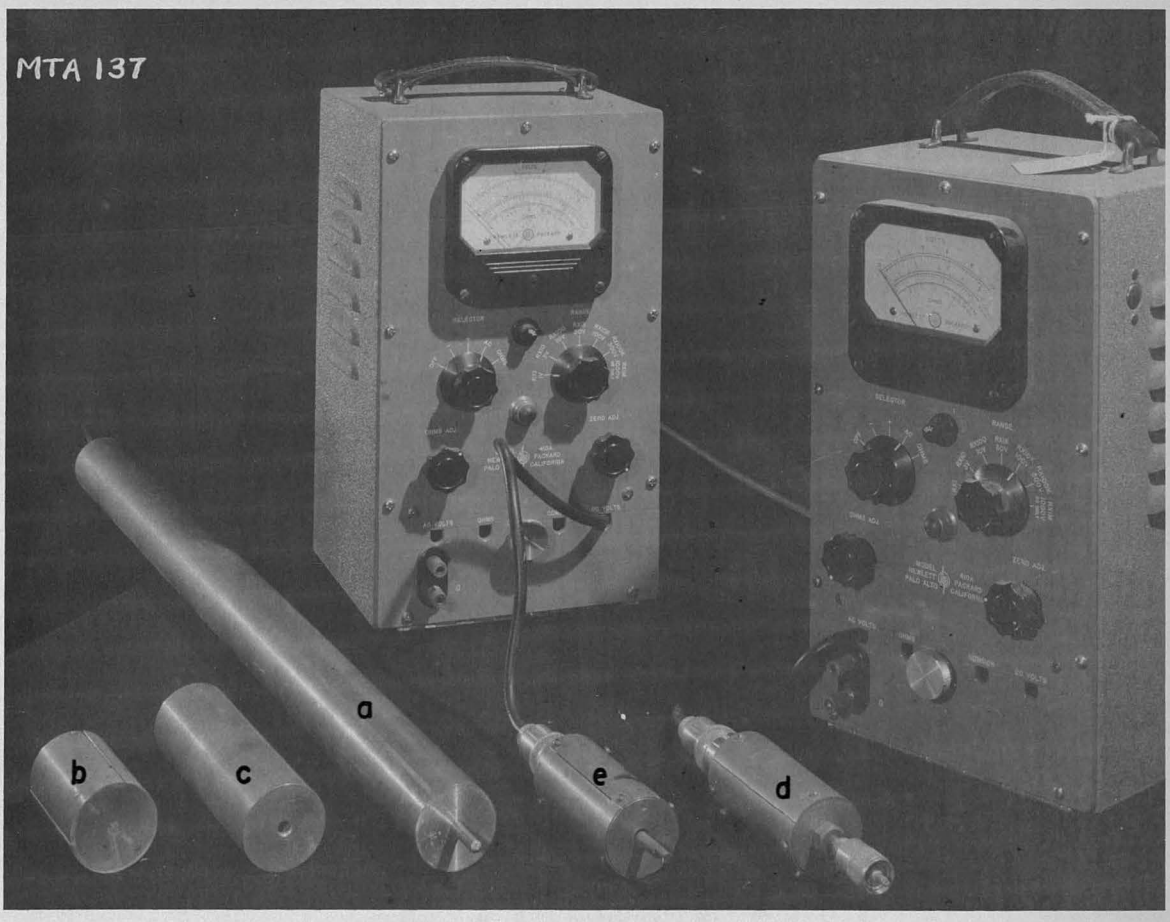

(a) stem

(b) probe coupling box

(c) stem extension

HP 410A VTVM PROBE ADAPTOR BOX WITH

(d) coaxial input

(e) capacitor voltage probe input

FIG. IX-11

the capacitor will reach zero at the same time.

For the measurements with the capacitors it was required that the stems be conducting over their entire length. This required that the coupling box be removed, because of the insulating ring. In its place an eight inch all metal stem extension was clamped. Fig. IX-11 is a photograph of a stem with both types of terminations.

The stems with capacitors were mounted on the cavity in the positions of Table IX-1. It was found necessary to align the DT's with the stems in place and this required the modification of the cathetometer table so that a sight could be taken through a hole punched directly above the DT center-line as described in Part IV. As a further aid for accurate stem positioning a set of lucite plugs with accurately scribed centers were made to fit into the outer ends of the stem extensions. These allowed the position of the outer end of the stem to be accurately measured with the cathetometer.

The stem positions were checked under these new conditions and found to be essentially the same as those given in Table IX-1.

One of the results to be obtained from the capacitor setup was the rf currents which could be expected to flow in them. Table IX-2 is a sample set of data taken on the capacitors.* These measurements were made with an accurately calibrated H.P. 410A VTVM with the probe adaptor of Fig. IX-11e. From this data, and the impedance of the capacitors, the currents were calculated for the average voltage and the maximum voltage of each stem.

As a final check on the accuracy and reproducibility of the measurements the liner nozzles were scaled, and when the system was converted to the metal stems these were installed with the coaxial bypass capacitors mounted on them

---

* A design change increased the capacitance from 5000 $\mu\mu$f to 18000 $\mu\mu$f after the measurements were started. It was impractical to obtain that high a capacity (1800 $\mu\mu$f on the model) so results were scaled.

Sample Set of Capacitor Voltages and Currents

(Values are full scale for Mark I)

Drift tube number	Quadrant voltages (For 5000 μμf)				Voltage (For 5000 μμf)		Voltage (For 18000 μμf)		Current (18000 μμf)	
	0°	90°	180°	360°	Av.	Max.	Av.	Max.	Av.	Max.
1	400	360	280	380	360	400	100	111	137	152
2	220	60	40	200	130	220	36	61	49	84
3	400	320	460	460	410	460	114	128	156	175
4	320	400	260	220	300	400	83	111	114	152
5	400	480	380	280	380	480	106	133	145	182
6	420	340	580	640	500	640	139	178	190	244
7	200	260	300	240	250	300	70	83	96	114
8	380	380	420	440	400	440	111	122	152	167

Where $X_c = \frac{1}{2\pi fc} = 0.729\ \Omega$

$f = 12.1 \times 10^6$ cycles

$c = 18000 \times 10^{-12}$ farads

$I = \frac{V_c}{X_c} = 1.37\ V_c$

$\frac{V_{18000}}{V_{5000}} = \frac{5000}{18000} = 0.278$

Table IX-2

by means of spring finger in a manner similar to that used on the initial measurements. In no case did the voltages measured exceed 170 volts (scaled to 18000 $\mu\mu$f) which corresponds to 233 amperes.

A second investigation was concerned with the variation of voltage with capacity. Theory predicts that the current will be constant for a given geometry regardless of the value of the bypass capacity. Fig. IX-12 shows the experimental results and also the theoretical curve, plotted from the relation:

$$V_c = I_c X_c = \frac{I_c}{2\pi fc} = \frac{K}{c} = \frac{3.678 \times 10^{-6}}{c}$$

assuming the c = 5000 $\mu\mu$f point to be correct. The two curves agree within the accuracy of measurement and the theoretical point for 18000 $\mu\mu$f is used hereafter for calculations involving the actual capacity to be used in the machine. Since all measurements were made at the 5000 $\mu\mu$f point the scaling factor for converting capacitor voltages to the 18000 $\mu\mu$f base is:

$$\text{Scaling factor} = \frac{V_{18000}}{V_{5000}} = \frac{5}{18} = 0.278$$

C. Drift tube perturbations

A logical adjunct to the measurements made above with the capacitors was the investigation of the effect on the bypass capacitor currents when a drift tube and stem were moved axially. This would be valuable information in the event that the conditions for acceleration of the ions were not met or could be improved by readjustment of the gaps.

This information was obtained by moving the DT system by small increments toward both the entrance and exit ends. This increment was measured with the cathetometer and the capacitor and stem moved exactly the same increment to retain the relative geometry of the system. The voltages were then read on the perturbed drift tube and the adjacent drift tubes. These increments were

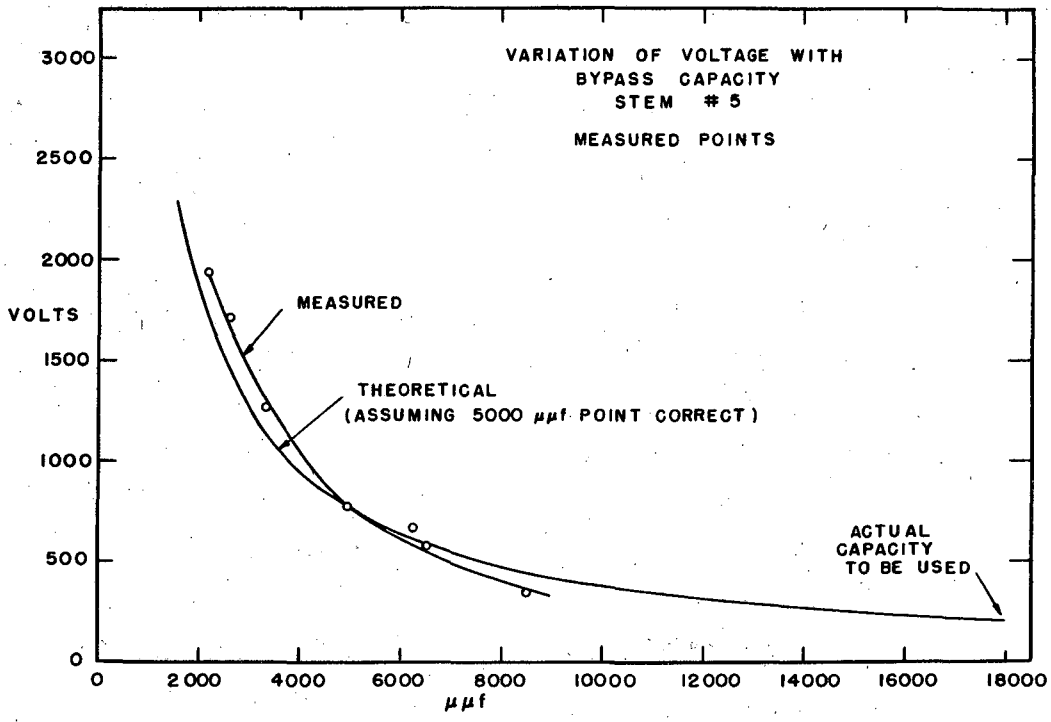

FIG. IX-12

MU 1546

plotted to obtain the slopes of the perturbation curves which fortuitously turned out to be straight lines. Fig. IX-13 shows two sets of data for DT #5 plotted on the same coordinates. The two adjacent drift tubes were also plotted to indicate the trend of interactive effects. It was noted that the effect on the second drift tube away was very small. The important information obtained from these graphs is the average slope. A horizontal displacement indicates that the drift tube was slightly out of position for that run. Note that if the drift tube stem is in its correct position the apex of the cone formed by the perturbation curves will fall at the zero perturbation point. The two sets of data shown were taken on different days, which indicates a reasonable degree of reproducibility. Table IX-3A tabulates the results obtained for other drift tubes. All were measured in the same manner as number 5 except number 1 which was extrapolated from the curve of Fig. IX-14, which is a plot of the average slopes of the perturbation curves for all the drift tubes. Number 6 presents the only anomaly, and since it represents the average of two sets of nearly identical data, it is not obvious why it does not fall on the curve.

A second set of drift tube perturbation data was taken after the metal stems were installed but the results logically belong in this section. The conditions of measurement are more completely outlined in later sections but roughly it was simply a measurement of the slope of a perturbation curve similar to the one detailed above, the only difference being that the drift tube stem was restrained at its out end so that in moving the drift tube the stem was forced to bend. This information was important in designing the focussing magnets as they have axial forces associated with them which cause this type of motion.

It was difficult to create these perturbations synthetically without affecting the cavity in other ways. It was considered sufficient to move

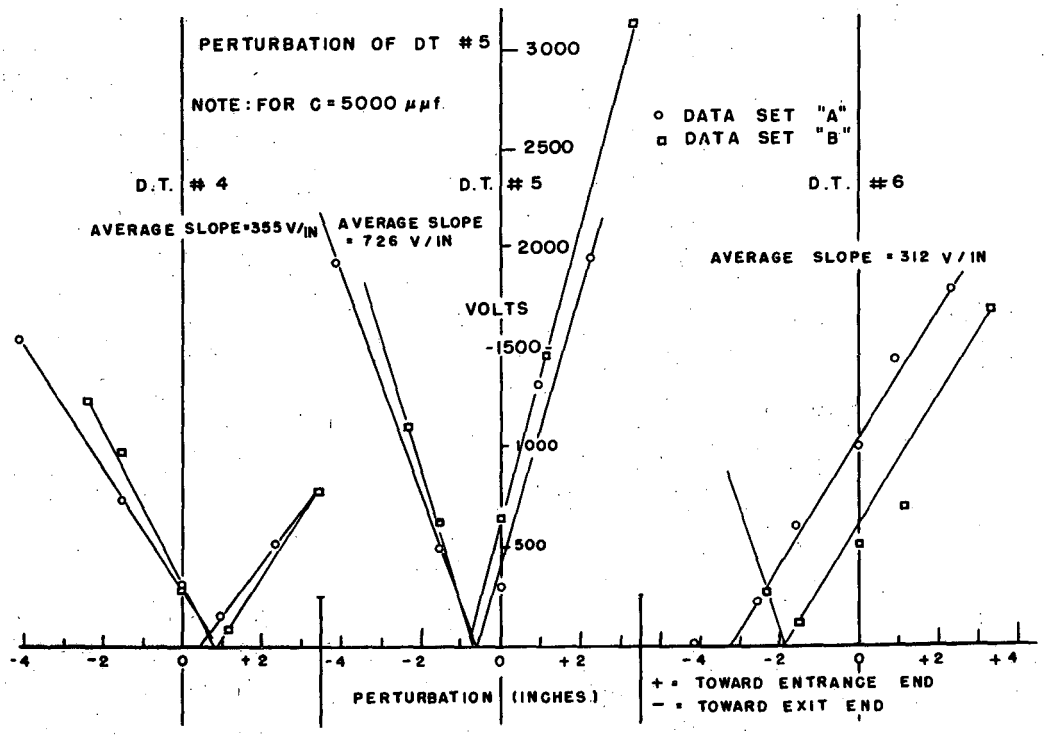

FIG. IX - 13

MU 1547

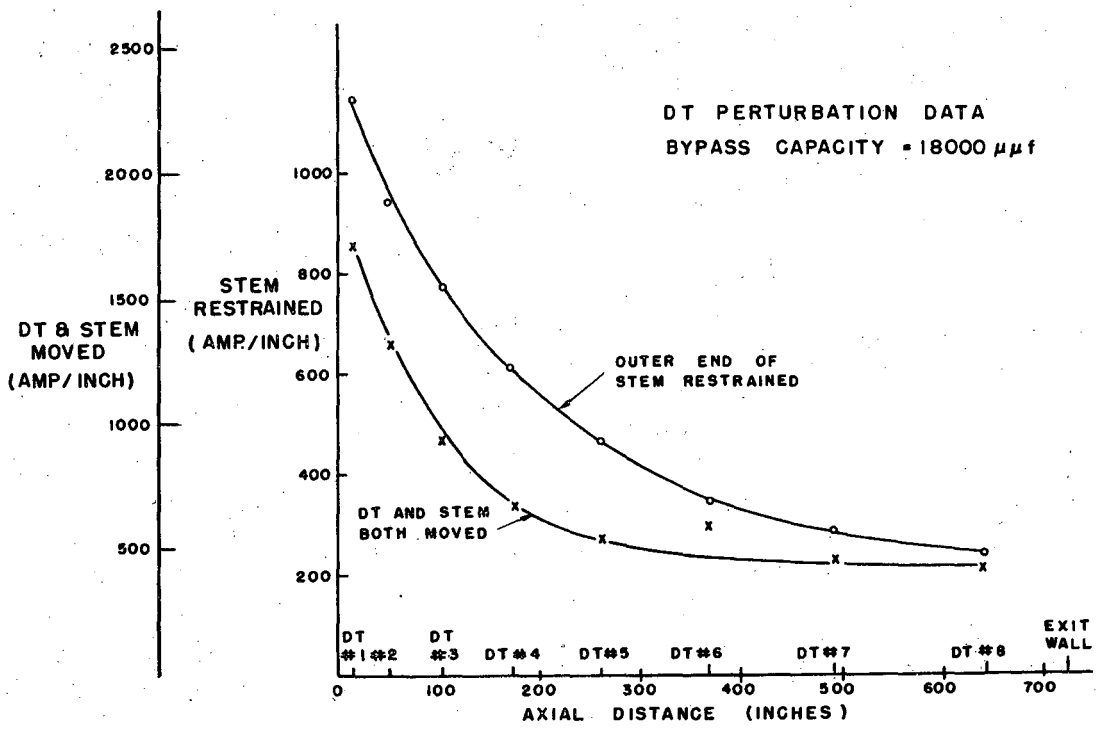

FIG. IX-14

MU 1548

Drift Tube Perturbations

A. Voltage across 18000 $\mu\mu f$ bypass capacitors for movement of both DT and stem axially along cavity.

Drift Tube Number	Average Slope of Perturbation Curve	
	Volts/Inch (Peak)	Amperes/Inch (Peak)
1	624	855
2	480	658
3	343	470
4	244	334
5	196	269
6	217 (180)*	297 (247)*
7	166	227
8	155	212

* Value in parentheses is value from curve of Fig. IX-14.

B. Voltage across 18000 $\mu\mu f$ bypass capacitor for movement of DT with outer end of stem restrained. (This is the condition existing for movement due to focussing magnet forces.)

1	1670	2290
2	1380	1890
3	1130	1550
4	890	1220
5	681	930
6	500	685
7	417	570
8	350	480

Table IX-3

drift tubes numbers 1, 6, 8 by means of a small cord passed through the center hole and back around the outside. Capacitor voltages were measured for several different displacements. The curves again turned out to be straight lines. The remaining slopes were interpolated along a smooth curve joining these three points. Table IX-3B tabulates the slopes of voltage and current for each drift tube. Fig. IX-14 shows a graph of the current slopes as a function of drift tube position.

Note that if the present design figures are used (73 capacitors with ratings 250 $\mu\mu$f, 20 kv, and 20 amperes at 12.1 megacycles) drift tubes number 1, 2, and 3 cannot be allowed to move one-inch from this type of motion or the maximum current rating of $\sim$1400 amperes will be exceeded. This 1400 amperes must include the algebraic sum of the initial current, the current due to the first type of perturbation discussed above, and the current due to this second type of perturbation.

X FIELD MEASUREMENTS ON THE 8½ DRIFT TUBE MODEL

It will be assumed that the reader is acquainted with the preceding sections of this paper because much of the detailed information pertaining to this section is contained in them.

The drift tubes and metal stems were silver plated and assembled with the proper offsets, and the liner nozzles were scaled and mounted on the liner in the proper orientation, i.e., in the center of the 126° sector. A new DT suspension system was designed. The DT assemblies were mounted with the coaxial bypass capacitors used in the previous measurements.

The object of these measurements was to obtain reasonably accurate values for the shunt impedance, Q, the relative losses in the various portions of the cavity, and the stored energy. Explicitly, the measurements required to determine the above quantities are: (a) The tangential magnetic fields at all conducting surfaces to compute the power losses as expressed in Eq. (II-16). (b) The $\int_{\text{field}} B \cdot dA$ over any plane which includes the axis of the cavity as one boundary for computing the end to end voltage, $\bar{V}_c$, of the cavity as expressed in Eq. (II-21). This requires a magnetic field of the chosen plane. (c) The $(\int_V B^2 \cdot dv)$ over the entire volume of the cavity to determine the stored energy as expressed in Eq. (II-23). This infers a map of the magnetic field throughout the volume.

Based on the experience gained on the 7½ drift tube model it was considered sufficient to determine the longitudinal field variations of the cavity by mapping only the variations along the DT transverse center-lines and along the transverse center-lines between DT's. Smooth curves drawn through points of equal radius determine the variations with z. In a given plane, for $\int_{\text{field}} B \cdot dA$, the variations with r are determined by the previous measurement. The volume integration requires that these be extended to include the variations with θ. This is a more subtle variation which results from the irregular polygonal shape of the liner.

A. Procedures for measurement

The following system was set up for taking the various measurements: (a) Two probe supports were built, one along the horizontal slot 90 degrees from the stems (called the A-plane) and the second 180 degrees from the stems (called the B-plane). Both of these planes are of importance because of the 90 degree physical asymmetry which induces a field asymmetry. Figs. X-1 and X-2 show the two probe support members with probes mounted on them. (b) A special set of probes was built with flexible tips for measuring the DT current distributions. (c) A scaled stem was fitted with a special probe for measuring the stem current distributions. (d) A system for regulating, controlling and accurately measuring the cavity level was assembled.

The probes used were the magnetic field sampling probes, described in detail in Section VI, in conjunction with a bolometer detector.

The data identification code (Fig. X-3) indicates the standard nomenclature adopted for identifying the various types of runs made. The data was recorded on special data sheets which included the essential information required for its interpretation and reduction. This information included: (a) probe number (in order to recheck data if necessary); (b) cavity excitation level as measured on the standard monitor loop (described in Section VI); (c) probe reading at the calibration point, which was placed symmetrically with the standard voltmeter loop so that the fields were identical. (See Fig. X-3.) A reading at the calibration point was taken before and after each run to detect any errors due to cavity level shifting or probe changing during the run. A maximum difference of 3 percent was allowed in the two readings for acceptable data. The average of the two readings was used as a normalization value to reduce all data to the same relative cavity level. (d) A $0-\pi$ ratio was measured for the probe as an index of its reliability in the presence of electric fields as

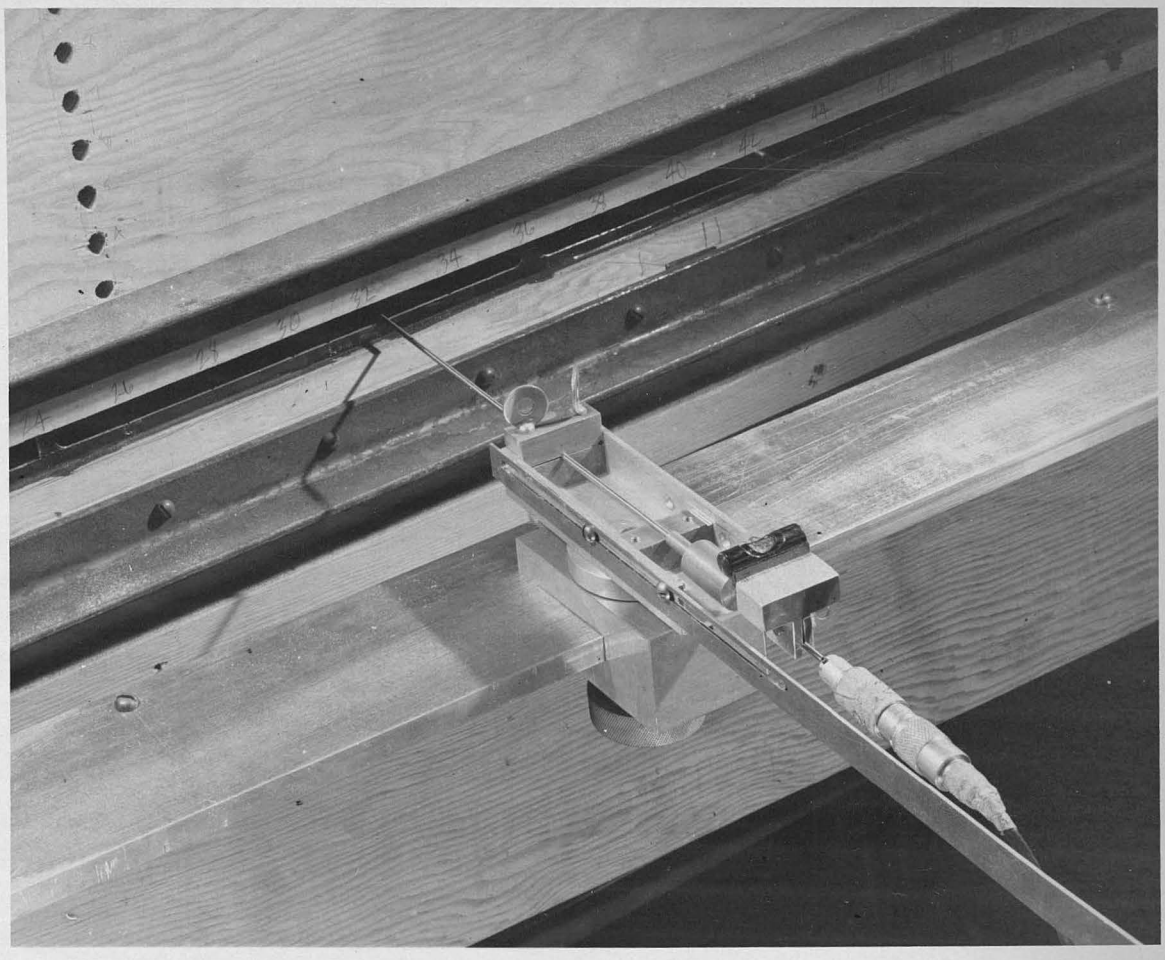

A - PLANE PROBE SUPPORT RACK

FIG. X-1

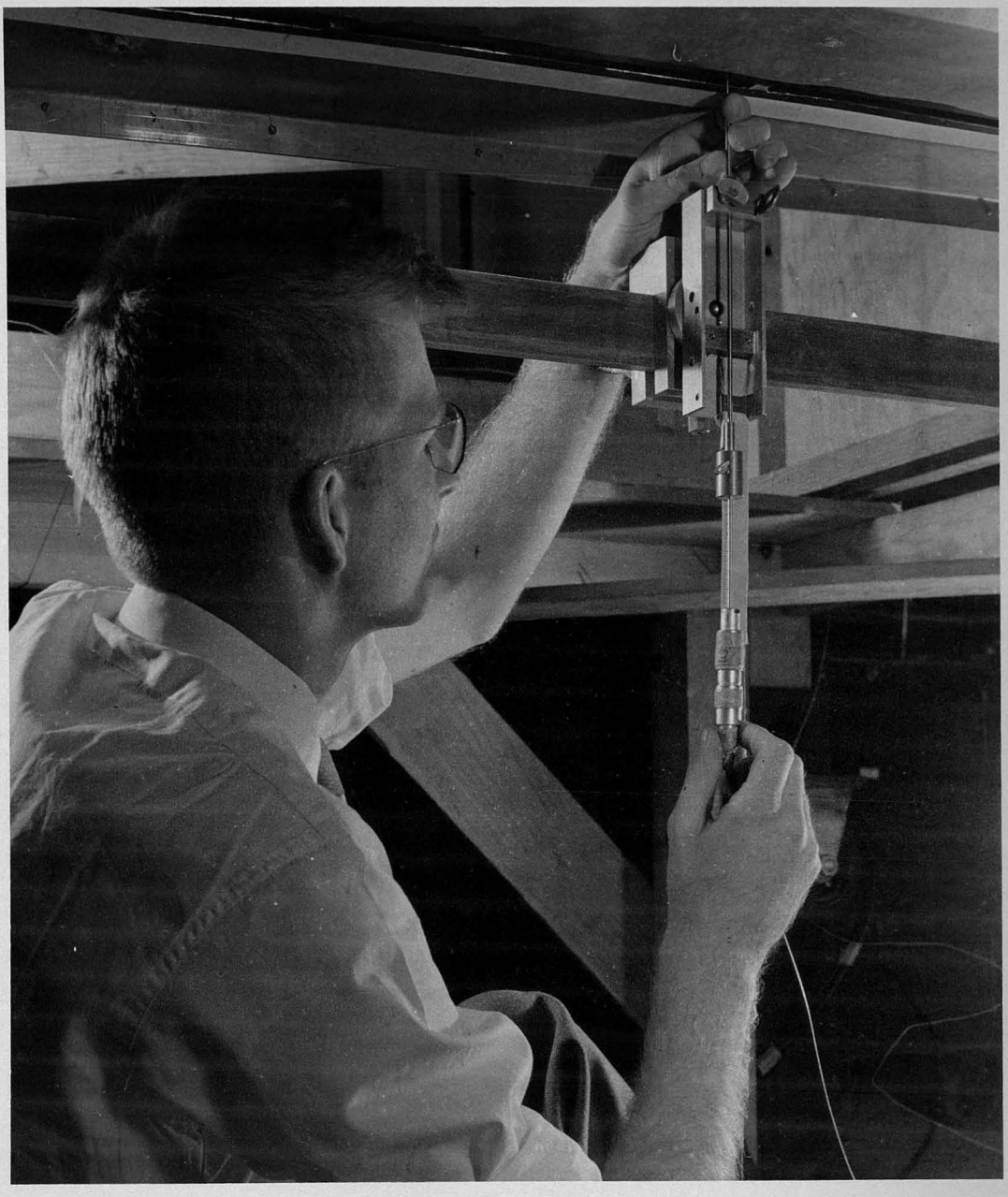

B - PLANE PROBE SUPPORT RACK

FIG. X-2

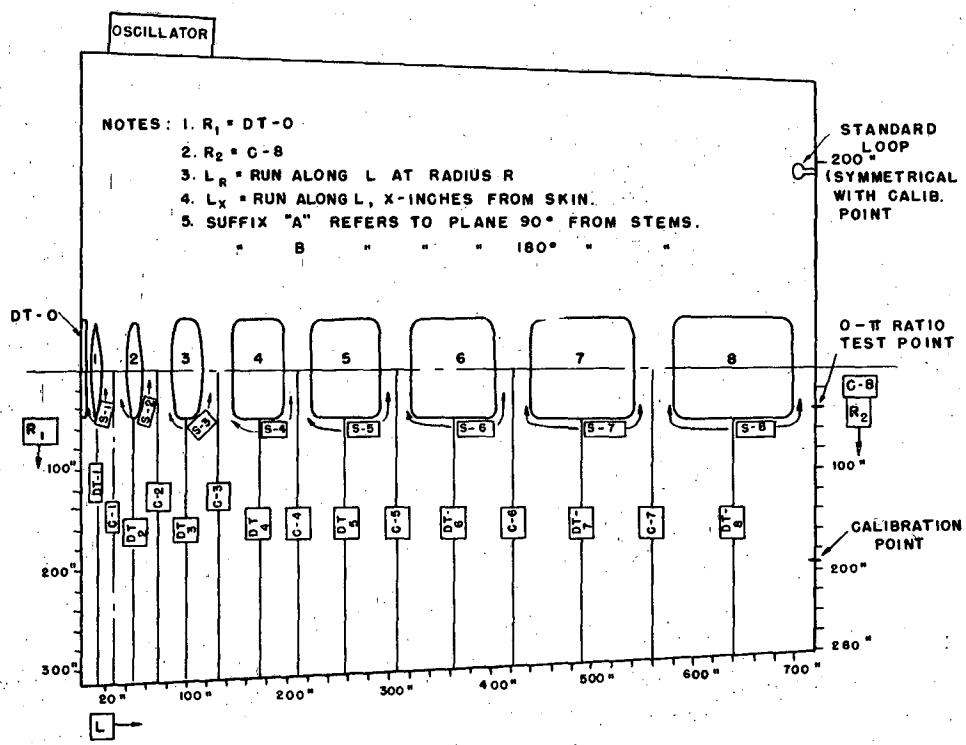

DATA IDENTIFICATION CODE

FIG. X-3

MU 1549

detailed in Section VI. (e) The actual data was read on the bolometer bridge meter in terms of "milliwatts" which were proportional to B^2, the square of the magnetic induction field at the position of the probe.

B. Field mapping ($\int_{\text{field}} B \cdot dA$)

There are two obvious planes for measuring the $\int_{\text{field}} B \cdot dA$. These are the two planes of symmetry of the cavity which have been previously denoted in Fig. III-1 by "A" and "B." The measurements on each plane are divided into two categories: (a) runs along the transverse center-line of the DT's denoted by "DT" and (b) runs along the center-lines between drift tubes denoted by "C." It should be noted that the entrance end wall is denoted by R_1 but is also the center-line of the half DT mounted on the entrance end and hence is also DT-0. Similarly the exit wall is denoted by R_2 but it also C-8 since it is between DT-8 and what would be DT-9 if the tank were extended.

The following sequence of operations for a particular set of measurements is included in order to give a clear picture of the proceedings. Fig. X-4 is a diagram of the general setup and Fig. VI-10 is a photograph of the oscillator control cabinet and standardizing equipment.

As preliminary measures the oscillator was tuned, the standardizing equipment balanced for the proper level of approximately 4 volts, and the data sheet heading filled out. Two persons were required: (a) the recorder, who maintained the proper cavity level by adjusting the oscillator plate voltage, zeroed and read the bolometer bridge, and recorded the data, and (b) the probe operator who controlled the movements of the probe and determined its position in the cavity.

Step 1. Probe selection and test for 0-π ratio.

The probe was inserted in the cavity at the 0-π ratio test point (see Section VI) indicated on Figs. X-3 and X-4. If the ratio was $0.95 < F_0/F_\pi < 1.05$,

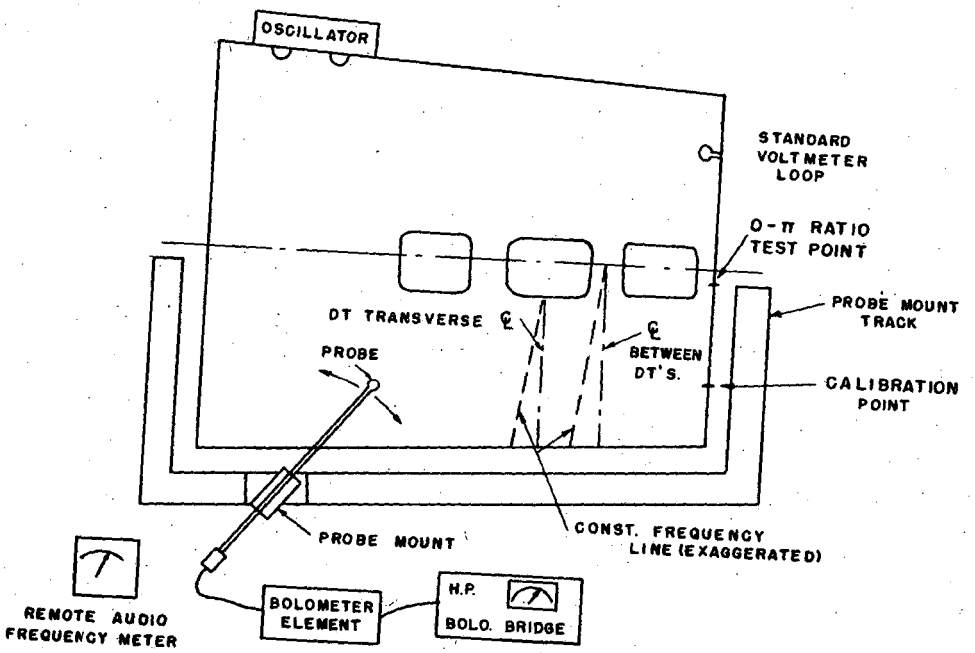

FIELD MAPPING "A" - PLANE

FIG. X - 4

MU 1550

the probe was considered acceptable.

Step 2. Probe positioning.

The probe was mounted on the holder but not inserted in the cavity. The audio beat note between cavity frequency and the standard oscillator frequency was then adjusted to be about one kilocycle and a remote meter indicating relative audio frequency placed in view of the operator. Noting the meter reading the probe was inserted almost to the DT and pointed directly at the transverse center-line of the DT (assuming the run to be made is a DT run). Retaining this inner position the probe was rotated about the center of the mount and translated along the cavity until the original audio frequency was obtained. Then the probe was slowly withdrawn in a straight line and the deviation meter observed. If the meter showed a variation of more than 50 cycles (model) during the process the angular position was poorly set or the probe was not straight over its entire length.* Usually about two or three adjustments were sufficient to provide a good position.

Step 3. Probe insertion calibration.

A dummy probe was inserted until it touched the DT (with the rf off) and the length from the inside of the liner wall was measured accurately. The first position of the good probe was then set to be $\frac{1}{4}$ inch less than this as measured to the center of the pickup loop. The distance from the DT transverse center-line at the liner wall to the position where the probe cut the liner wall was then measured. The ruler used for measuring the probe insertion was set so that the desired readings fell on even inch, or fraction of inch, marks.

Step 4. Level bubble set.

The probe was inserted at the calibration point of Figs. X-3 and X-4 and

* Except for a narrow region of probe resonance about 21 inches from the liner.

supported horizontally at the outer end. It was then carefully rotated about the probe stem axis until the maximum reading was obtained on the bolo.-4. The level bubble (Fig. X-1) was then clamped in a level position. This adjustment was checked several times. The purpose of this was to allow the operator to set the probe for maximum signal without seeing the bolometer. It should be noted that in the B-plane where the probe is vertical this was not possible and the probe was then rotated slowly and the maximum value read by the recorder.

Step 5. While set at the calibration point a reading was taken and recorded.

Step 6. The data.

The probe was again inserted in the cavity at the desired position and a set of readings were taken starting with the innermost point. The number of points taken was varied with the variation of the field. In the region of a DT, readings were made every $\frac{1}{4}$ inch and near the liner every inch.

Step 7. The probe was again placed at the calibration point and a reading taken. Differences between this reading and the one taken in Step 5 usually varied about 1 percent and if the variation was more than 3 percent the run was not accepted.

Step 8. The data was reduced in a standard manner by the following steps: (a) The probe position, originally taken in inches from the wall for convenience, was converted to inches of radius from the center-line. (b) Bolometer readings were corrected from the instrument calibration curve (detailed in Section VI). These readings, which are proportional to the square of the magnetic induction field, B^2, we call F^2. (c) Corrected readings were normalized by the calibration point reading, resulting in a dimensionless quantity which we call F_N^2. (d) The square root of this value, F_N, is proportional to B and from Eq. (II-71) the absolute magnetic field, $B = F_N B'$, where B' is the absolute field at the position of the standard voltage loop.

The above procedure was modified slightly to take care of the special requirements of the various types of runs made. In the case of the "C" runs there were no critical measurement points near the DT so it was not necessary to carry out Step 3. For these runs the probe was aimed at the junction of the cavity center-line and the transverse center-line between DT's. In the case of the runs along R_1 and R_2 which are metal boundaries, and hence force the field lines to conform to the boundary conditions, it was not necessary to laboriously align the probe along a line of constant frequency, as indicated in Step 2. It was sufficient to take the readings with the probe $\frac{1}{2}$ inch from the metal boundaries.

In mapping the B-plane the operator sat beneath the cavity as shown in Fig. X-2. Except for the level bubble which is inoperative in this position, measurements were made as for the A-plane.

The graphs of F_N vs. r for the DT's were all placed on one sheet in order to check their compatibility. From this plot it was clear that a few of the curves did not fit into the scheme of things. These curves were readjusted to make the family of curves look reasonable. In no case was the readjustment of any curve more than 2 percent. (This is less than the desired error of measurement.) The resulting curves for the A-plane are shown in Figs. X-5 and X-6; for the B-plane in Figs. X-7 and X-8. As a final check of consistency of the data near the DT's a plot was made of the fields at the DT skin. This plot is shown in Fig. X-9 and includes data for both A- and B-planes. The results are remarkably consistent. The break in the curve is apparently due to change in shape of the contour of the first three DT's. For the last five, the ends have the same contours and vary only in length.

A similar set of plots for the "C" curves was made and treated in the same manner. Figs. X-10 and X-11 are for the A-plane and Figs. X-12 and X-13 are for

MAGNETIC FIELD ON DRIFT TUBE LONGITUDINAL CENTER-LINES
ON THE A-PLANE vs RADIUS FOR DRIFT TUBE NOS. 1-4

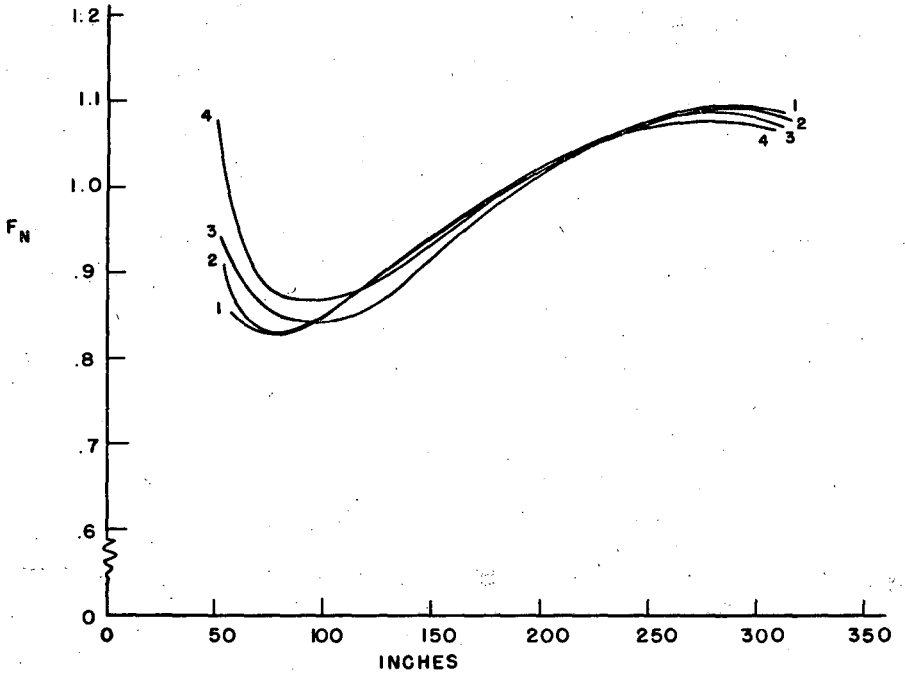

FIG. X-5

MU 1551

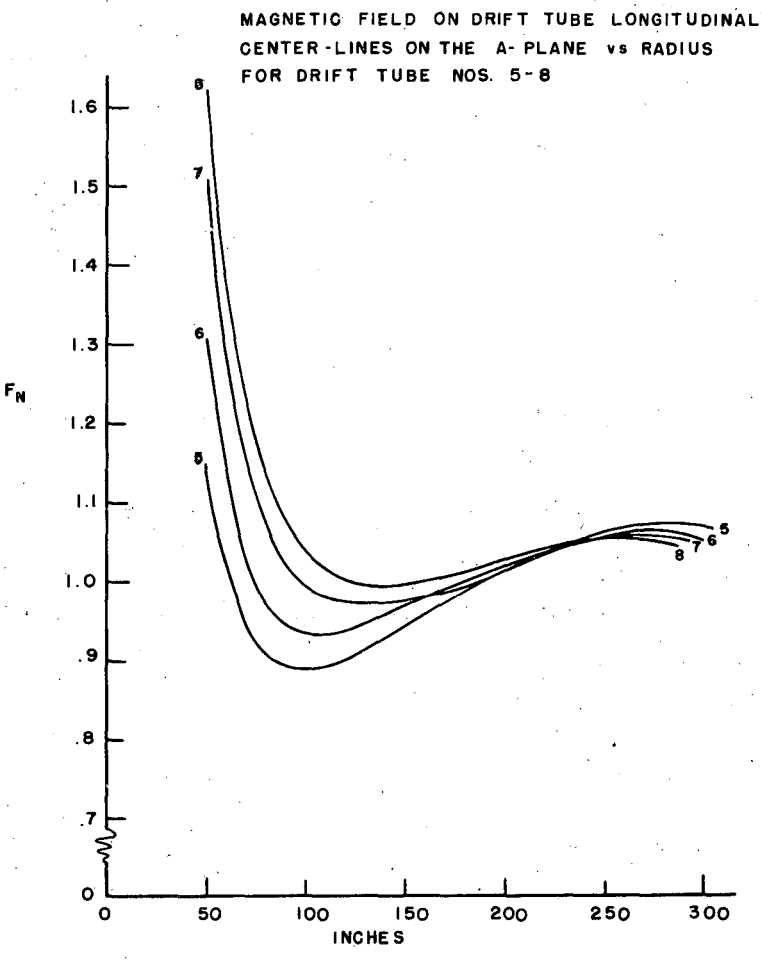

FIG. X-6

MU 1552

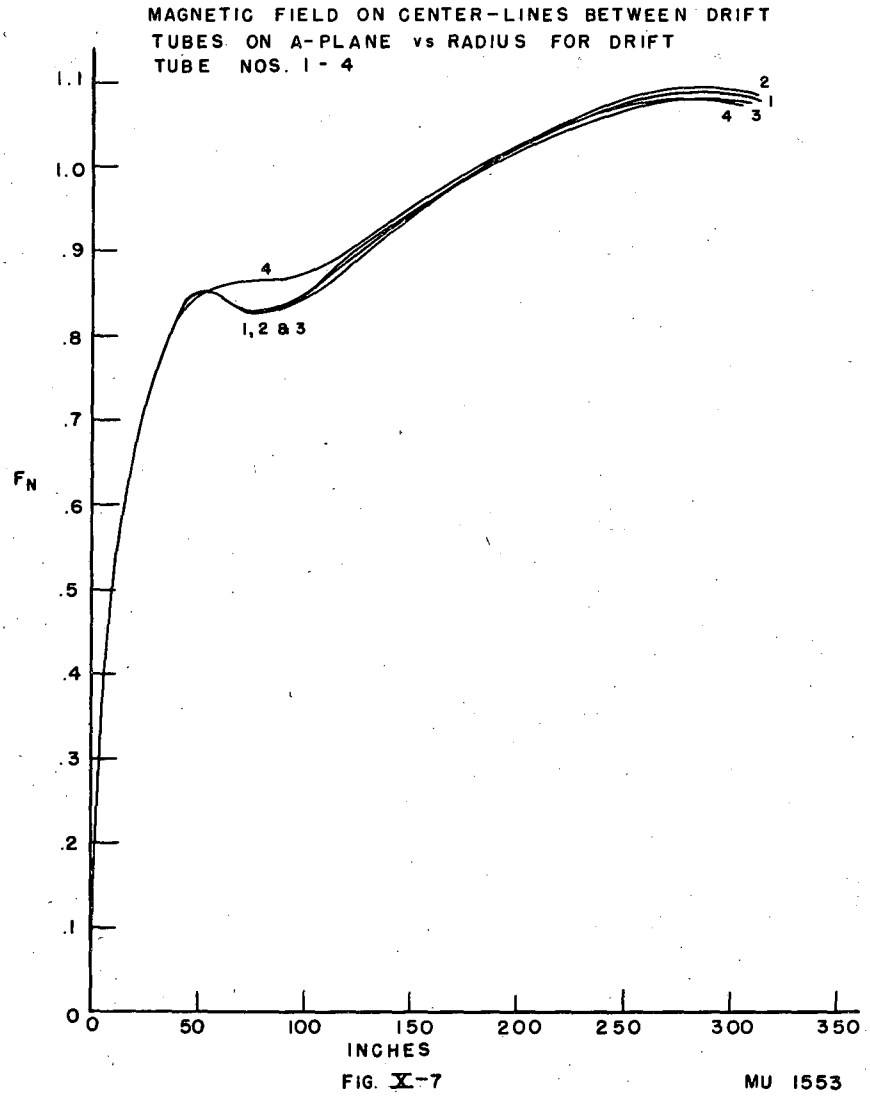

FIG. X-7

MU 1553

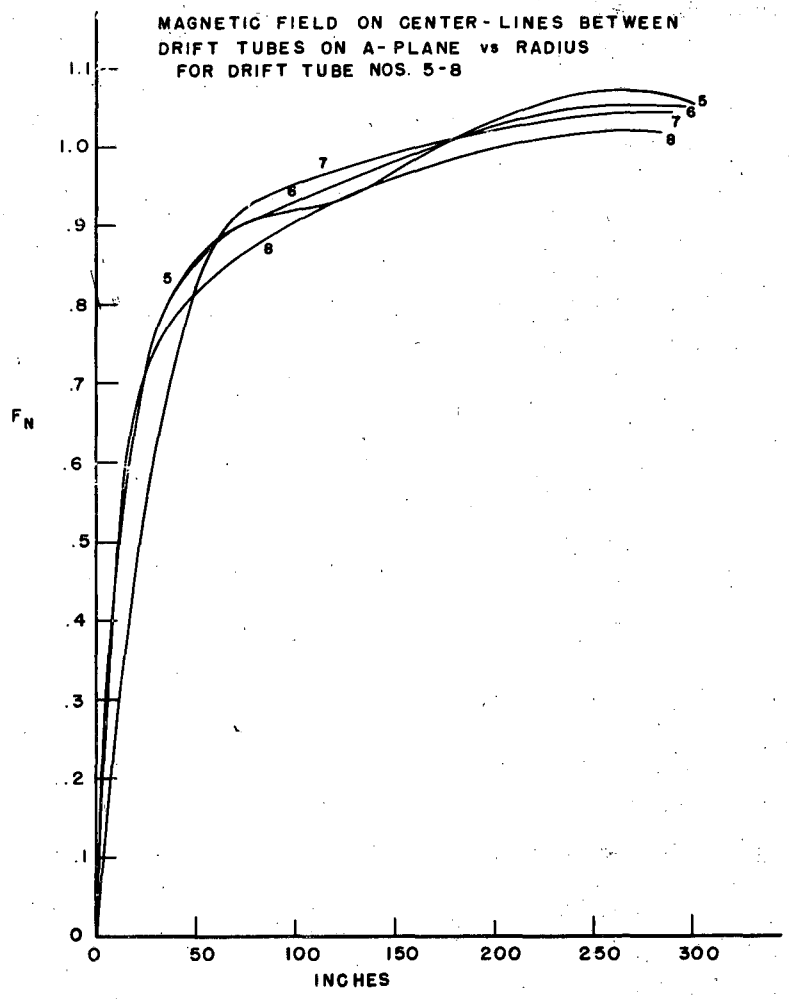

FIG. X-8

MU 1554

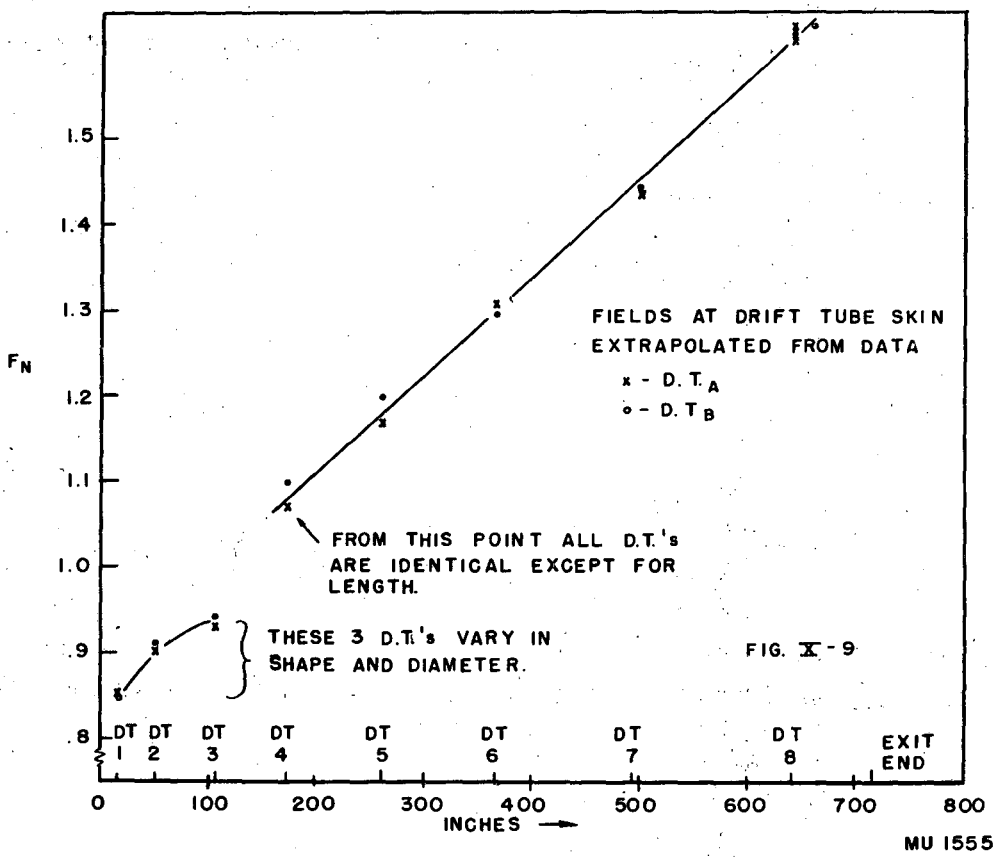
1.5
1.4
1.3
1.2
1.1
1.0
.9
.8
F_N
FIELDS AT DRIFT TUBE SKIN
EXTRAPOLATED FROM DATA
x - D.T.A
o - D.TB
FROM THIS POINT ALL D.T.'s
ARE IDENTICAL EXCEPT FOR
LENGTH.
THESE 3 D.T.'s VARY IN
SHAPE AND DIAMETER.
FIG. X-9
DT 1
DT 2
DT 3
DT 4
DT 5
DT 6
DT 7
DT 8
EXIT END
0
100
200
300
400
500
600
700
800
INCHES
MU 1555

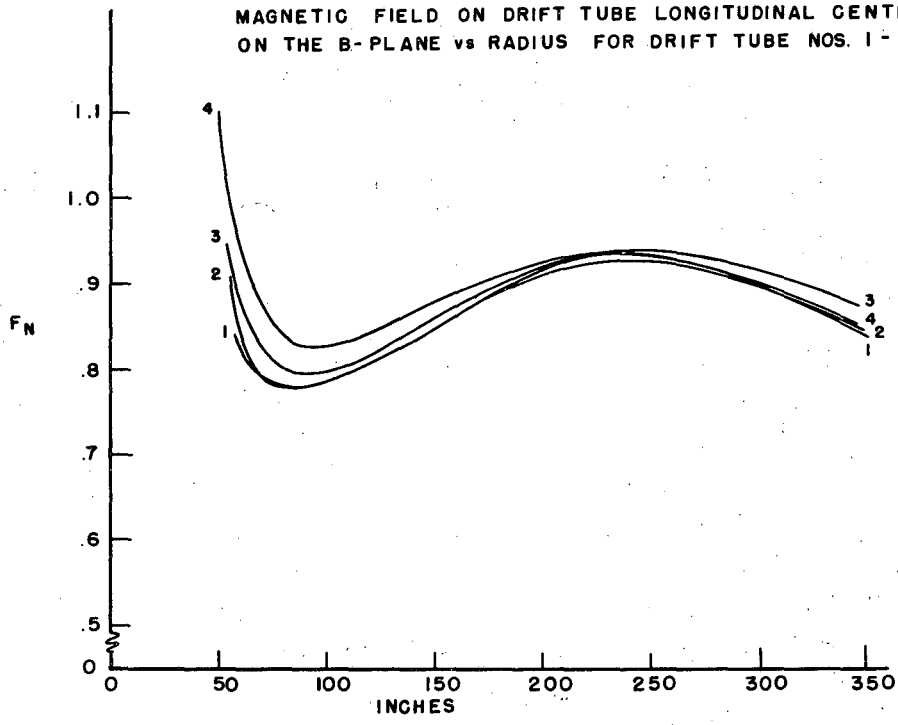

FIG. X-10

MU 1556

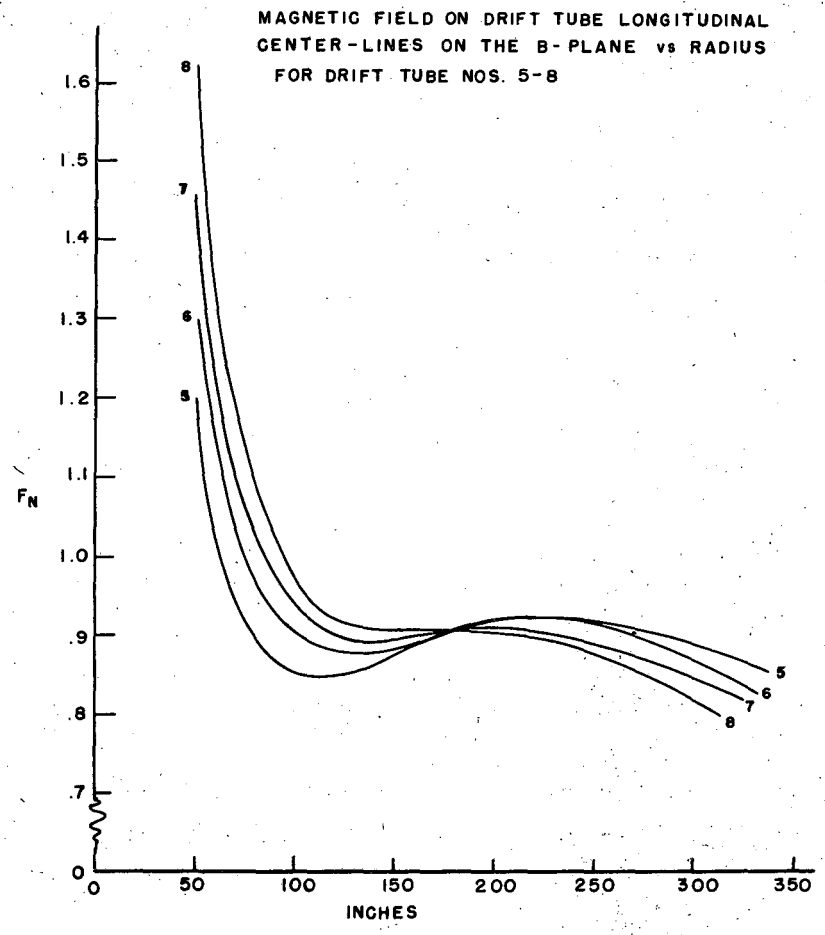

FIG. X - 11

MU 1557

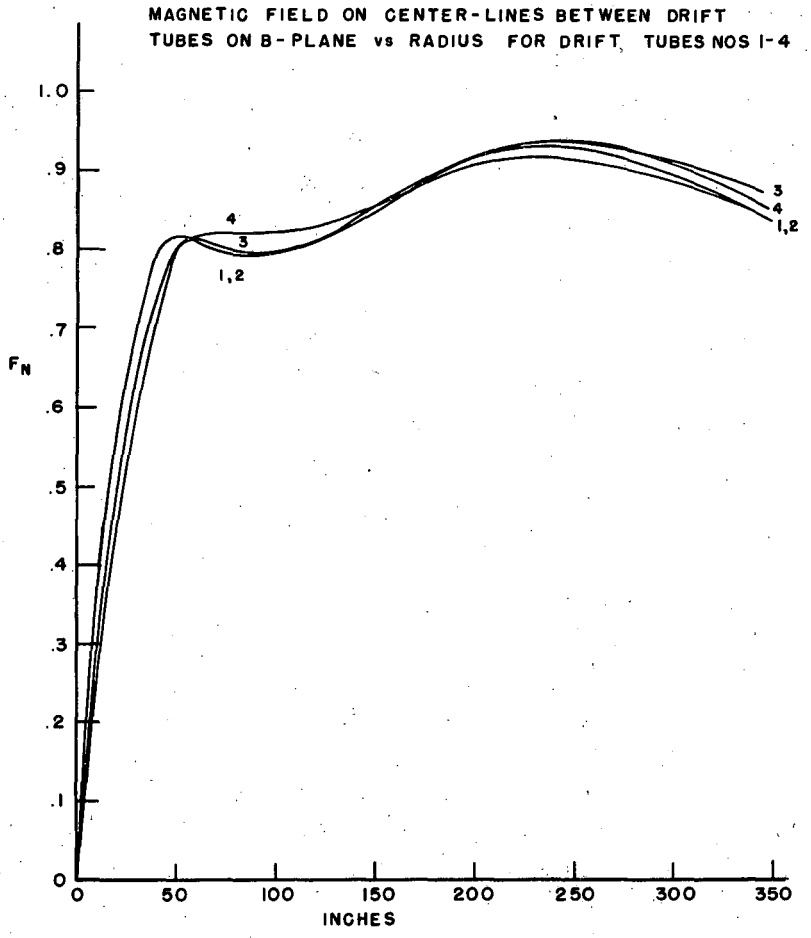

FIG. X-12

MU 1558

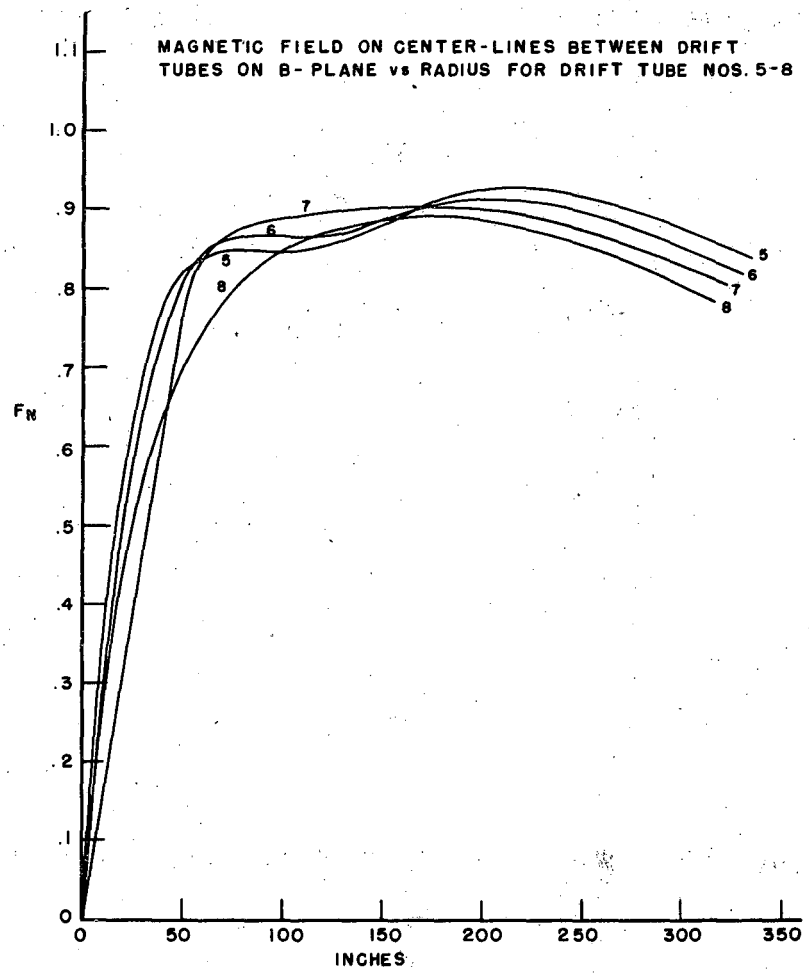

FIG. X-13

MU 1559

the B-plane.

From the above curves the $\int B \cdot dA$ was obtained by graphical integration. The integration areas for Cell #5 are shown in Fig. X-14. For any given radius the relative field, F_{NR}, to be used along with the area associated with that radius is obtained by averaging the value of F_N from the curves for DT-4, C-4, and DT-5 at that radius. This is not an exact evaluation, but since the variation is small over the length of the cell except very near the DT as evidenced by the curves of Fig. X-15 (which are curves of F_N vs. z at constant radius the error is very small. A value of F_{NR} was obtained for each radius listed above the integration area charts. This value was multiplied by the area within which it fell. This area is $(\Delta r)(\ell)$ where Δr is found beneath the charts and ℓ is the length of the cell (8.75 inches model dim. for Cell #5). The product $(F_{NR})(\Delta r)(\ell)$ was then summed over the entire plane. Each cell was treated in the same manner for both the A- and B-planes. The $k \int_{field} B \cdot dA$ for the entire plane is then found by summing all the cell contributions for that plane. The results from the two planes should be identical according to theory. The total integral was calculated in three ways: plane A by the DT-cell-2 method (see Fig. I-1 for definition of DT-cell-1 and cell-2) and plane B by the DT-cell-2 method and also by the DT-cell-1 method. Table X-1 compiles these results.

Table X-1

Results of Field Integration to Obtain $\int_{field} F_N \cdot dA$

Plane	Method of dividing areas	$\int_{field} F_N \cdot dA$
A	DT-cell-2	115.3 meter^2
B	DT-cell-2	115.9
B	DT-cell-1	117.7
	Average	116.3

Note: See Fig. I-1 for definition of DT-cell-1 and DT-cell-2.

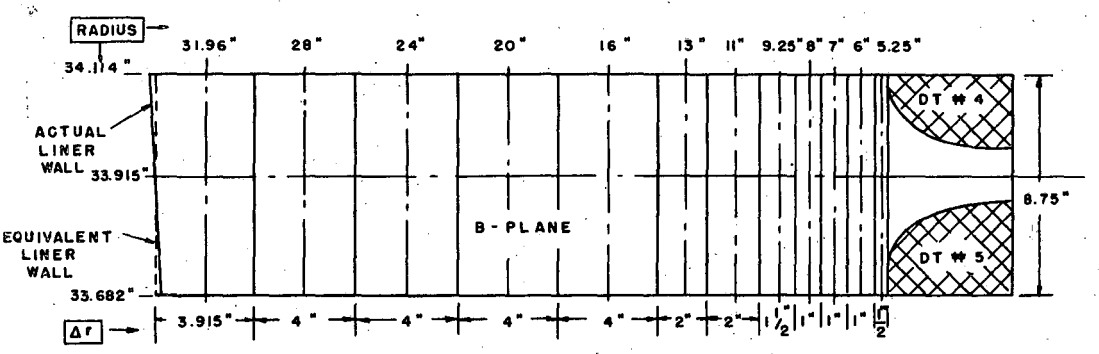

NOTE: THE AREA BETWEEN DT'S IS NEGLECTED IN THE INTEGRATION. ALL DIMENSIONS ARE FOR MODEL.

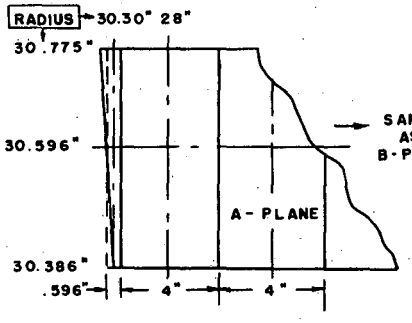

CELL DIVISION INTEGRATION AREAS FOR CELL # 5

RELATIVE FIELD, F_{NR}, FOR ANY AREA IS:

$$F_{NR} = \left[\frac{F_N|_{DT-4} + F_N|_{C-4} + F_N|_{DT-5}}{3} \right] @ \text{RADIUS } r$$

$$K \int_{\substack{\text{B-PLANE} \\ \text{DT \# 5}}} B \cdot dA = \sum_{r=5}^{33.915} \left[F_{NR} \times f_x \times \Delta r \right]$$

$$K \int_{\substack{\text{A-PLANE} \\ \text{DT \# 5}}} B \cdot dA = \sum_{r=5}^{30.596} \left[F_{NR} \times f_x \times \Delta r \right]$$

FIG. X - 14

MU 1560

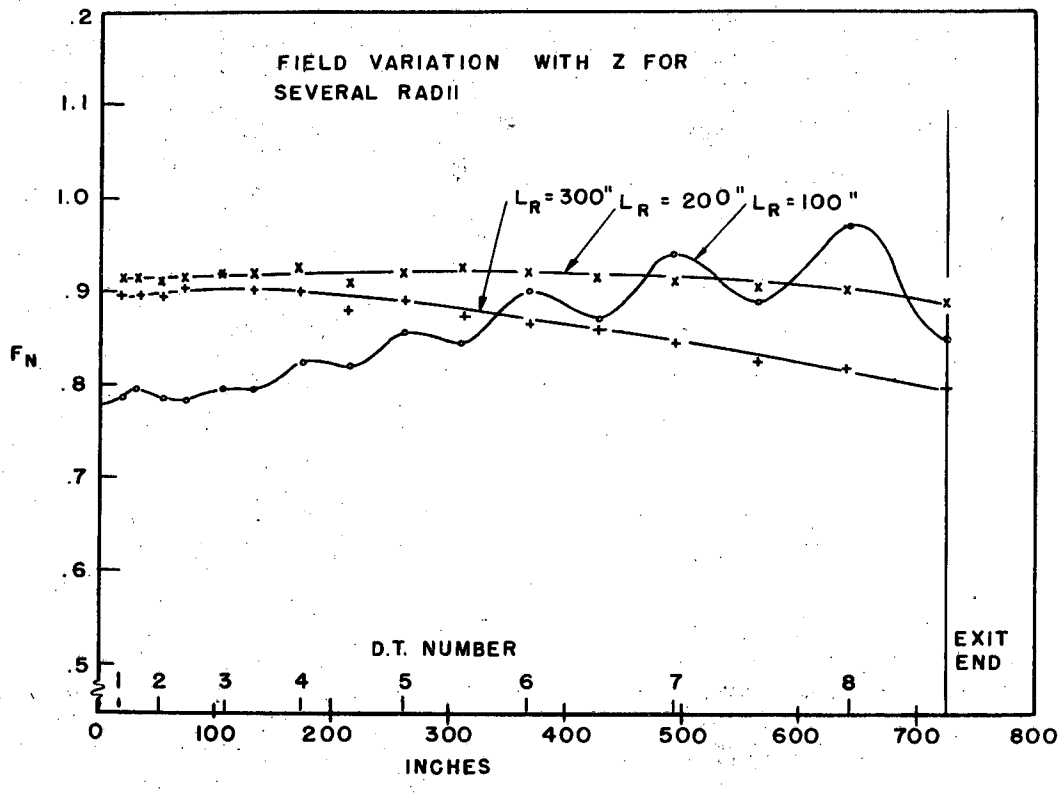

FIG. X - 15

MU 1561

Aside from the total integral, the individual cell integrals are also of some interest when plotted as a function of cell number. Table X-2 indicates the results in terms of the design end-to-end voltage of 45.18×10^6 volts. The results tabulated are also plotted on Fig. X-16.

Table X-2

Peak RF Voltage per Cell

Cell Number	Peak Voltage per Cell	% Total per Cell
1	1.059×10^6	2.34
2	2.192	4.85
3	3.332	7.37
4	4.468	9.89
5	5.565	12.31
6	6.762	14.96
7	7.931	17.55
8	9.011	19.94
9*	4.860	10.75
	$\sum = 45.180$	99.96

* #9 cell is the last half gap and has therefore approximately one-half the voltage as a full cell (but less because the next half-cell would have a greater voltage).

The design of the machine was made with the hope that the curve of Fig. X-16 would be a straight line and it was very gratifying to know that it is very near to that.

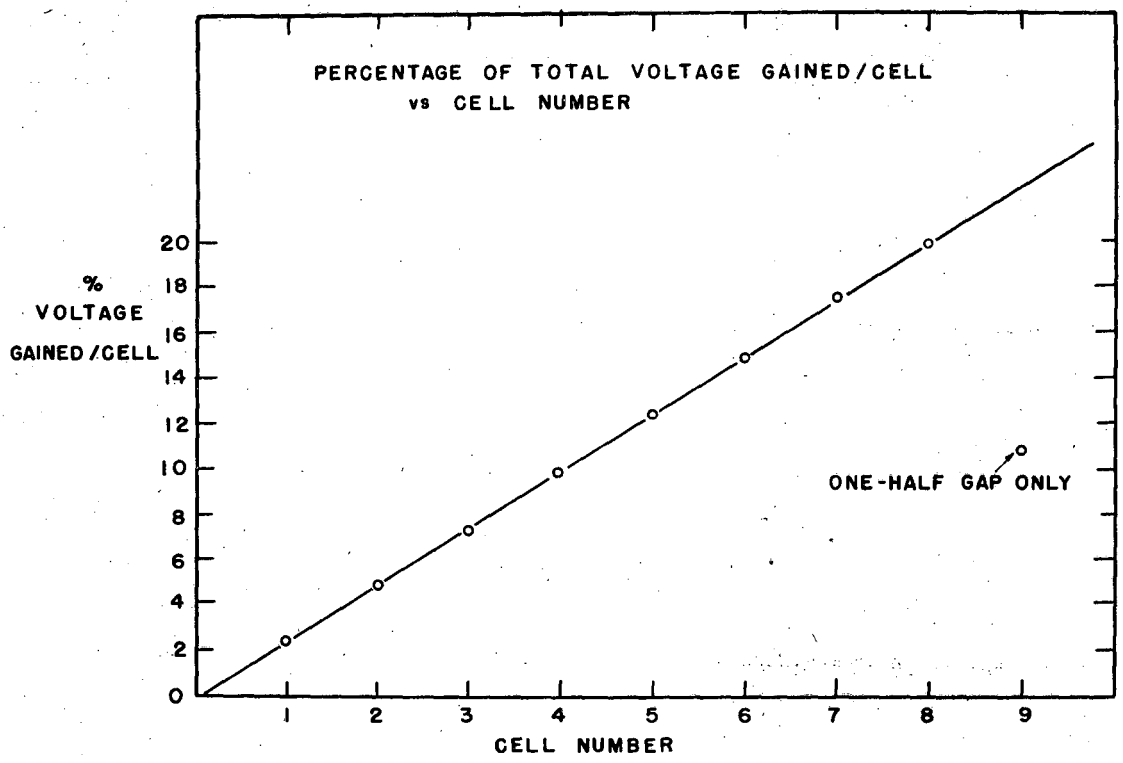

FIG. X - 16

MU 1582

C. Volume integration

In addition to the above data taken in the A- and B-planes it was necessary to take enough data to obtain the angular distribution of field with radius. This is necessary because the outer conducting boundary is not a circular cylinder but an irregular polygon (with the A- and B-planes of symmetry). The corners of this polygon are points of zero magnetic field* and hence of zero current in the liner. The field perturbation due to these corners is a maximum at the conducting boundary and "washes out" as the center of the cavity is approached. In order to get a reasonably clear picture of the manner in which the field varied, data was taken radially at the 0, 9, 18, 27, 36, 45, 54, 63, and 90 degree angles around the cavity and at the center-line of DT #5. Fig. X-17 shows one-quarter of the cavity with these angles indicated on it. They correspond to the corners of the polygon and the center-lines of the sides. These data were left in terms of F_N^2 because the integrals in which they are used are in terms of B^2. They were normalized a second time to the value of F_N^2 in the B-plane at the same radius (call these values F_{NB}^2). This had several advantages, the chief one of which was the fact that curves when plotted as a function of radius for constant angle show very clearly when the distribution starts to deviate from the distribution of the B-plane. Such a set of curves is shown in Figs. X-18 and X-19.

In addition to this radial data, the distributions across the wide flat (at the 90 degree point) and the narrow flat (at the zero degree point) were taken one-half inch inside the cavity. A plot of these two curves, each normalized to its own maximum value, is shown in Fig. X-20A. Fig. X-20B shows variation of field with θ. It was not possible to measure exactly in the corner because of the finite size of the probe and the erroneous readings due to images of the probe when it is closer than about one-half inch to the conducting

* This can be shown mathematically through the use of a Schwarz transform but will not be treated rigorously here.

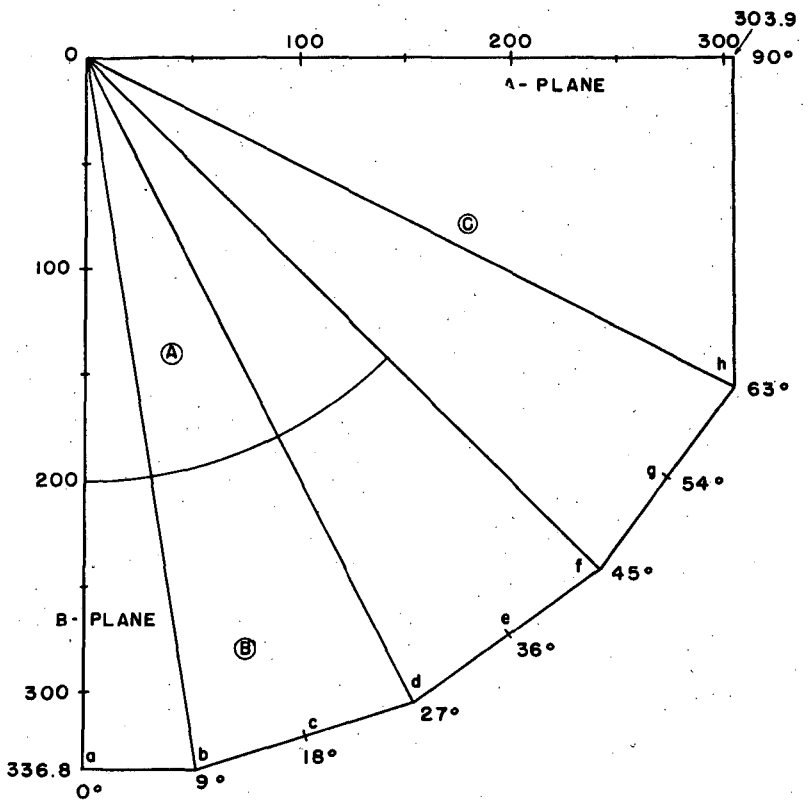

CAVITY GEOMETRY AND REGIONS
FOR VOLUME INTEGRATION.

FIG. X - 17

MU 1563

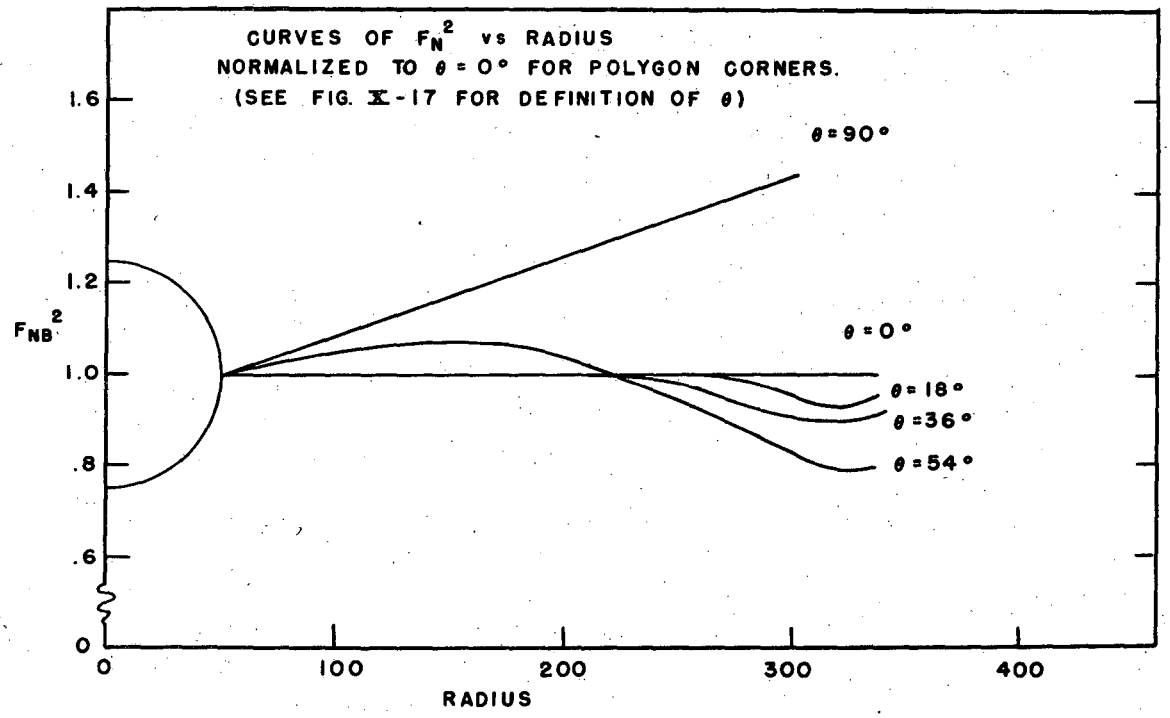

FIG. X-18

MU 1564

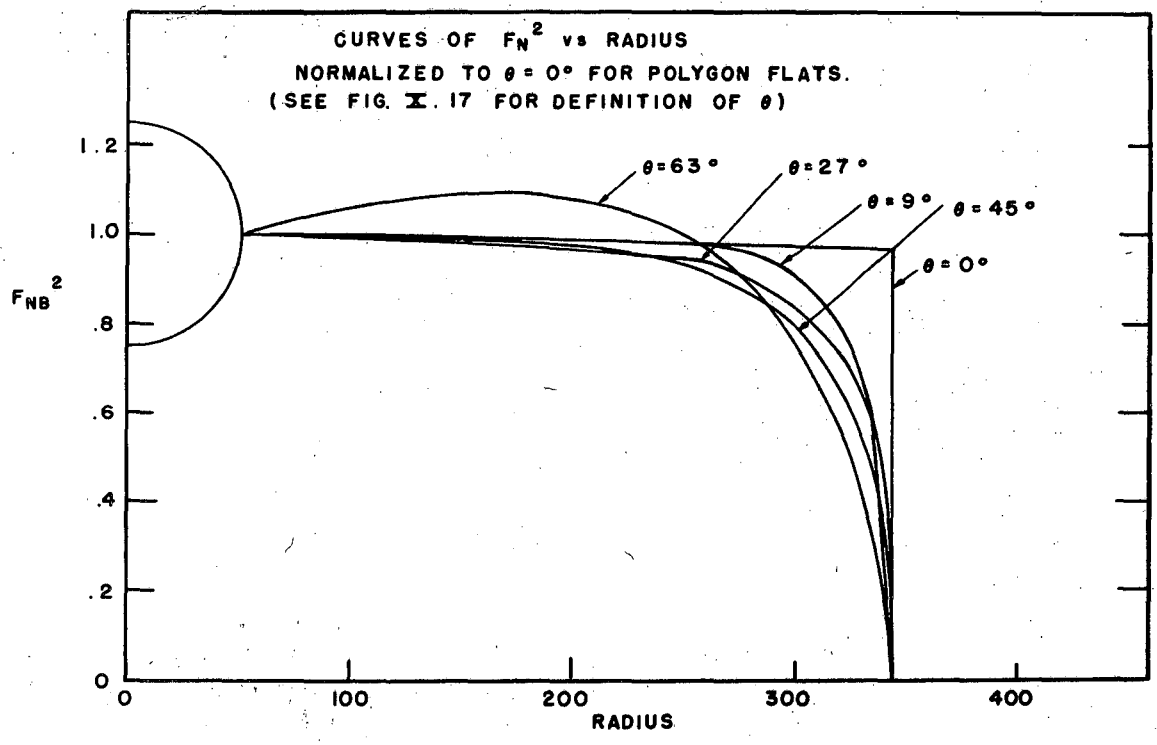

FIG. X-19

MU 1565

Dimensions are for model
(Multiply by 10 for full scale)

NORMALIZED F_N^2 DISTRIBUTIONS ACROSS POLYGON SIDES AT LINER WALL.

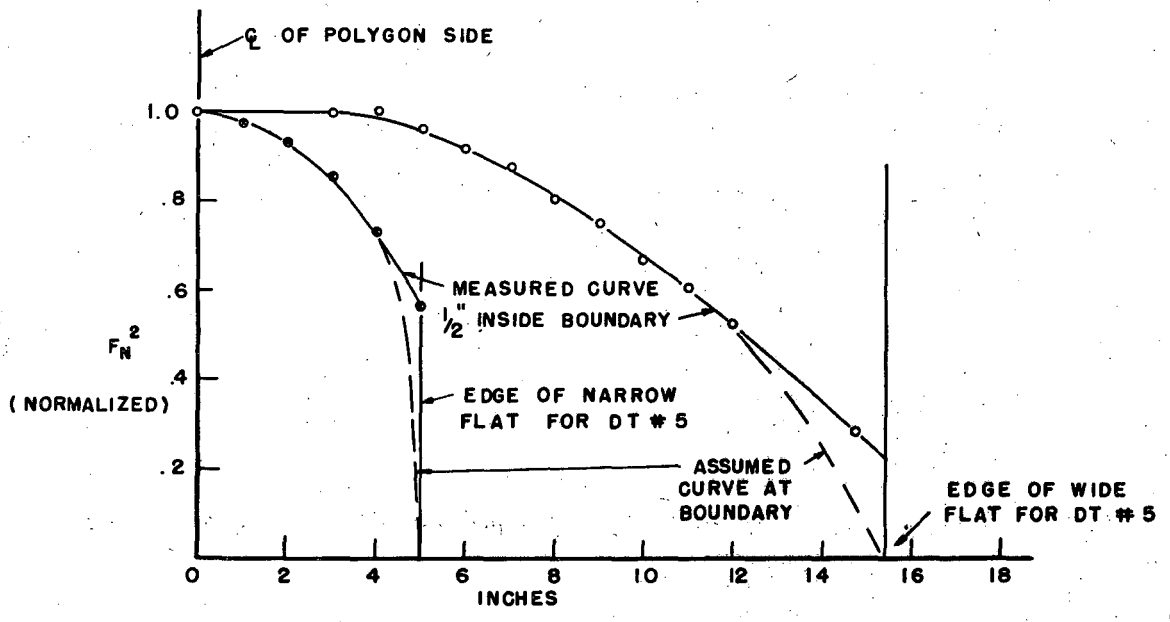

FIG. X - 20A

MU 1566

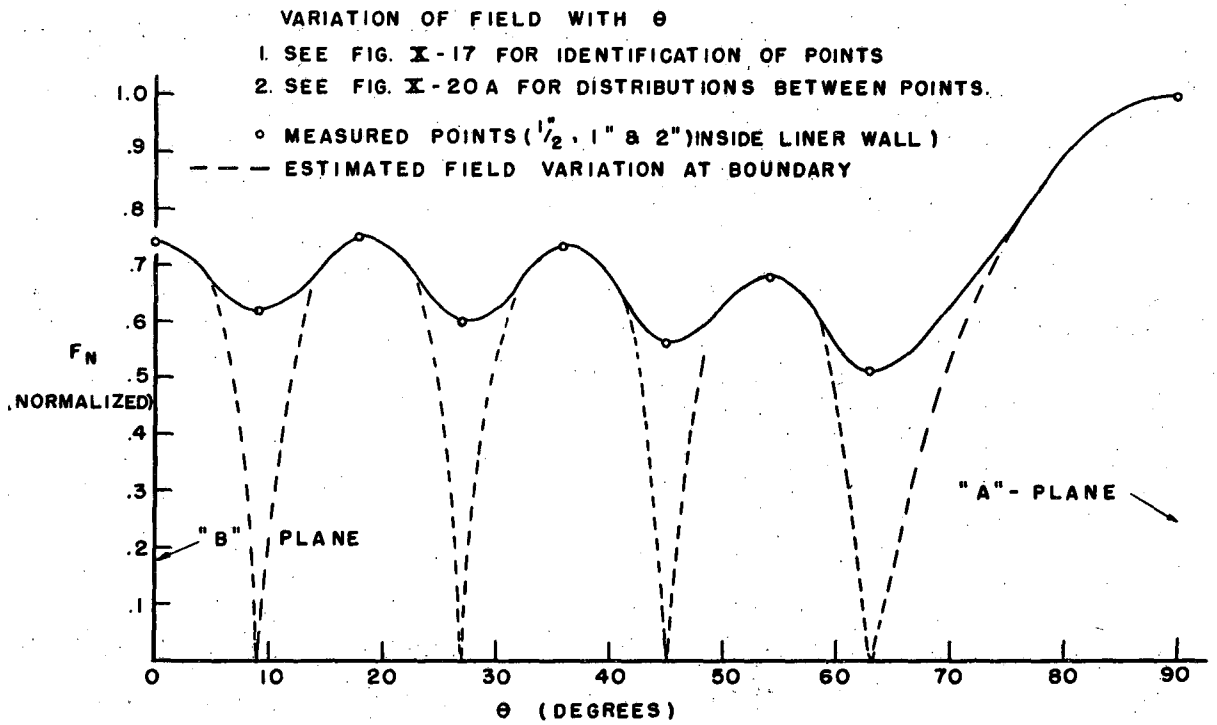

FIG. X-20B

MU 1567

boundary. It was assumed that the field did go to zero in the corner and the curve was extrapolated smoothly to this point as shown by the dashed line.

The actual volume integration will not be dealt with in detail, but it was carried out in roughly the following steps:

1. On the basis of the curves of Figs. X-18 and X-19 the areas of integration as shown by Ⓐ, Ⓑ, and Ⓒ on Fig. X-17 were chosen. In region Ⓐ the fields are uniform with θ and hence can be integrated in a straightforward manner using the distributions of the B-plane. Areas Ⓑ and Ⓒ require special treatment.

2. The integration was carried out by plotting curves of constant radius from the curves of constant θ. This was done for the average radius of each small area of integration within Ⓐ and Ⓑ. The resulting curves were integrated graphically to obtain the average F_N^2 over the 45 degree sector.

3. From this value an area integral was obtained by multiplying by the area of the individual sectors.

4. As a convenience in extending to the volume these areas were normalized to the maximum radius at DT-5. This left the data in a completely normalized form, i.e., none of the dimensions or values of DT-5 were included.

5. All DT areas were normalized in radius to the maximum radius at the DT center-line included in that area.

6. Curves of the average F_N^2 plotted against normalized radius were drawn using the average across the DT-area obtained in a manner similar to that used in determining the $\int B \cdot dA$ above.

7. To convert the results of step 3 into the volume integration it was necessary to multiply the individual areas by the square of the radius and the average F_N^2 of the DT-area under consideration. This value when multiplied by length of the DT-area provided the volume integral of that area. The

complete volume integration is found by summing the individual DT-area integrations.

The results of this integration, in terms of F_N^2 are:

$$\int_{\text{volume}} F_N^2 \cdot dv = 3.03 \times 10^3 \text{ (meters}^3\text{)} . \qquad \text{(X-1)}$$

D. Losses

The losses in the machine were calculated from the magnetic fields at the conducting boundaries using Eq. (II-16). There are a number of types of geometries which must be treated separately, e.g., ends, side panels, drift tubes, and stems. Table X-3 tabulates the results for these various portions of the machine and the following paragraphs sketch briefly the method for determining each.

The end losses can be calculated from an intermediate step in the volume integration of the preceding section. Step 4 of that integration is $\int F_{NB}^2 \, ds$ over a normalized plane parallel to the ends, where F_{NB}^2 is F_N^2 normalized to the value on the B-plane. To remove the normalization it was necessary to multiply by the square of the radius and the value of F_N^2 on the B-plane at each end separately. This yields $\int F_N^2 \cdot ds$ for one-fourth the entrance and exit ends respectively.

The side panels are of two different sizes, the wide panels perpendicular to the A-plane and the narrow panels making up the remainder of the liner. The distribution across each of these panels is shown in Fig. X-20A.

The stem losses were calculated using the relation of Eq. (II-83) for the field distribution around the stem. This assumes that all of the losses are due to longitudinal currents arising from the insertion of the stem in the field, i.e., that no losses arise from the circumferential currents discussed in

Detail of Losses

	$\int F_N^2 \cdot ds$ meters^2	% Losses	% Total Losses	Mega-watts Loss
(a) Liner				
Entrance end		20.6	15.2	1.333
Exit end		16.2	11.9	1.044
Side panels		63.2	46.8	4.104
Total	871.7	100	73.9	6.481
(b) Drift Tubes				
DT #0		2.1	.3	.026
#1		4.3	.6	.053
#2		5.2	.8	.070
#3		5.5	.8	.070
#4		8.2	1.2	.105
#5		11.2	1.7	.149
#6		14.9	2.2	.193
#7		20.0	3.0	.264
#8		28.6	4.2	.368
Total	174.5	100.0	14.8	1.298
(c) Drift Tube Stems				
Stem #1		11.8	1.3	.114
#2		12.0	1.3	.114
#3		12.2	1.4	.123
#4		12.5	1.4	.123
#5		12.5	1.4	.123
#6		13.0	1.5	.131
#7		13.0	1.5	.131
#8		13.0	1.5	.131
Total	133.3	100.0	11.3	.991
Total losses	1179.5		100.0	8.770

Table X-3

Dimensions are for model
(Multiply by 10 for full scale)

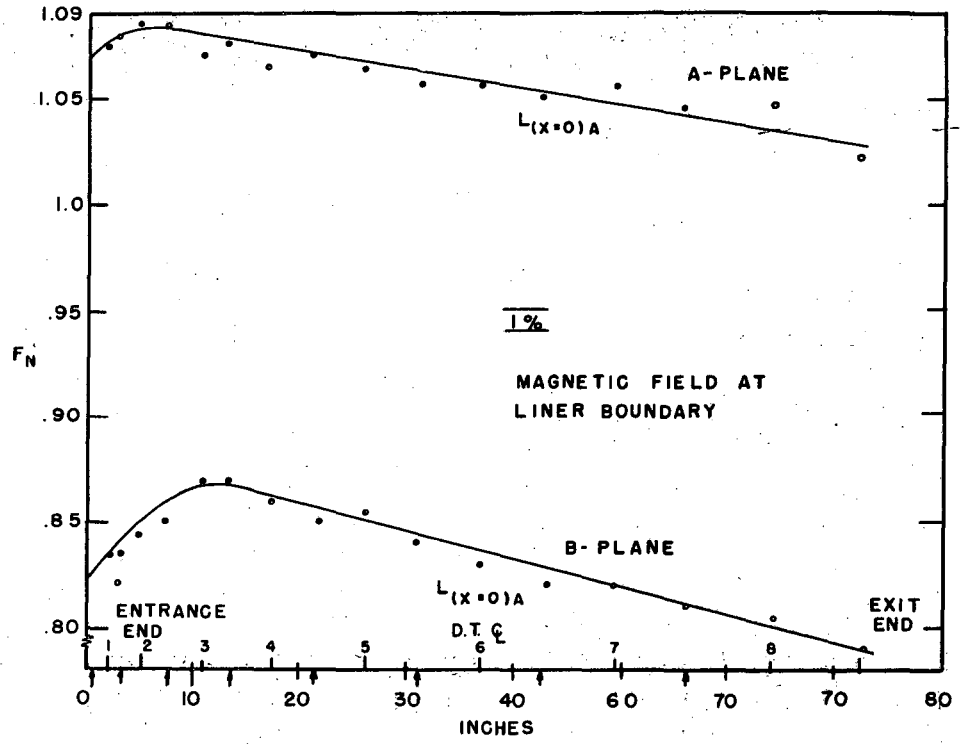

FIG. X - 21

MU 1568

Section IX. It also neglects the end effects due to the finite length of the rod. These are rather complicated in the actual case because of the drift tube on one end and the liner nozzle on the other end but there is no reason to believe that the errors are excessive. A special probe was constructed to work in conjunction with a scaled stem to check the theoretical cosine field distribution. For this test the loop was coplanar with the axis of the stem and approximately 120 inches inside the liner at the number 5 drift tube position. Fig. X-22 shows the loop mounted on the stem and Fig. X-23 shows a rough field plot of the cavity fields with the stem inserted. Measurements were made as a function of stem rotation at several radii and the data reduced to the skin of the stem. The results corroborated the theory well within the estimated experimental error. The loss for each stem was calculated separately using the proper length of stem and radial field distribution with no stem present as given in Figs. X-7 and X-8. For calculation purposes Eq. (II-83) can be rewritten:

$$B_t = 2B \cos \theta$$

Then:

$$\iint |B_t|^2 \, ds = 4 \int_0^{2\pi} \int_{\ell_1}^{\ell_2} \left| B^2 \cos^2 \theta \right| a \, dr \, d\theta$$

$$= 4\pi a \int_{\ell_1}^{\ell_2} \left| B^2 \right| dr$$

Where: B^2 = magnetic field distribution along stem axis with no stem present from Figs. X-7 and X-8.

ℓ_1, ℓ_2 = drift tube radius and liner radius for the particular drift tube being calculated

a = radius of the stem = 0.875 in. (model dim.)

Applying this equation to each stem (in terms of F_N^2 instead of B^2) results in a relative loss for each stem. These are tabulated in Table II-3.

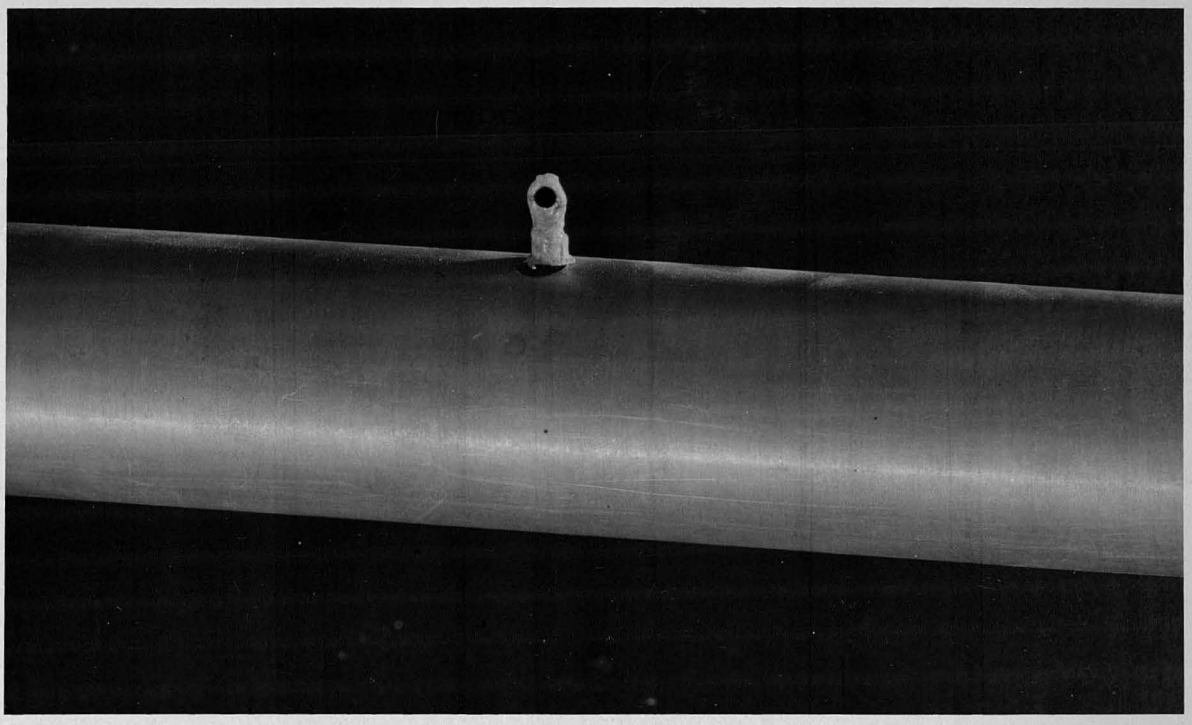

STEM FIELD DISTRIBUTION PROBE

FIG. X-22

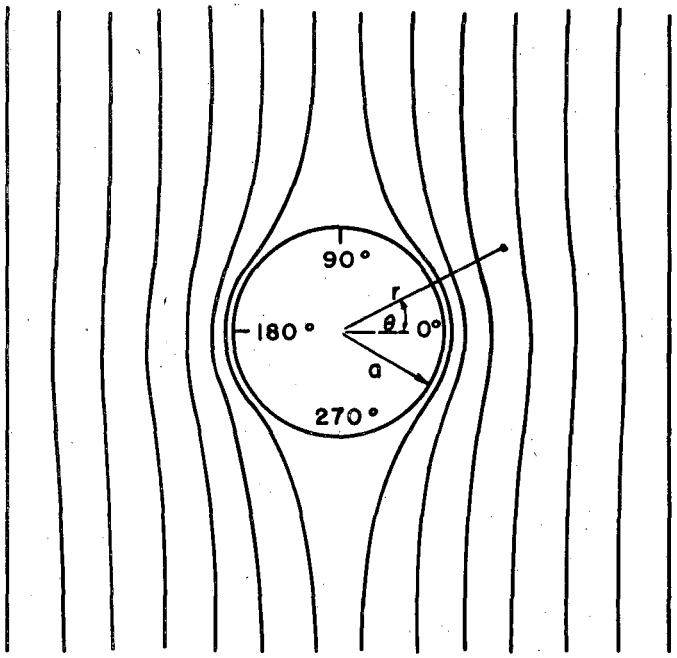

SKETCH OF FIELD PERTURBATIONS NEAR STEM

FIG. X-23

MU 1569

The drift tube losses were measured with special flexible tip probes as shown on Figs. X-24 and X-25. These were designed so that the surface field distributions could be measured without perturbing the fields. This was accomplished by inserting the rigid probe stem into the center of the drift tube where it could be positioned on a frequency constant line. The flexible tip was then adjusted outside the cavity on a drawing of the drift tube section to the desired position and a reading taken. This process was repeated for one-inch intervals around the drift tube and the results plotted. The process was laborious and a number of the points did not fall on a reasonable curve. This became more and more true for the smaller drift tubes. However enough data were taken to show that for all the drift tubes the distribution was sinusoidal. Fig. X-26 shows the theoretical and measured results for drift tube #8. The plot is in terms of the square of the field because this is the quantity measured and also the way it appears in the integral. On this basis the losses for each drift tube were calculated using the $\cos^2 \theta$ distribution and the individual geometries. In order to place the drift tube losses on the same relative scale as other losses the maximum field at the longitudinal center of the drift tube was taken from the curves of Figs. X-5 and X-6. The results of the surface integration for the drift tubes are tabulated in Table X-3.

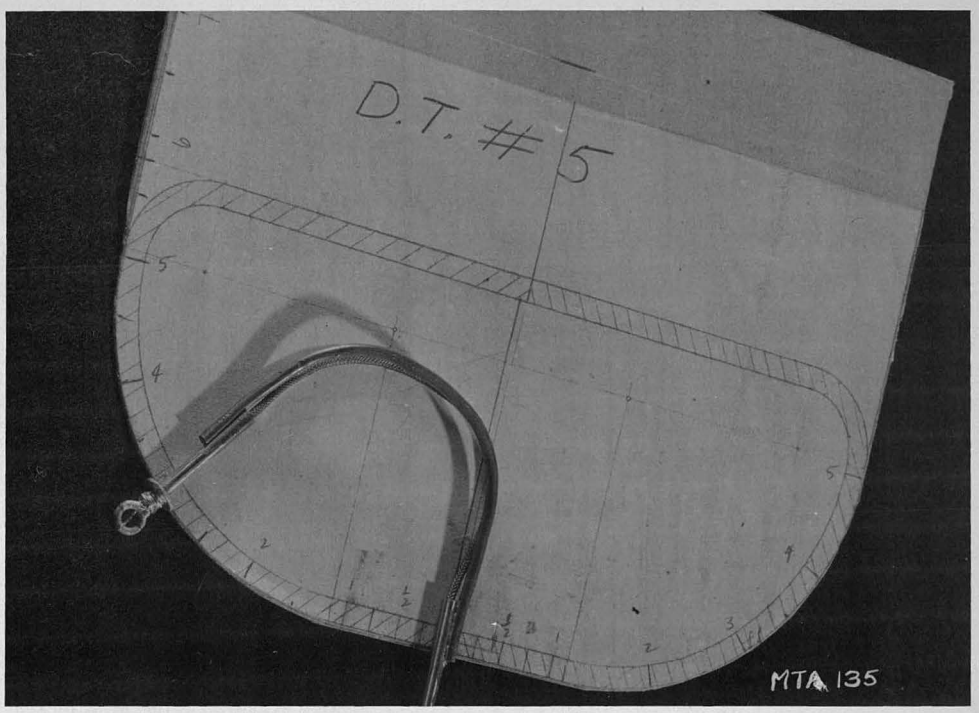

DRIFT TUBE FIELD DISTRIBUTION PROBE SETTING CARD.

FIG. X-24

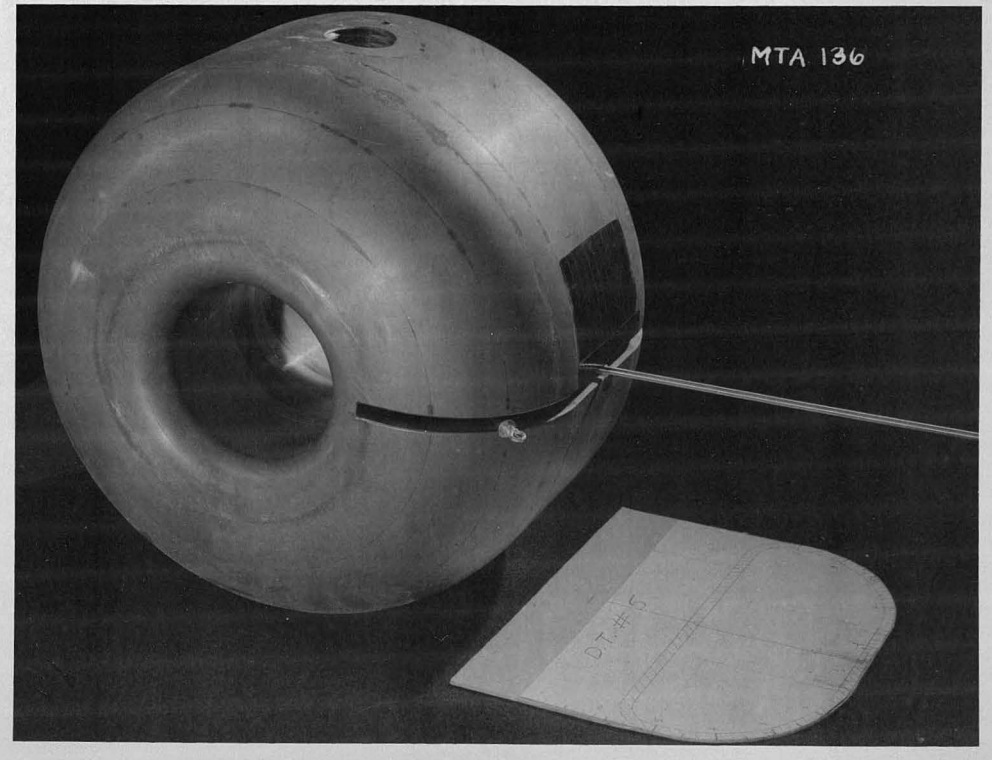

DRIFT TUBE FIELD DISTRIBUTION PROBE IN MEASURING POSITION.

FIG. X-25

NOTE: Ordinates are proportional to H^2. The current distribution would be a cosine curve.

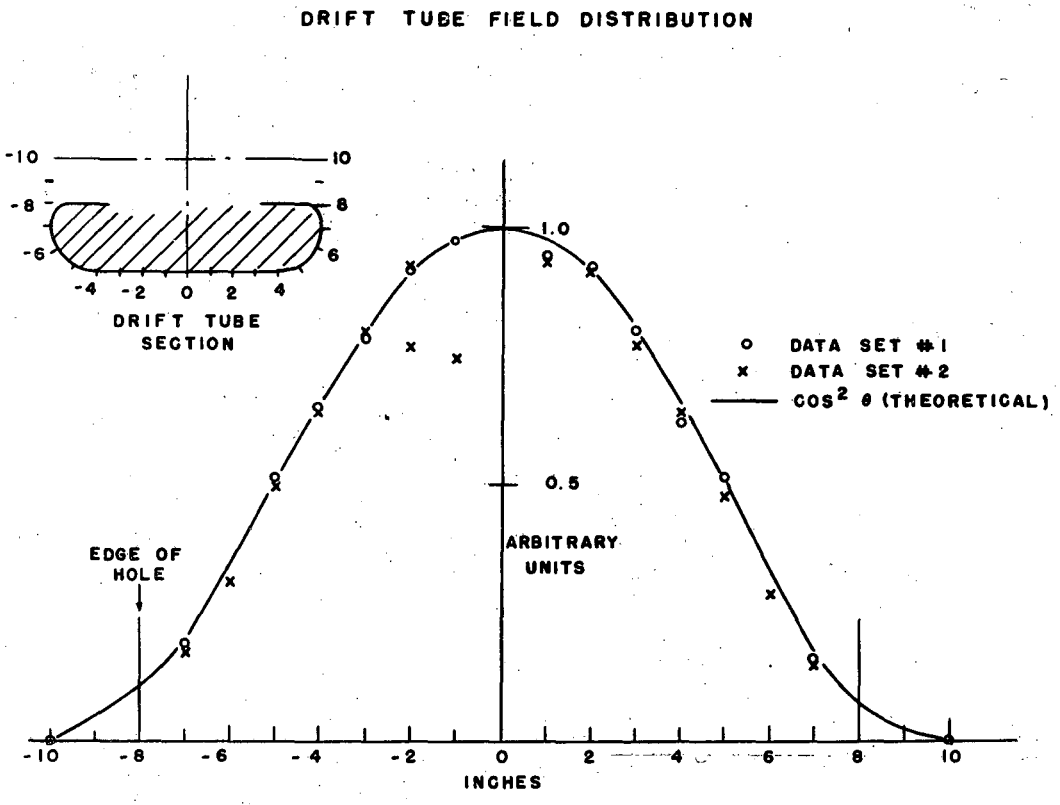

FIG. X-26

XI RESULTS

With the data of the preceding section and the design characteristics it is possible to calculate some of the operating characteristics from the formulae derived in Section II.

A. Shunt impedance, Z_s

Eq. (II-53) can be written

$$Z_s = \frac{1.241 \times 10^9}{\lambda^{3/2}} \left[\frac{\left(\iint_{field} F_N \cdot dA \right)^2}{\iint_{\Sigma s} F_N^2 \cdot ds} \right] \text{ohms}$$

$$\lambda^{3/2} = (24.67)^{3/2} = 122.5 \text{ meters}^{3/2}$$

$$\iint_{field} F_N \cdot dA = 116.3 \text{ meters}^2 \quad \text{(from Table X-1)}$$

$$\iint_{\Sigma s} F_N^2 \cdot ds = 1179.5 \text{ meters}^2 \quad \text{(from Table X-3)}$$

$$Z_s = 116 \times 10^6 \text{ ohms} \pm 3 \text{ percent} \qquad \text{(XI-1)}$$

B. Q

From Eq. (II-60)

$$Q = \frac{5.248 \times 10^5}{\sqrt{\lambda}} = \left[\frac{\iiint_{volume} F_N^2 \, dv}{\iint_{\Sigma s} F_N^2 \, ds} \right]$$

$$\sqrt{\lambda} = \sqrt{24.67} = 4.967$$

$$\iiint_{volume} F_N^2 dv = 3.03 \times 10^3 \text{ meter}^3 \quad \text{(from Eq. (X-1))}$$

$$\iint_{\Sigma s} F_N^2 \, ds = 1179.5 \text{ meters}^2 \text{ (from Table X-3)}$$

$$Q = 2.71 \times 10^5 \pm 3 \text{ percent} \qquad \text{(XI-2)}$$

This value must be compared to that measured directly as described in Section VII. It is

$$Q_M = 2.46 \times 10^5 \pm 2 \text{ percent}$$

The difference between the two values is 9 percent.

It is convenient for the following analysis to work in terms of the results on the model. We will use primes on all model values to differentiate them from full scale values.

$$Q' = 85{,}830 \pm 3 \text{ percent}$$

$$Q_M' = 77{,}800 \pm 2 \text{ percent}$$

$$\text{Difference} = 9 \text{ percent}$$

Originally this difference was 17 percent but by means of the silver plating (discussed is Section III and Appendix A) the improvement was effected. As a check on the location of these losses Q was determined by field plots and measurement for the unloaded cavity (i.e., no drift tubes or stems) as discussed in Appendix C, yielding:

$$Q'_{(\text{unloaded})} = 96{,}100 \pm 3 \text{ percent}$$

$$Q'_{M(\text{unloaded})} = 88{,}000 \pm 3 \text{ percent}$$

$$\text{Difference} = 8 \text{ percent}$$

This indicates that the discrepancy between measured Q and calculated Q is almost entirely in the liner. This is not a serious matter provided the power loss represented by this difference does not occur in a small area. The geometry of the liner is such that a highly concentrated loss is very unlikely. Further, it is conceivable that the construction of the model cavity, although done with great care, differs from the ideal conditions assumed in the calculation by this

amount. Several checks were made of obvious possibilities for differences: (a) The slots were covered with a copper strip to prevent fringing of the fields. (b) The liner nozzles were shorted out by placing a flat copper sheet flush with the liner on the inside making good contact to the stems. (c) The bypass capacitors were shorted with copper straps. It is perhaps worth noting that the two values differ by less than two probable errors and would require some refinement of techniques to detect small improvements. In any case, after due consideration, it was decided not to pursue the investigation further.

C. Absolute fields and currents

In order to convert the field quantities, F_N, to absolute fields it is necessary to calculate the absolute value of the field B' at the position of the calibration point because this was the normalizing point. This can be done using Eq. (II-66)

$$B(r,\theta,z) = F_N(r,\theta,z)\, B'$$

Integrating both sides

$$\iint_{\text{field}} B \cdot dA = B' \iint_{\text{field}} F_N \cdot dA$$

The left hand side can be determined from Eq. (II-21)

$$\iint_{\text{field}} B \cdot dA = \frac{V_c}{\omega} = 0.591$$

Where: $V_c = 45.18 \times 10^6$ volts (a design figure for the end-to-end voltage)

$$\omega = 2\pi f = 2\pi \times 12.16 \times 10^6 = 76.403 \times 10^6$$

$$\iint_{\text{field}} F_N \cdot dA = 116.3 \text{ meter}^2 \text{ (from Table X-1)}$$

$$B' = \frac{0.591}{116.3} = 5.08 \times 10^{-3} \text{ webers/meter}^2 \qquad \text{(XI-3)}$$

As indicated in Section II-H currents will scale in the same manner as fields. If we choose a field value, F_N, from the curves of Section X at a conducting boundary the current is expressed by Eq. (II-67):

$$I_s = \frac{B' F_N}{4\pi} \times 10^7$$

$$B' = 5.08 \times 10^{-3} \text{ webers/meter}^2$$

$$I_s = (4.04 \times 10^3) F_N \text{ peak amperes/meter} \qquad \text{(XI-4)}$$

D. Stored energy

From Eq. (II-23)

$$U_H = \frac{1}{2\mu} (B')^2 \iiint_{\text{volume}} F_N^2 \, dv$$

$$\mu = 4\pi \times 10^{-7}$$

$$B' = 5.08 \times 10^{-3} \text{ webers/meter}^2$$

$$\iiint_{\text{volume}} F_N^2 \, dv = 3.03 \times 10^3 \text{ meters}^3$$

$$U_H = 3.11 \times 10^4 \text{ joules} \pm 3 \text{ percent} \qquad \text{(XI-5)}$$

E. Power loss

From Eq. (II-16)

$$P_L = \frac{1.431 \times 10^9}{\sqrt{\lambda}} (B')^2 \iint_{\Sigma s} F_N^2 \, dv$$

$$\sqrt{\lambda} = 4.967$$

$$\iint_{\Sigma s} F_N^2 \, dv = 1179.5$$

$$(B')^2 = 25.806 \times 10^6$$

$$(P_L)_{\text{total}} = 8.77 \times 10^6 \text{ watts} \pm 3 \text{ percent} \qquad \text{(XI-7)}$$

A further useful relation is the power density at any point on the conducting surfaces. This can be obtained from Eq. (XI-4) and the power density relation.

$$P_D = \frac{I_s^2 R_s}{2} \text{ ohms/meter}^2$$

$$I_s = 4.04 \times 10^3 F_N$$

$$R_s = 9.101 \times 10^{-4} \text{ ohms/square}$$

$$P_D = 7420 F_N^2 \text{ watts/m}^2 \qquad \text{(XI-8)}$$

The values of F_N can be obtained from the curves of Section X.

XII ABSOLUTE FREQUENCY AND PERTURBATIONS

An accurate determination of the frequency of oscillation of the cavity was essential for the optimum design of other components of the mcahine. The following paragraphs summarize the frequency measurements and calculations of the absolute frequency and its variation with physical perturbations of the cavity structure. All of the measurements were made with the cavity initially aligned to the design conditions as set forth in Sections II, III, and IV.

A. Absolute frequency

Measured with Signal Corps Frequency Meter TS-175/U, Serial #833. Drift tubes aligned to ± 0.20 inch, end walls flat to ± 5/8 inch, radius accurate to ± 5/8 inch.

The following limits of error have been estimated for the actual manufacture tolerances of the 1/10 scale model. These have been translated into frequency shifts of the full scale machine using the perturbation coefficients set forth in the succeeding sections of this report:

Component	Mechanical Accuracy	Frequency Variation Limits
Frequency meter accuracy	----	± 0.01 Mc/sec.
Entrance end flatness	5/8 inch	± 0.006 "
Exit end flatness	5/8 inch	± 0.005 "
Cavity length	5/8 inch	± 0.001 "
Cavity radius	5/8 inch	± 0.020 "
Drift tube position (8 tubes): axially	0.2 inch/DT	± 0.002 "
tranversely	1.25 inches/DT	± 0.001 "
Drift tube length (8 tubes)	0.05 inch/DT	± 0.004 "

Component	Mechanical Accuracy	Frequency Variation Limits	
Drift tube diameter (8 tubes)	Different for each DT	± 0.002	Mc/sec.
Temperature effect for 10° C variation	----	± 0.002	"
	Total spread	± 0.053	"
	R.M.S. of error	± 0.023	"
The experimentally determined frequency is 12.26 ± 0.023			"

Note: The 1/10 scale cavity is 0.25 inch longer than design figures. Full scale this is 2.5 inches and this raises the measured frequency 0.002 Mc/sec. which is outside the accuracy of measurement.

B. Frequency perturbation coefficients

This table is a summary of frequency changes to be expected with various perturbations of the full scale cavity. The following sections indicate how the figures below were determined.

Item	Coefficient	Direction to Decrease Resonant Frequency
DT #1 moved along axis	1.7 ± 0.1 Kc/inch	Move towards exit end
DT #8 moved along axis	0.7 ± 0.05 Kc/inch	Move towards exit end
Move drift tube off axis	less than 0.15 Kc/inch	Move towards axis
Change length of drift tube	10 ± 2 Kc/inch	Increase length of drift tube
Change diameter of drift tube:		
DT #0	1.5 ± 0.3 Kc/inch	Increase diameter of drift tube
DT #1	1.7 ± 0.03 "	
DT #2	2.27 ± 0.5 "	
DT #3	3.08 ± 0.6 "	
DT #4	4.20 ± 0.8 "	
DT #5	5.4 ± 1.1 "	

Item	Coefficient	Direction to Decrease Resonant Frequency
Change diameter of drift tube:		
DT #6	6.6 ± 1.3 Kc/inch	
DT #7	7.7 ± 1.5 "	
DT #8	9.2 ± 1.8 "	
Entrance End Wall Oil Can Tuning	9.3 ± 0.5 Kc/inch	Push in entrance end wall
Exit End Wall Oil Can Tuning	8.0 ± 0.5 Kc/inch	Push in exit end wall
Entrance End Wall Parallel Displacement Along Axis	1.0 ± 1.0 Kc/inch	Decrease length of cavity
Exit End Wall Parallel Displacement Along Axis	1.3 ± 1.0 Kc/inch	Decrease length of cavity
Wide Panel	3.8 ± 0.4 Kc/inch	Move away from axis of cavity
Narrow Panel	1.7 ± 0.2 Kc/inch	Move away from axis of cavity
Change Radius of Cavity	32 ± 4 Kc/inch	Increase radius
Change Cavity Temperature	0.2 ± 0.01 Kc/°C	Increase temperature

C. Drift tube perturbations

1. Drift tube displacement

Frequency perturbations measurements were made by measuring the change in modulation frequency necessary to restore resonance when the cavity is excited with a sideband from a high frequency oscillator using the equipment set up for Q measurement (Section VII).

(a) Axial displacement

The drift tubes were displaced axially along the cavity with the stems restrained at their outer extremities. It was convenient to measure only drift tube #1 and #8 but these represent the limiting cases for size of tube and length of gap.

(1) Drift tube #1

$$\frac{\Delta f}{\Delta l} = 1.7 \pm 0.1 \text{ Kc/inch}$$

(2) Drift tube #8

$$\frac{\Delta f}{\Delta l} = 0.7 \pm 0.05 \text{ Kc/inch}$$

Displacing the drift tubes towards the exit end decreases the resonant frequency of the cavity.

The above variations are small, as expected, because there is very little net change in total loading capacity due to a tube moved in such a manner. The capacity is decreased in one gap but there is a nearly compensating increase in the second gap affected. It is expected that approximately the same frequency shift would occur if the drift tubes were displaced by translating axially the entire drift tube and stem support.

(b) Transverse displacement

Displacing the drift tube off the axis shifts the resonant frequency of the cavity less than one-fifth the amount that the frequency is shifted when the drift tube is displaced the same distance along the axis.

2. Change in drift tube dimensions

(a) Change in length

A rough estimate of the perturbation due to a change in length of the drift tubes was taken from some measurements on the high-β cells relating a variable g/l with frequency, for constant d/D and β . This could be obtained for only one drift tube (#6) and only approximately.

(b) Change in diameter

The frequency change as function of drift tube diameter was calculated approximately from the change in volume effected by a given change:

$$\frac{\Delta f}{\Delta v} = \frac{f_{unloaded} - f_{loaded}}{\sum_{o}^{8} \text{volume of drift tubes}}$$

$$f_{unloaded} = 13.82 \text{ mc/sec.}$$

$$f_{loaded} = 12.26 \text{ mc/sec.}$$

$$\sum_{o}^{8} \text{volume} = 3.5 \times 10^{6} \text{ cu. in.}$$

With this equation and the Δv calculated for each drift tube for a change of diameter of 1 inch, the table of part B was calculated.

D. End wall perturbations

1. End wall diaphragm movement

Provision was made to vary the resonant frequency of the cavity by applying forces at the center of both the entrance and exit end walls, sometimes called oil-can-tuning. Frequency changes effected by such tuning are as follows:

(a) Entrance end wall

$$\frac{\Delta f}{\Delta l} = 9.3 \pm 0.5 \text{ Kc/inch}$$

(b) Exit end wall

$$\frac{\Delta f}{\Delta l} = 8.0 \pm 0.5 \text{ Kc/inch}$$

Pushing in either end wall decreases the resonant frequency.

2. End wall motion

No provision was made for moving the complete end wall along the axis in the manner of a plunger; however, consideration is given to the frequency shift that would occur in such a case because manufacturing tolerance will allow the complete cavity to deviate slightly from the exact design length.

The basic equations for the calculation of this perturbation are found in

Section II-I, Eqs. (II-63) and (II-64). This condition falls under Case 2 of that section. The magnetic effect, Δf_H, can be calculated from the field distribution curves for either end and the electric effect can be determined approximately from the measured diaphragm movement. Examination of the field distributions indicates that the electric field is concentrated at the center of the cavity and the magnetic field is small at the center of the cavity. This being the case the diaphragm movement perturbation is essentially one involving the electric field only (within the accuracy required, at least). Then the perturbation, Δf, is the difference between the calculated Δf_H, and the measured Δf_E for the same physical perturbation. The results for the entrance and exit end walls are:

(a) Entrance end wall

$$\frac{\Delta f}{\Delta l} = 1.0 \pm 1.0 \text{ Kc/inch}$$

(b) Exit end wall

$$\frac{\Delta f}{\Delta l} = 1.3 \pm 1.0 \text{ Kc/inch}$$

Again, pushing in either end wall decreases the resonant frequency.

E. Outer cylinder perturbations

These were calculated as indicated in Section II-I (Case 1). In this case the result is simplified because the $\int_{\Delta V} E_a^2 \, dV \ll \int_{\Delta V} H_a^2 \, dV$ and $\int_{\Delta V} H_a^2 \, dV$ can be evaluated from the field plots.

1. Wide flat panels

If just one of the wide side panels were displaced normal to the cavity axis:

$$\frac{\Delta f}{\Delta l} = 3.8 \pm 0.4 \text{ Kc/inch}$$

2. Narrow flat panels

For a single narrow side panel displaced normal to the cavity axis:

$$\frac{\Delta f}{\Delta l} = 1.7 \pm 0.2 \text{ Kc/inch}$$

Reducing distance from panel to axis increases frequency.

If the results of "1" and "2" are summed around the cavity for the 14 small panels and the 2 large panels the perturbation for a change of the entire cavity radius is obtained.

$$\frac{\Delta f}{\Delta l} = 32 \text{ Kc/inch}$$

Reducing the radius increases frequency.

(This can be roughly compared to a right circular cylinder without drift tubes of the same frequency. Its radius will be 940 cm.

$$\frac{\Delta f}{\Delta l} = 34 \text{ Kc/inch} \quad)$$

F. Temperature coefficient of frequency

It is assumed that the frequency effect is due primarily to the change in dimensions of the cavity due to expansion of the copper. From Part B it is noted that the frequency perturbation due to a change in length is very much less than that due to a change in radius. Neglecting the former:

$$\frac{\Delta f}{\Delta^{\circ}C} = 0.2 \pm 0.02 \text{ Kc/}^{\circ}C$$

Increase in temperature will decrease frequency.

APPENDIX A

SILVER PLATING

A silver plating program was conducted by this group during the measurements on the 8 ½ M for the reasons given in Section III. The procedures used were patterned after those used by Cook in obtaining high conductivity silver (UCRL-1068).

The surfaces of the DT's and stems were carefully prepared to give a smooth base upon which to plate. All scratches and pits were filled with 70-30 soft solder. Also a small filet (about 1/8 in. radius) was built up around the base of the stems to form a transition from the DT to the stem. The drift tubes and stems were then sanded smooth with a Speedmatic Sander model 1000 work to #600 paper.

The drift tubes and stems were cleaned with a detergent and C.P. alcohol. The commercial degreasing bath available could not be used because the heat caused the soft solder joints in the DT's to break due to differential expansion.

The drift tubes and stems were plated with approximately 2 mils of copper. This was done to give a uniform surface over the entire drift tube and stem which could be easily silver plated. Although a cold copper sulphate bath was used, no difficulty was experienced in striking the copper over the soft solder joints. Both the copper strike and the copper plating were done in the same bath, which consisted of 33 oz/gal. copper sulphate and 10 oz/gal. sulfuric acid.

The copper plated DT's were sanded with #600 paper and buffed to a high polish. All surfaces were examined carefully for defects which would affect the silver plate. If any doubt existed about the surface of any drift tube, it was replated. Those drift tubes which were considered satisfactory were again cleaned with a detergent and C.P. grade alcohol in preparation for silver

plating.

Unlike the copper plating, the silver strike and silver plating were done in separate baths. These baths were composed of:

Strike bath

Silver cyanide	.9 oz/gal.
Potassium carbonate	2 oz/gal.
Potassium cyanide	10 oz/gal.

Plating bath

Silver cyanide	4.8 oz/gal.
Potassium carbonate	6 oz/gal.
Potassium cyanide	8 oz/gal.

Distilled water and C.P. grade chemicals were used for both baths.

Because of the geometry of the drift tubes with stems attached, plating currents in terms of amperes per square foot of surface to be plated have little meaning. Therefore, the currents used were determined empirically. No doubt there was some variation in the thickness of the plating. However, by plating 1-$\frac{1}{2}$ mils at the base of the stem where the current density was as low as at any point on the tube or stem, the minimum silver thickness was of the order of 6 skin depth at 120 megacycles/sec.

APPENDIX B

HALF-WAVE RESONATOR

In order to measure the conductivity resulting from several silver plating processes, a half-wave coaxial transmission line resonator was constructed.

The outer conductor was a copper tube six feet long with an inside diameter of six inches. Metal rods one inch in diameter and four feet long could be inserted to act as the center conductor. The extra foot in length of the outer conductor prevented radiation from the two open circuit ends of the transmission line.

For equal conductivity, the ratio of losses in the inner and outer conductor are inversely proportional to their radii. Thus when the transmission line is resonated, about six times as much power is dissipated in the inner conductor as in the outer conductor. By measuring Q when various rods are used as the inner conductor it is possible to determine relative conductivity of different rods and to calculate the actual conductivity of the various conductors that are inserted.

Relative d.c. conductivities can be determined to an accuracy of about 2 percent by means of the Q-measuring equipment mentioned in Section VII, and absolute conductivity can be calculated with an accuracy of about 6 percent.

APPENDIX C

Q OF THE UNLOADED CAVITY

The first experimental measurements of the Q of the model cavity gave a result which was approximately 15 percent lower than the value calculated from the magnetic field distributions. In order to separate the liner and drift tube effects a set of measurements was made on the unloaded cavity, i.e., with the stems and drift tubes removed. The measured Q was determined by the bandwidth method exactly as for the loaded cavity. The frequency was 138.2 megacycles/sec. It was not possible to make a complete field plot of the cavity because the taper of cavity with no drift tubes present causes the field lines to curve near the liner in order to satisfy the boundary conditions. This makes it impossible to insert probes along frequency constant lines as was done in the loaded cavity. It was believed that the radial field distributions were independent of z which would allow the use of the radial field distributions at the ends by normalizing to the fields as measured along the side for planes in between. This was checked by making several radial B-B runs at different values of z. Our belief was corroborated as all the distributions taken had the same shape. Figs. C-1 and C-2 show the field distributions at the liner walls. Fig. C-3 shows a comparison of the radial distributions on the A- and B-planes with $J_1(2.405x)$, which is the theoretical radial distribution for a right circular cylinder. The integration was carried out in the same manner as for the loaded cavity. The results obtained were:

$Q_{measured}$	88,000 ± 3 percent
$Q_{integration\ of\ fields}$	96,000 ± 3 percent

These results indicate that about 8 percent of the discrepancy in the Q of the loaded cavity as obtained by the two methods was due to the liner and the

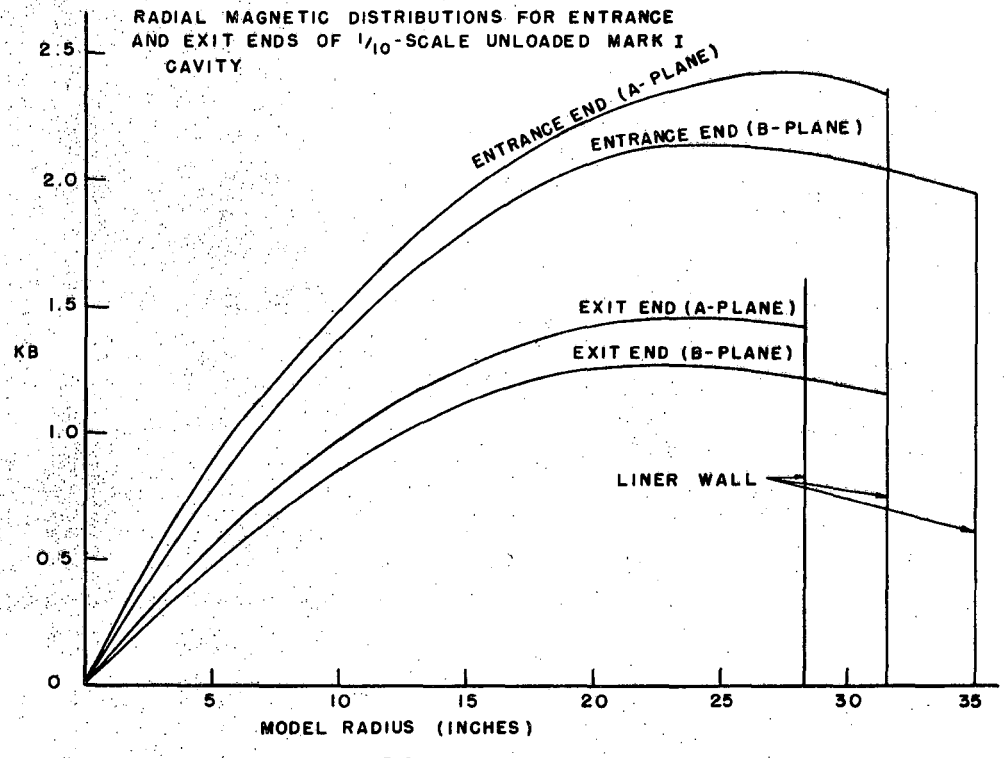

FIG. C-1

MU 1571

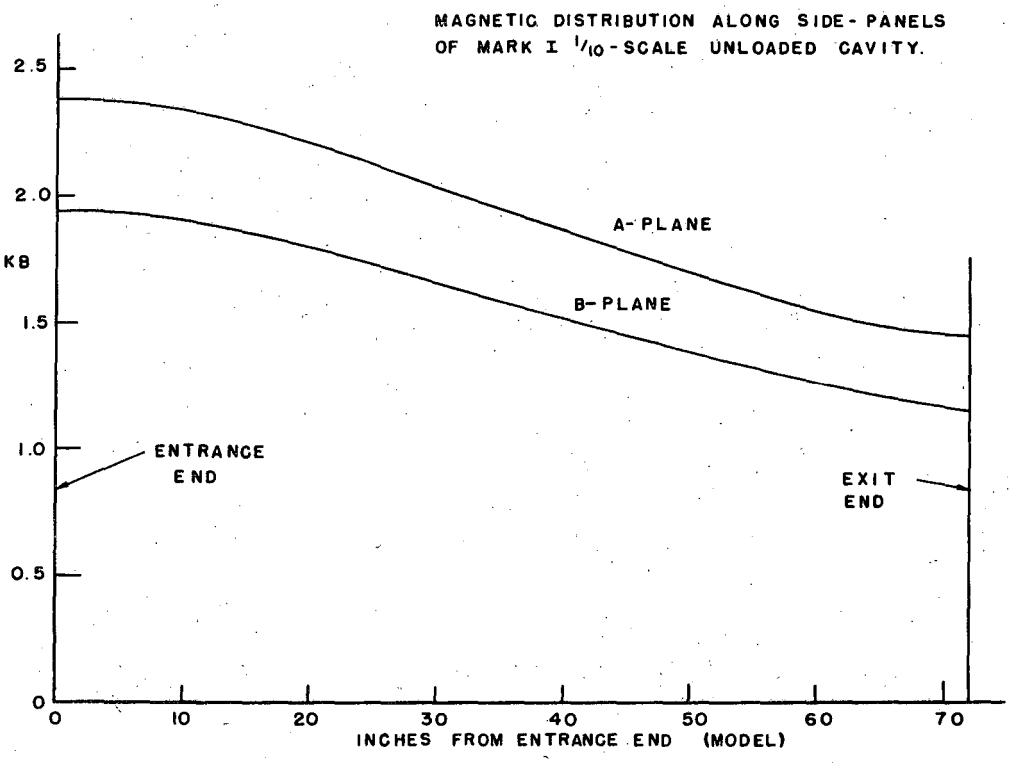
MAGNETIC DISTRIBUTION ALONG SIDE-PANELS
OF MARK I 1/10-SCALE UNLOADED CAVITY.
2.5
2.0
KB
1.5
1.0
0.5
0
A-PLANE
B-PLANE
ENTRANCE
END
EXIT
END
0
10
20
30
40
50
60
70
INCHES FROM ENTRANCE END (MODEL)
MU 1572

FIG. C-2

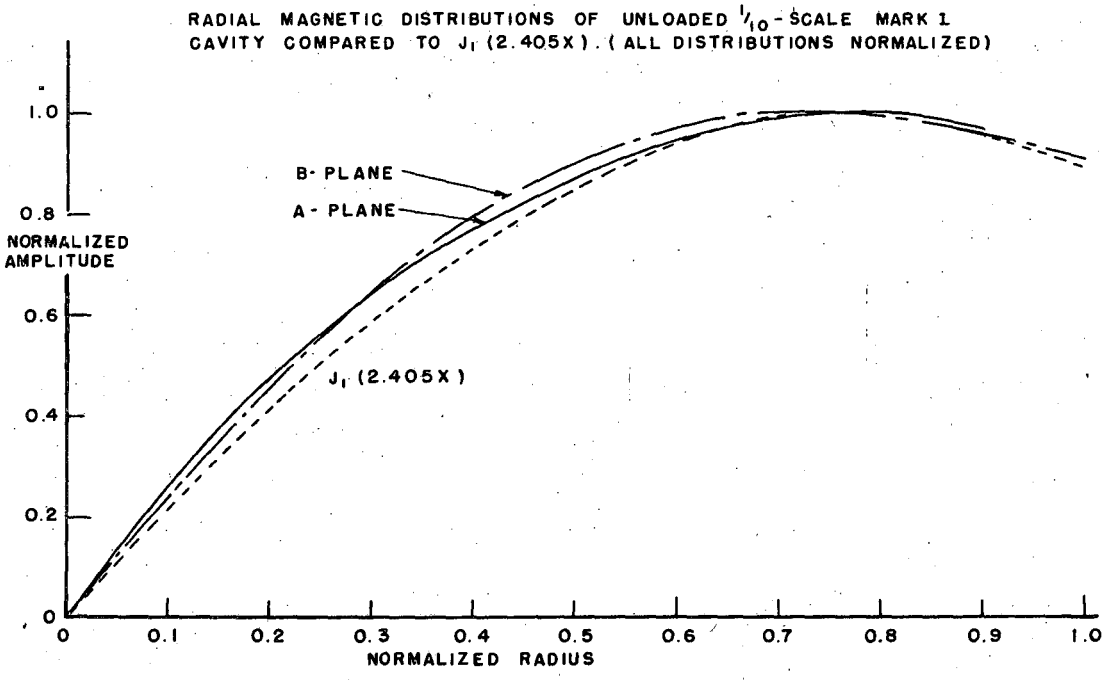

FIG. C- 3

MU 1573

remainder was due to the drift tubes and stems. These differences are probably due to losses in poor solder joints or other imperfections in the manufacture of the liner. It should be noted that the two values listed above are less than one probable error apart.

APPENDIX D

CYLINDRICAL CAVITY

The first electric and magnetic field measurements were made on a cylindrical cavity in order that the measuring equipment and techniques could be tested. When a cylindrical cavity is excited in the TM_{010} mode, the electric and magnetic field distributions are bessel curves of the form $J_o(K_c r)$ and $J_1(K_c r)$ respectively. This not only gives an excellent overall check of the measurement, but enables one to learn the effect that slots and holes in the cavity wall have on the measurements taken in the proximity of these slots and holes. This is important in determining the skin losses in the cavity walls inasmuch as these measurements should be taken as close to the wall as is practical.

One must be careful to differentiate between incorrect readings caused by faulty measuring equipment and those resulting from incorrect insertion of the probe. The frequency and level of the cavity should be monitored at all times to aid in locating equipotential lines. One of the advantages of the cylindrical cavity is that the equipotential lines are radial.

The cavity used was constructed as shown in Fig. D-1. The two halves of the cylinder were spaced $\frac{1}{2}$ inch apart, giving a slot completely around the cavity. Thus the cavity was not a perfect cylinder. Also the two halves did not match by 1/8 inch. Neither of these facts affected the resonance of the cavity as long as shorting strips were placed less than 1/8 wave-length apart around the slot.

Fig. D-2 shows the effect of measuring near an open slot, a "filled " slot, and a wall without slots. The measurements were taken at a constant radius which for the TM_{010} mode means at constant field. The probe was inserted into the cavity far enough not to feel the effect of the slot through which it entered.

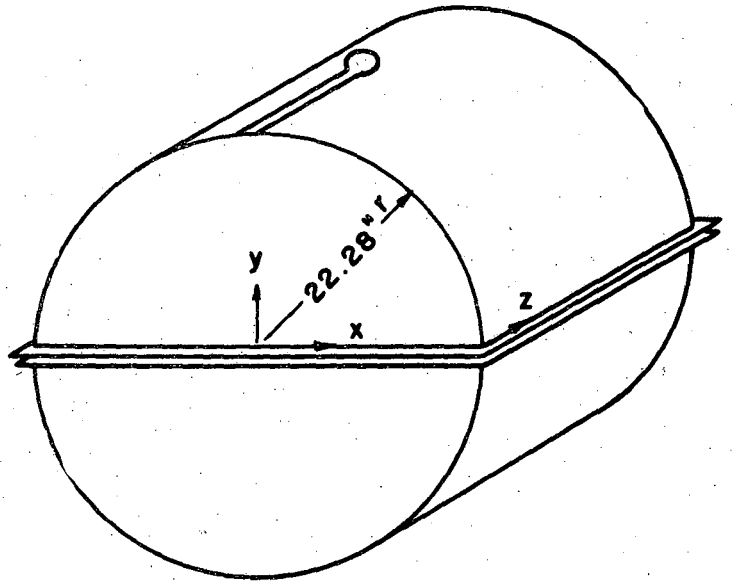

CYLINDRICAL CAVITY

FIG. D-1

MU 1574

CYLINDRICAL CAVITY
MAGNETIC FIELD - SLOT EFFECT
f = 204.3 MEGACYCLES / SEC

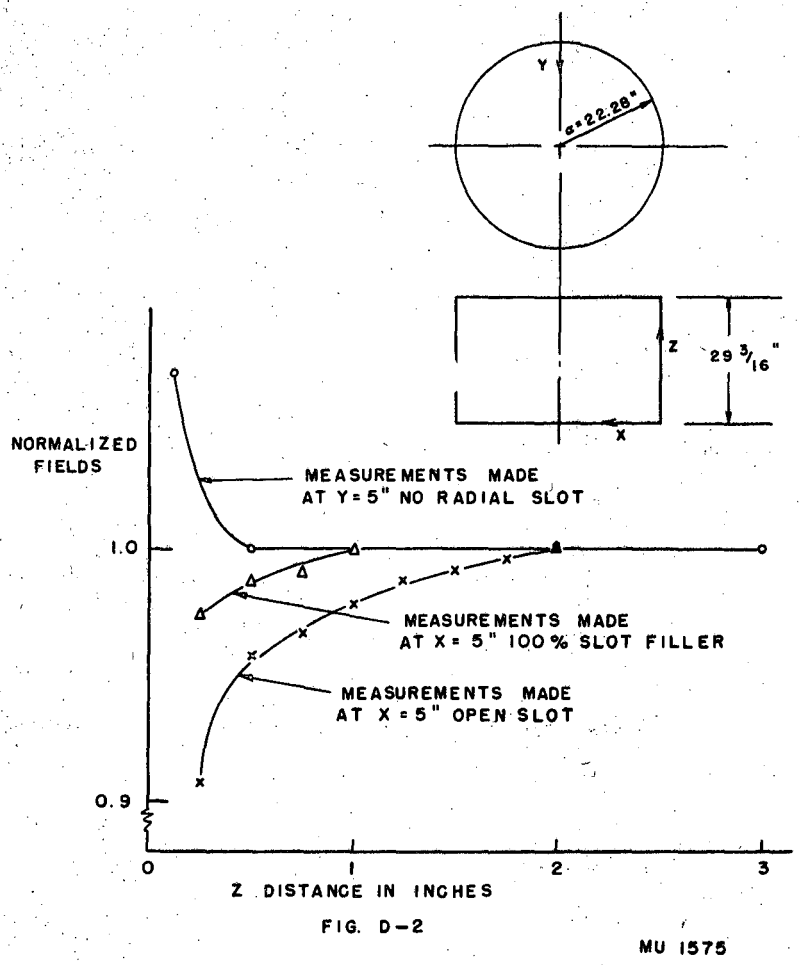

FIG. D-2

MU 1575

As the probe approached the 1/2 in. slot, the field fell from 100 percent at a point 2 in. from the slot to 95.8 percent at a point 1/2 in. from the slot. The slot was then "filled" by placing a piece of 1/2 in. bar stock between the flanges and flush with the inside wall. It was found that the field dropped from 100 percent 1 in. away from the bar to 98.6 percent 1/2 in. away. This was probably caused by the fact that the slot "filler" was not perfect. A measurement was then taken from a longitudinal slot in the top of the cavity so that the probe could approach the end wall at a place where there was no slot. In this case, the field remained constant until the probe came within about 1/8 in. from the wall where the signal rose to about 107 percent, due to image effect.

Fig. D-3 shows the agreement obtained between the theoretical and measured E and H fields distributions taking into account the slot effect.

CYLINDRICAL CAVITY
MAGNETIC FIELD - SLOT EFFECT
f = 204.3 MEGACYCLES / SEC

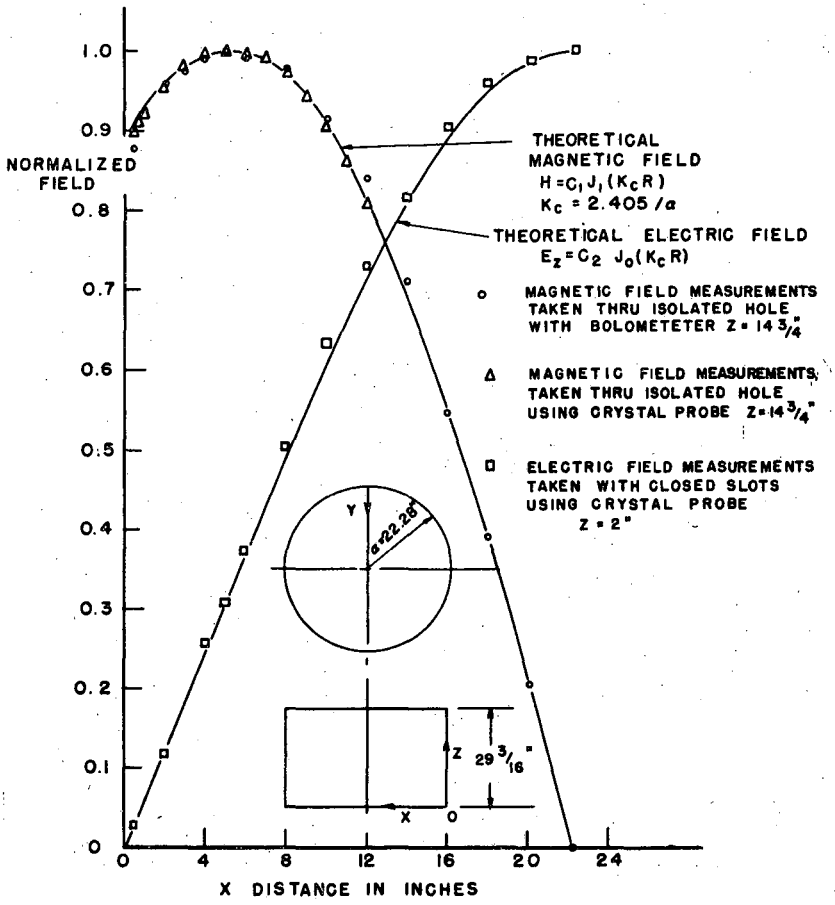

FIG. D-3

MU 1576

APPENDIX E

PUMP-OUT SLOTS IN THE MODEL CAVITY

Toward the end of the measurement program on the 1/10 scale model, a second 234° section of the liner was built to include pump-out slots in the bottom and exit end (Figs. E-1 and E-2). The purpose was to find out if any large power loss would occur as a result of energy from the rf fields radiating through the slots. To reduce the radiation, copper skirts were soldered around the slots.

The measured Q of the cavity with the slotted liner was about 7 percent less than that measured for the cavity with the solid liner. However, when all of the slots were covered with copper sheet no change in Q was observed, indicating that the loss was not due to radiation through the slots.

The 7 percent difference in Q was greater than would be expected from losses resulting from current bunching around the slots alone. Part of the loss may have been due to poor rf joints at the skirts or elsewhere in the slotted section. However, since the effect of bunching at the slots can be calculated with reasonable accuracy, no effort was made to investigate further the losses in the liner.

Information Division
scb/3-20-51

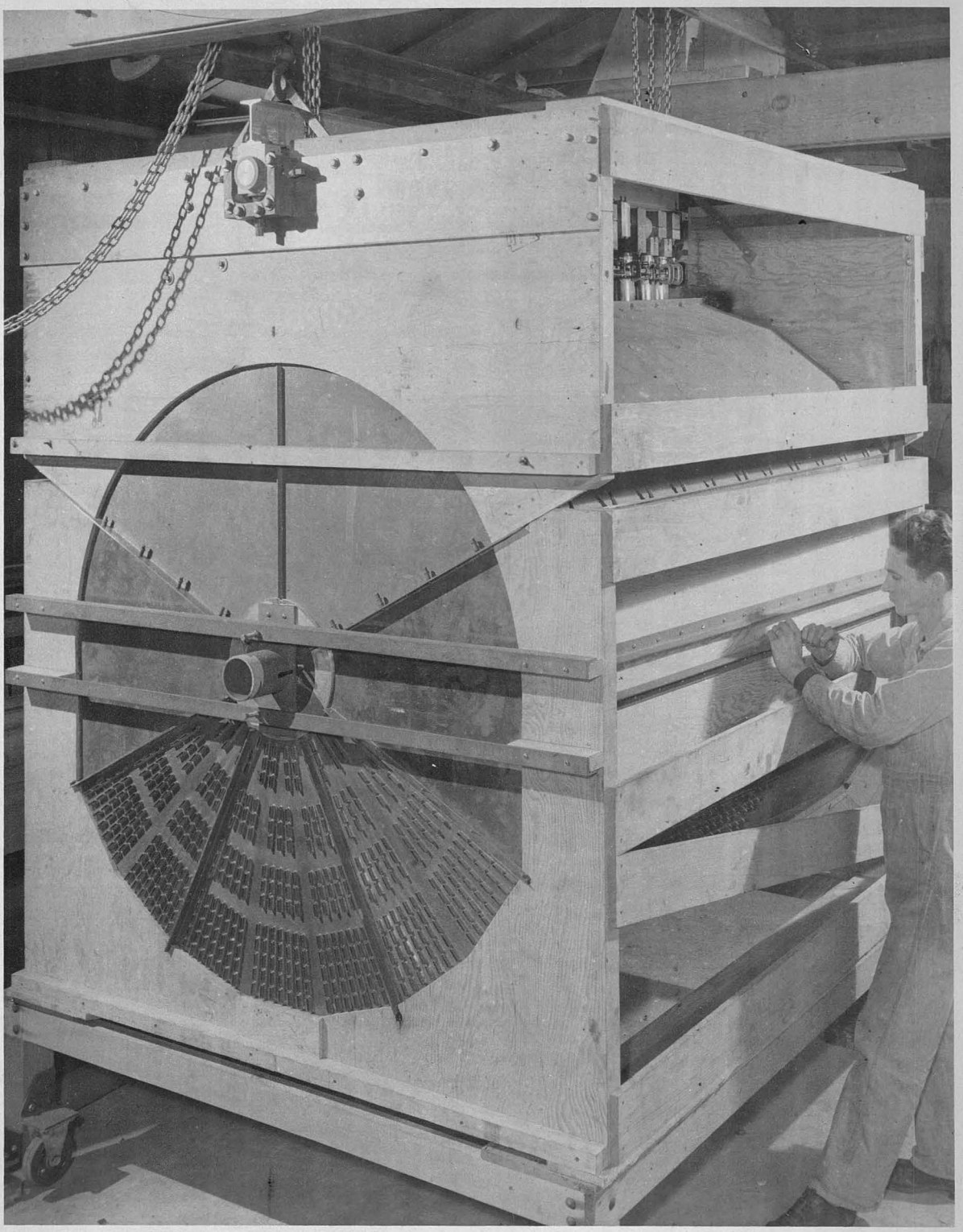

1/10 SCALE MODEL CAVITY SHOWING PUMP-OUT SLOTS

FIG. E-1

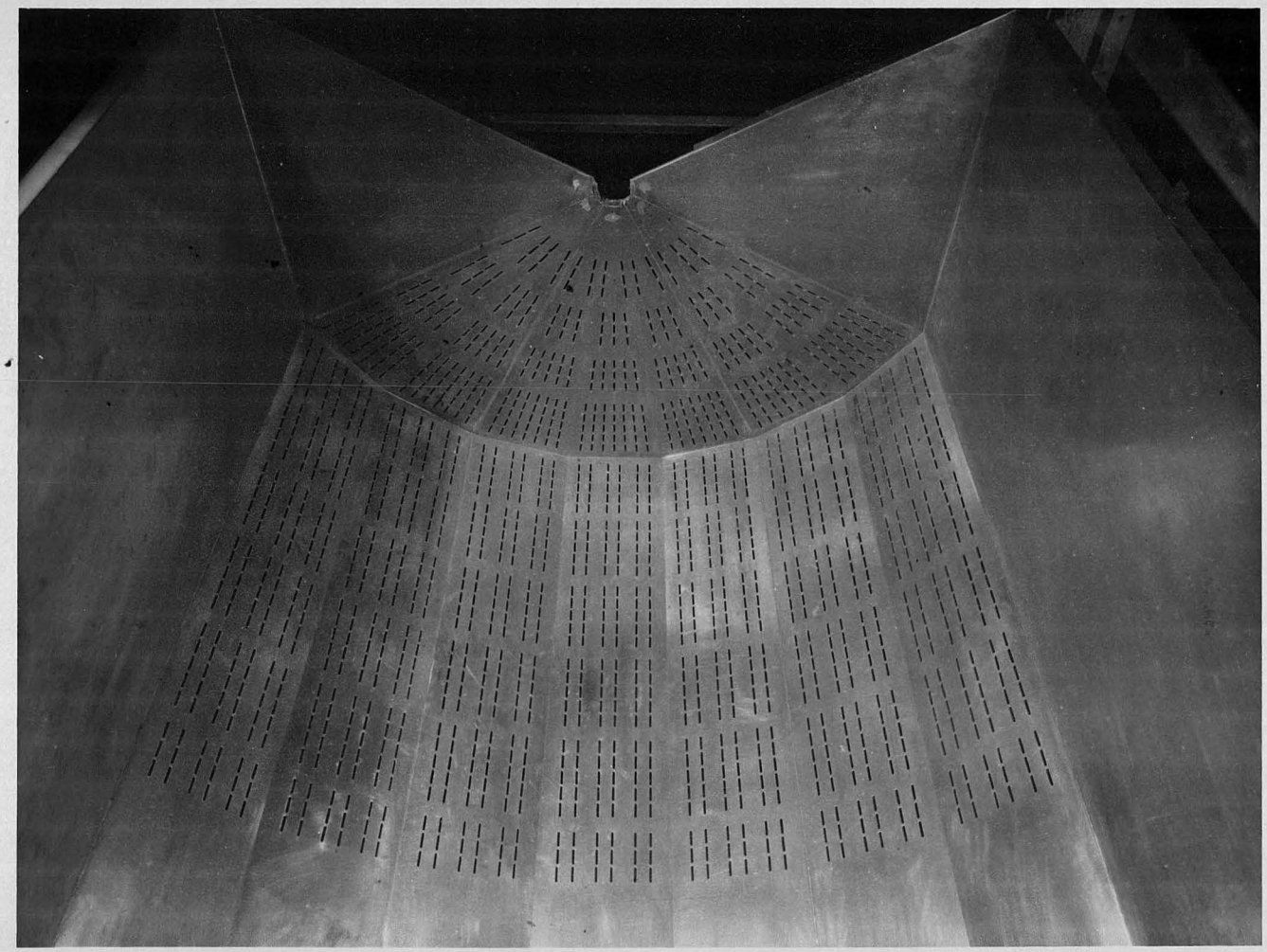

BOTTOM SECTION OF $\frac{1}{10}$ SCALE LINER SHOWING PUMP-OUT SLOTS IN BOTTOM AND EXIT END

FIG. E-2

LIST OF FIGURES

LIST OF TABLES